KYUSHU INSTITUTE OF TECHNOLOGY

Doctoral Thesis

Visual-Inertial Attitude Determination for Small Satellites

A dissertation submitted in partial fulfillment of the requirements
for the degree of Doctor of Philosophy in Engineering

by

Amartuvshin Dagvasumberel

Supervisor: Professor Kenichi Asami

in the
Department of Engineering
Graduate School of Engineering
Kyushu Institute of Technology

September 2019

Abstract

Attitude determination, along with attitude control, is a critical component for many Earth-observation small satellites. However, most of the small satellites operate without redundant attitude sensors due to the satellite's small form factor, so that there is a significant risk of mission failure. Moreover, the range of possible applications for small satellites is limited due to their low available volume, weight, power, and other constraints. The majority of these limitations affect Earth-observation CubeSat-class spacecraft due to the lack of high-performing attitude determination and control systems. Achieving accurate and robust attitude determination and control system in small form factor is challenging and complete attitude knowledge in inertial space requires a combination of multisensors in order to maintain robust attitude estimation in different cases.

Our objective in this dissertation is to improve attitude estimation of Earth-observation satellites using visual and inertial sensors with Unscented Kalman filter. CMOS (Complementary Metal-Oxide Semiconductor) camera is common sensor for CubeSats to carry as its primary payload. Besides, Earth's surface features in an imager's field of view provides an important prior feature for attitude estimation. These observations motivate us to use a CMOS camera as sensor for small satellite's attitude determination system. Our goal is to improve the accuracy of attitude estimation capabilities of the resource-constrained small satellite by using a sensor fusion approach with vision-based and inertial sensors. This improvement increases the possibility of applications that require accurate attitude determination and control system such as laser communications, target tracking and Earth imaging missions for CubeSats.

In this dissertation, we study the issues of vision-based and inertial-aided attitude determination approaches and sensor fusion techniques. The vision-based attitude estimation method is usually achieved by Earth's surface features tracking and feature-correspondences matching techniques with different outlier rejection methods and then provides absolute attitude information in 3 degrees of freedom. Experimental and simulation tests were carried out to qualify the proposed approach's performance. For the validation of the vision-based method's performance, we used raw imagery data of High Definition Earth Viewing (HDEV) payload of the International Space Station (ISS). The performance of the visual-inertial approach is assessed through the realistic Earth-surface scene simulations and results are compared with ground truth data. All the methodology details of the proposed approach have been explained and the test results have been analyzed.

Acknowledgements

It has been an honor and a great privilege to be a doctoral student at Kyushu Institute of Technology (KIT), in the SEIC community, for the last four years. There are many people I would like to acknowledge for making my graduate student life such a great experience.

First of all, I would like to thank my supervisor Professor Kenichi Asami for having offered me the possibility of doing a PhD study under his supervision. He provided me a highly inspiring environment and all the necessary resources to achieve the present work. I thank him for encouraging my research and for allowing me to grow as a research scientist. Without his guidance and constant feedback to reach this point would not have been achievable.

Also, I would like to thank Professor Mengu Cho for his great guidance and helpful advice. I had participated in the BIRDS-1 project, as a member of Camera Subsystem team under his leading. I got a great experience and I have learned a lot from him.

I thanks for Assistant Professor Masui Hirokazu and BIRDS-1 team members for the helping and encouraging me when things not work. Also, thanks to their friendly and fun atmosphere in the laboratory and during conferences abroad.

I thank to all my colleagues; Rafael Rodriguez Leon, Mohamed Elhady Keshk, U.Tuguldur, Shota Ogawa, R.Uezu and all other members with whom I have shared the same laboratory in KIT for three years.

Also I would like to acknowledge the Japanese Government (MEXT) and The United Nations Office for Outer Space Affairs' PNST fellowship program for the financial support throughout my researches in Japan.

I thank to my closest friends; Dr D.Erdenebaatar (teacher), T.Turtogtokh, B.Battuvshin, U.Tuguldur, B.Bolortuya, S.Purevdorj who supported me in every difficult and fun situations.

Also, I would like to thank Professor Tsolmon Renchin for her guidance and helpful advice during my master degree study at National University of Mongolia.

Lastly, I am deeply grateful to my parents, younger brother and sister, who have been always with me despite the long distance between us and all the support they gave me to reach this point.

Contents

List of Figures

List of Tables

Chapter 1

Introduction

This chapter provides background and related concepts to motivate the research work about Visual-Inertial attitude determination. Regarding the satellite miniaturization and the challenges related to attitude determination and control system arises the motivation of this research at the time of the writing the dissertation.

Research Vision is to contribute for demanding of increase of nanosatellite's attitude determination and control system's accuracy and reliability in the future small satellites.

Purpose of research is to develop an vision-based and inertial-aided attitude determination approach for small satellites.

Goal of thesis research is to demonstrate that proposed approach can give reliable and accurate measurements of satellite attitude changes.

1.1 Research motivation

Over the last two decades, the CubeSat category of spacecrafts have become increasingly popular in small satellite industry [1]. This miniature-sized spacecraft technology has enabled institutions to send these small satellites into space and demonstrate sophisticated missions and scientific experiments [2][3]. The CubeSats are a subclass of nanosatellites (less than 10 kg) having a mass of 1.33 kg per unit (U) and a volume of a cube with 10 cm on a side. The first conceptual proposal of CubeSat and new launch standard developed by California Polytechnic State University (CalPoly) and Stanford University. With the rapid development of the semiconductor industry, micro electromechanical systems and integrated circuit (IC) technologies, the miniaturization of satellite technology is speeding up. *Figure 1.1* shows an example of 1U CubeSat developed in Kyushu Institute of Technology.

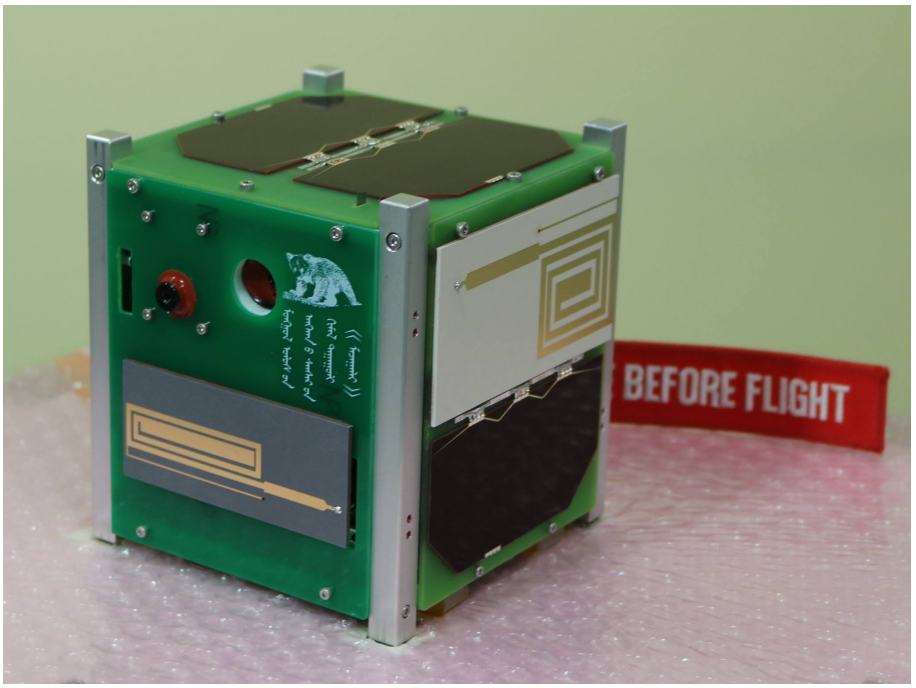

FIGURE 1.1: The Birds satellite (JGMNB project) is an example of a 1U CubeSat.

Compared with traditional Earth-observation and communication satellites, the CubeSats are more suitable for high-risk and short-term missions, and these small satellites have lower development and launch costs and shorter system development periods. These relatively inexpensive ways of launching and operating satellites has led the wide adoption of the CubeSat standard and increased the availability of small satellite launches and opened space exploration to smaller organizations, in particular university student teams. Furthermore, enabling commercial of the shell (COTS) technology in space and the significant reduced mass and less complexity are other advantages of Cubesats. Since the total required cost to build Cubesat is inexpensive than traditional satellites, the institutions and organizations may take the risk of using their own developed hardware and software for the mission and the satellite can be developed from scratch. The number of launched nanosatellites is increasing day by day and more than 1180 nanosatellites have been launched as of June 2019. *Figure 1.2* shows the number of nanosatellites that are known to have launched since 1998, and nanosatellites currently in development with expected future launch dates and with future forecasts. Plot is from the Nanosats database [4].

The CubeSats has conducted a wide range of experiments and tests, including tests and qualifications of mobile phone cameras, studies of the Radiation effect on the electronic devices and Earth-observation studies. *Table 1.1* summarizes examples of recent CubeSat missions. It is apparent that a low available volume and limited weight constraints

are major challenges that limit the range of possible missions that can be done using a nanosatellite. These size and weight restrictions limit the available payload for batteries and external solar panels, which limits the CubeSat's power consumption. Majority of these limitations effect on attitude determination and control system (ADCS) of these satellites. Unlike the traditional satellites, high accuracy high-performance attitude determination sensors and actuators such as star-trackers and reaction wheels cannot be easily used for nanosatellite missions considering they are heavy, big and do use high power consumption.

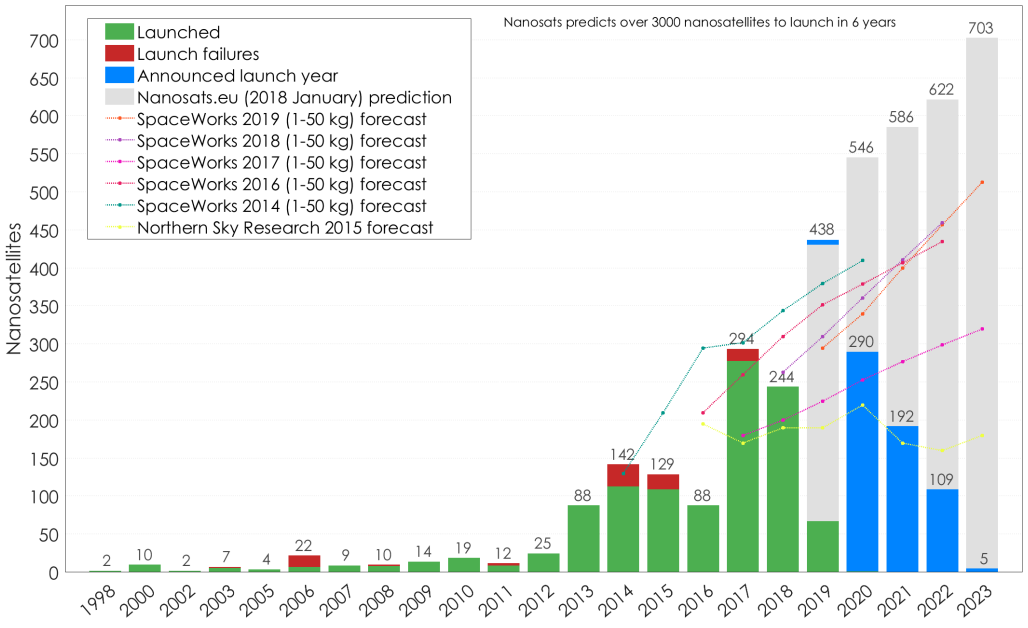

FIGURE 1.2: Yearly launched and planned CubeSats as of January 2019.

Satellite Name	**Launch date**	**Mass (kg)**	**Mission**
Phonesat 1.0	April 2013	1	Scientific research
Dove 1	April 2013	5.5	Earth imaging
ArduSat	August 2013	1	Education
BRITE-PL	November 2013	7	Astronomy
GOMX-3	August 2015	2	Technology demonstration
MinXSS	December 2015	3.5	Scientific research
Horyu-4	February 2016	10	Scientific research
Aalto-1	June 2017	3.9	Technology demonstration
Birds-1	July 2017	1.3	Technology demonstration
1-KUNS-PF	April 2018	1	Technology demonstration

TABLE 1.1: List of CubeSat missions

Small satellites often use miniaturized sun sensors, magnetometers, and Micro-Electro-Mechanical Systems (MEMS) based rate gyros to achieve the required attitude knowledge. However, these sensors have several limitations. On the other hand, miniaturized Star Trackers can provide precise attitude knowledge with a low rate in the long term. However, the star trackers increase the mission cost and the system complexity because of the requirement for a baffle. Meanwhile, 2D image sensors or cameras are cheap, lightweight, and passive, and can be a useful supplement for attitude sensors for obtaining accurate attitude measurements. The camera provides vast external information like an eye of humans and animals. Furthermore, the vestibular system of humans and animals gives inertial information for their navigation and body stabilization systems. Moreover, this information is important for several visual tasks such as gaze holding and tracking. Vision system combined with vestibular system is successful navigation and localization system that used by nature. From these humans and animals perception systems, it is apparent that such complementary sensing system can be used in small satellite's attitude determination system to combining vision sensor and tri-axial MEMS gyroscope. In our work we explore some aspects of integration of visual and inertial sensing. These complementary sensing system motivated our research to develop an approach for increased accuracy and robustness of attitude estimation. *Figure 1.3* shows a possible combination framework of visual and inertial sensing modeled as human vision and vestibular system.

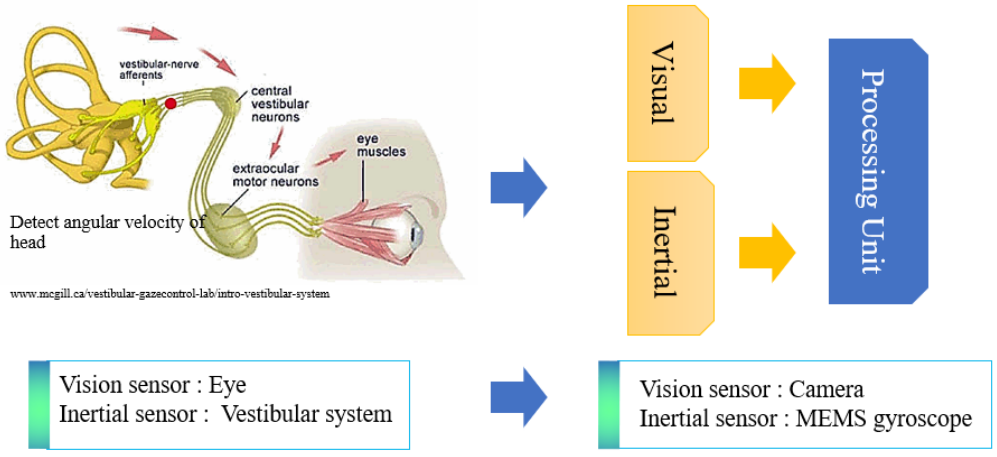

FIGURE 1.3: Combination of inertial and vision sensing modeled as human vision and vestibular system.

1.2 Literature Review

CubeSat attitude determination system's capability usually depends on the pointing requirements, the operating environment, and desired pointing accuracy among other factors. Achieving accurate and robust attitude determination and control systems in small form factor is challenging and complete attitude knowledge in inertial space requires a combination of multisensors in order to maintain robust attitude estimation in different cases. Furthermore, the spacecraft's size, weight, and power constraints are significantly limit the number of sensors that can be used in CubeSat's attitude determination subsystem. The general characteristics of CubeSats are summarized in *Table 1.2*. It is apparent that a low available volume and limited weight constraints are the major challenges of attitude determination systems on CubeSats. These size and weight restrictions limit the available payload for batteries and external solar panels, which limits the CubeSat's power consumption. For CubeSats in low-earth orbit, the need for power generation capabilities depends on orbital parameters, solar panel configurations and orientation all affect the anticipated power generation levels for solar panel systems. Also, attitude determination algorithms place additional constraints that depending on whether the algorithm is in real-time or with some latency. The real-time attitude determination algorithms are computationally intensive and require a powerful processors.

Parameters	**1U CubeSat**	**3U CubeSat**
Orbits	Low Earth Orbit	Low Eart Orbit
Mission length	90-365 days	90-365 days
Volume	10x10x10 cm	10x10x30 cm
Typical mass	1.33 kg	3.9 kg
Maximum allowable power	1-2.5 W	7-20 W

Table 1.2: Generic CubeSat characteristics.

With the rapid development of the semiconductor industry and the miniaturization of integrated circuit technologies, recently large number of compact and low-power sensors have become available. These range from micro-sized magnetometers that are simple, surface-mount circuit board components, to more specialized infrared devices using thermopiles that can measure the Earth's limb relative to cold space, and even miniature sized star trackers for high accurate attitude determination. We briefly introduce two broad classes of sensors. The first class is inertial sensors that are used to measure kinematics states of a satellite. The kinematic states they measure are angular velocity and specific forces. These measurements can be processed to yield an estimate of the CubeSat's attitude. The second class of sensors is referred to as vector sensors.

1.2.1 Inertial Sensors

Inertial sensors used to determine a subset of the kinematic state of the body to which they attached. The sensors are gyroscopes and accelerometers. Accelerometers measure specific force, the algebraic sum of linear acceleration and gravitational acceleration normalized by mass. A triad of accelerometers arranged orthogonally will measure the specific force vector of the body to which they attached. Rate gyroscopes are generally used in CubeSat attitude determination subsystem. These gyroscopes based on Micro-Electro-Mechanical Systems (MEMS) and provide angular rate measurements. Normally triad gyroscopes are packaged with triad accelerometers together to form called an inertial measurement unit (IMU). When using rate gyroscopes, satellite's attitude can be estimated by numerically integrating the following equation. This *Equation 1.1* is for the Euler angles of the ZYX rotation.

$$\begin{bmatrix} \dot{\phi} \\ \dot{\theta} \\ \dot{\psi} \end{bmatrix} = \frac{1}{\cos\theta} \begin{bmatrix} \cos\theta & \sin\phi\sin\theta & \cos\phi\sin\theta \\ 0 & \cos\phi\cos\theta & -\sin\phi\cos\theta \\ 0 & \sin\phi & \cos\phi \end{bmatrix} \begin{bmatrix} \omega_x \\ \omega_y \\ \omega_z \end{bmatrix} \tag{1.1}$$

But, low-cost MEMS gyroscopes tend to have large output errors due to its high biases, scale factor variations, drifts, and noise characteristics [10]. Accurate gyroscopes tends to be large and requires more power to operate. Therefore, gyroscopes for attitude determination in CubeSats will have to be fused with external sensors that compensate attitude drift resulting from gyroscopes output errors. Vector sensors are usually used for this purpose. Examples of two different grade IMUs are provided in *Table 1.3*.

Grade	**Gyro output error**		**Example IMU**	**Power (W)**
Consumer	Bias stability	$>10°/h$	QRS-11	0.4
-	Output noise	$0.01° \sqrt{Hz}$	AD-16405	0.6
Tactical	Bias stability	$<1°/h$	LN-200	12.0
-	Angle random walk	$0.13° \sqrt{Hz}$	HG-1700	5.0

TABLE 1.3: Examples of two different grade IMUs.

1.2.2 Vectors Sensors

There are several attitude sensors commercially available in small form that can collectively be classified as vector sensors. These sensors provide measurements of some the components of a vector that describes some physical quantity, such as magnetometers, Earth sensors, sun sensors and star trackers. These sensors are common attitude sensors

for CubeSat missions. They are cheap, light, and available as commercial of-the-shelf (COTS) equipment [5]. However, the overall achievable attitude determination accuracy is limited with these sensors, mainly because of their inherent limitations and operational cases in different space environment. On the other hand, miniaturized Star Trackers can provide precise attitude knowledge with a low rate in the long term. Here we briefly introduce Earth horizon sensors, sun sensors, magnetometers and star trackers. Also, examples of vector sensors suitable for CubeSat missions are provided in *Table 1.4*.

Sensor name	**Type**	**Mass (g)**	**Accuracy**	**Power (W)**
Nano-SSOC-D60	Sun Sensor	6.5	$<0.5^\circ$	0.08
MAI-SES	IR Earth horizon	33	$<1.0^\circ$	0.26
Honeywell HMC 1001	Magnetometer	0.14	$\approx 1-2^\circ$	0.05
MIST	Star tracker	500	$<0.008^\circ$	5.0

TABLE 1.4: Examples of attitude sensors suitable for CubeSat missions.

Sun sensors: These sensors are widely used in spacecraft altitude determination systems and provide a measurement of the line of sight vector from a CubeSat to the center of the Sun. For a given time of year and location of the satellite, this vector will be known in the inertial coordinate frame. The sun sensor's measurement's can be used to determine two of three attitude angles that describe the satellite's orientation.

Magnetometers: Most CubeSat missions have operated in Low Earth Orbit (LEO). These sensors measure the intensity of Earth's magnetic field vector. The Earth's magnetic field can be measured using on-board sensors to give a coarse sense of what the instantaneous field direction and intensity are. Using these measurements in combination with the Earth magnetic field model, satellite attitude can be determined.

Earth horizon sensors: These sensors can be used to provide the nadir vector. Based on infrared thermopile detectors, the Earth's limb sensed via the relatively warm infrared radiation that the Earth's limb emits, in contrast to the cold background of space. This measurement is used to build an estimate of the location and direction of Earth's limb and using that, provide a nadir vector estimate.

Star trackers: These sensors image visible stars in imagery's field of view (FOV) and provide complete attitude knowledge of the satellite. Star trackers used for measuring the line of sight vector to celestial objects that can be seen by the sensor. Given the line of sight vector to two stars are known in both inertial and body coordinate frames, the attitude can be determined via Wahba's problem.

1.2.3 Current State of Research

Many methods were proposed for satellite attitude estimation based on vision sensors, such as CMOS (complementary metal-oxide-semiconductor) Earth horizon sensors, Stellar gyroscopes and Image-based attitude estimation and control methods. CMOS Earth horizon sensor (EHS) tracks Earth's horizon curvature in imager's field of view (FOV) and provides roll and pitch angle measurements [6][7]. These sensors use a CMOS camera to capture Earth in visible spectrum, then use computer vision algorithms to detect the Earth horizon in the image that can provide two axis attitude knowledge respect to the Earth. The Earth horizon curvature based methods provides an absolute attitude knowledge when the horizon is visible in imager's field of view. EHSs determine the nadir vector which corresponds to a pitch and roll angle measurement of the satellite with respect to the Earth. Regarding to COTS CMOS EHS, The CubeSense sensor manufactured by CubeSpace (2016), which employed a wide FOV CMOS camera and can provide attitude knowledge with an accuracy of 0.2 degrees at 1Hz sample rate. A paper [8] that related with EHS states, the algorithm utilized a Sobel edge detection algorithm with a subsequent circle fit. Meller et al., (2000) introduced EHS with multiple CMOS cameras with 512x512 pixels sensitive to the visible spectrum. Proposed approach utilized a Threshold filter applied to scan lines which determine the horizon points then fed into a Least-Square circle fit [9]. Rensburg et al., (2008) proposed a sensor sensitive to the IR spectrum of 6.5m-20m wavelength. Proposed approach employed 32x31 pixels image sensor which can provide attitude knowledge with accuracy of 0.24 degrees (pitch) and 0.59 degrees (roll) within an FOV of 35 degrees. This approach used a sub-pixel Canny edge detection algorithm with subsequent line fit using the Least-Square method [10].

The image-based attitude estimation and control methods usually based on Earth's surface features tracking and feature-correspondences matching techniques with different outlier rejection methods and provide nominal attitude in 3 degrees of freedom (3DOF). Alessandro et al., (2009 and 2013) introduced a Vision-based method for high accuracy assessment of satellite attitude using 320x240 pixels CCD image sensor directed toward the Earth [11][12]. The authors proposed frame-to-frame registration approach which utilized Shi and Tomasi features descriptors, Phase correlation algorithm, Lukas-Kanade tracker and RANSAC outlier rejection method. Klančar et al., (2012, 2013) proposed an Image-based satellite attitude control algorithm for remote sensing satellite's attitude determination and control system [13]. The image-based control algorithm used a Scale Invariant Feature Transform (SIFT) image features to extract and match current and previous images in order to derive attitude knowledge and PD control method.

Rawashdeh et al., (2014) presented an Image-based attitude propagation for small satellites using RANSAC method [14]. The stellar gyroscope concept based on motion of stars in imager's field of view. By detecting stars in captured current image, the algorithm solves the relative attitude problem and provides satellite attitude in 3 degrees of freedom, as long as the camera is viewing the sky. This approach utilized RANSAC method on rotational kinematics to find a rotation estimate with consensus and reject the false data. Kouyama et al., (2017) proposed a Satellite attitude determination and map projection based on robust image matching approach [15]. This approach derives the satellite attitude by extracting feature points from base map and satellite captured images, matching these feature points based on SURF descriptors and removing the outliers using RANSAC method. The proposed method applied to UNIFORM-1 small satellite observations and satellite attitude was determined with accuracy of 0.02 degrees. However, a major problem with using pure vision-based approaches is that they suffer from blurred images induced by high-rate rotational motion and low update rates. On the other hand, the integration of vision-based and inertial-based approaches provides a more robust and accurate attitude estimation solution due to their complementary properties. Integration of visual and inertial sensors is inspired by human vestibular and visual systems [16]. In unmanned aerial vehicle (UAV) navigation studies, sensor fusion of visual and inertial sensors has been widely investigated [17][18]. However, regarding a small satellite's attitude determination system, most existing works related to the integration of visual and inertial sensors used the star trackers and inertial sensors [19]. There are few results to the integration of image-based attitude estimation approach and inertial sensors in the literature. Venn diagram of relevant literature topics shown in *Figure 1.4*.

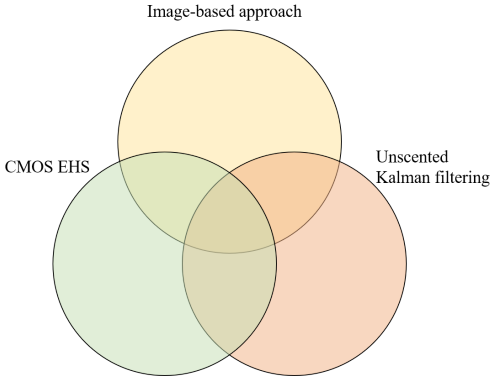

FIGURE 1.4: Venn diagram of relevant literature.

1.3 Contributions

This dissertation investigates in methods for vision-based and inertial-aided attitude determination system for small satellite. The main goal is an approach which is accurate, robust, efficient and able to provide long-term navigation of the spacecraft in different cases. This long-term goal requires intensive research in a variety of fields.This dissertation presents the following core contributions:

- Development of vision-based attitude determination and propagation algorithms that use a single camera as a sensor and provide attitude information in 3 DOF.
- Development of a multi-sensor fusion framework capable to accurately estimate satellite's attitude changes.
- Implementation and testing of the framework on realistic Earth-surface scene simulations.

With these three key-points in focus, several side-paths are explored and discussed. While the hardware design of the system, size and power requirements of Cubesats evidently plays a major role to achieve our goals, in this dissertation, we focus on the algorithmic side of the problem statement.

1.3.1 Camera as Attitude Sensor

Regarding sensors, the focus of this dissertation is on using a camera as an on-board sensor for attitude determination of small satellite. In particular, we aim at obtaining complete 3DOF attitude measurements from this sensor mounted on-board the platform.

1.3.2 Sensor Fusion and Filtering

The main contribution of this dissertation is the development, implementation and testing of a sensor fusion framework for small satellites. We focus on vision and tri-axial MEMS gyroscope as main sensors for accurate attitude measurements since these sensors are both, lightweight and low on power consumption. Although, they provide sucient information to achieve the task. Drift in attitude measurements of the satellite's state estimate would cause the satellite to abnormal operation. Therefore, it is very important to recognize and compensate for such drifts. Here, we analyze our sensor fusion framework in order to eliminate dierent drift sources.

1.4 Structure of this Dissertation

This introduction is followed in Chapter 2 by a discussion of theoretical background relevant to this dissertation and includes the review of related attitude determination algorithms and approaches. Furthermore, attitude reference frames and attitude representation forms used in the algorithm development, analysis, and illustrations are described. Chapter 3 addresses the our Earth horizon based approach implemented in this work. The used hardware, image processing methods, results of the experiments of this approach and simulations are described. In Chapter 4 we present vision based and visual-inertial approaches. This chapter first gives the description of image processing methods which are used in the vision based approach. Also, we present our sensor fusion framework that integrates visual and inertial sensors measurement information to improve the accuracy of attitude estimation. As a basis for building the sensor fusion framework, the Unscented Kalman Filter (UKF) and its implementation method for attitude estimation are given. Moreover, we test our previously theoretically analyzed visual-inertial method on realistic Earth-surface scene simulations and precise rotary table. The experimental setup for the visual-inertial based attitude estimation approach is given. A comparison of performance evaluation for the only vision-based and visual-inertial based attitude estimation approaches is also included. The dissertation itself is concluded in Chapter 5, where conclusions and the discussions of the experimental results of our proposed approach presented. The results are evaluated regarding the main aim of this dissertation and analyzed. Finally, the concluding remarks and recommendations for the future work are given.

Chapter 2

Background

2.1 Satellite Mathematical Models

2.1.1 Coordinate Systems

The coordinate systems used in this thesis are the satellite body frame, which matches with the principal axes of inertia of the satellite, orbit reference frame and inertial reference frame which is Earth centered. The definitions of these coordinate systems are given below.

Earth-Centered Earth-Fixed Frame (ECEF)

This reference frame is earth-centered, having a z-axis that lines up with the earth spin axis pointing towards the celestial north pole. The x-axis extends to the zero latitude and longitude point, i.e. the intersection of the Equator and the prime meridian passing through Greenwich, UK. The y-axis is such that it completes the right hand rule. The ECEF frame is convenient to describe phenomena that are earth-fixed, such as ground stations, earth targets, and the geomagnetic field.

Earth-Centered Inertial Frame (ECI)

This reference frame is earth-centered, with the z-axis towards the celestial north pole. The x-axis points towards the Vernal Equinox, which is the intersection of the ecliptic plane with the equatorial plane at the ascending node. The y-axis completes the right hand rule.

Satellite Body Frame

The origin of the frame is located at the centre of mass of the satellite. The axes are directed towards the principal inertial axes of the spacecraft. Three parameters named as Euler angles set the condition of the body frame related to the orbital coordinate system. When the direction cosine matrix is identity matrix the satellite body frame matches with the orbital frame.

Camera Reference Frame

The origin of the frame is at the mass centre of the spacecraft. The z axis is in nadir direction (towards the centre of the Earth) and the y axis is tangential to the orbit (aligns with velocity vector of the spacecraft in case of circular orbit). The x axis completes to the orthogonal right hand system.

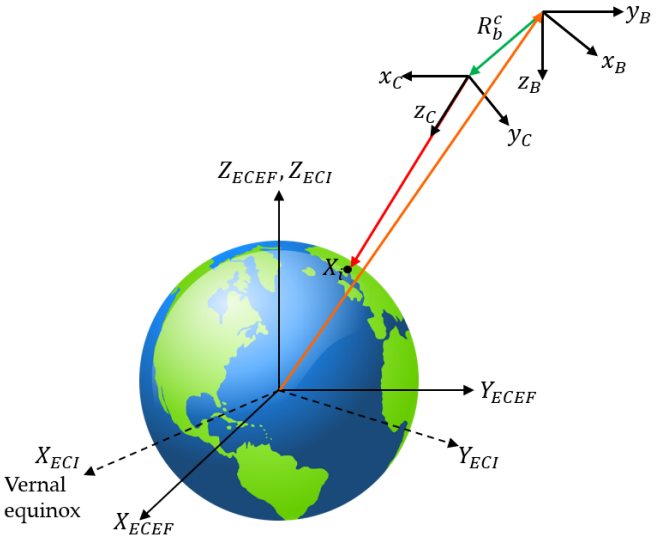

FIGURE 2.1: Definition of coordinate systems.

The coordinate systems used in the proposed approach include the Earth-Centered Inertial (ECI) coordinate system, the Earth-Centered, Earth-Fixed (ECEF) coordinate system, Camera coordinate system referred as C, and Body coordinate system referred as B. The Camera coordinate system is fixed with the camera and a center of the image detector acts as a center of the camera coordinate system. The camera is rigidly attached to mechanical structures and the line of sight of the camera is oriented to the Earth's surface. The Z, X, and Y axes of the Camera coordinate system satisfy the right-hand rule. *Figure 2.1* shows a definition of the coordinate systems. World point X_i is the intersection of the Earth's surface and the camera's line-of-sight unit vector in the ECI coordinate system. The line-of-sight unit vector of the camera can be defined from the current satellite position, camera transformation matrix R_b^c and attitude matrix R_i^b as follows:

$$L = (R_b^c R_i^b)^{-1} \begin{bmatrix} 0 \\ 0 \\ 1 \end{bmatrix}_{cam} \tag{2.1}$$

$$X_{ECI} = P_{ECI} - Z_s L \tag{2.2}$$

where L is a line-of-sight unit vector, Z_s a factor that denes the length of the line-of-sight and the $z_C$is is always pointed along the line-of-sight, and P_{ECI} defines the current position of satellite obtained from GPS. The relative position of the world point X_i in the ECEF coordinate system can obtained as:

$$X_{ECEF} = \begin{bmatrix} \cos\omega_E t & \sin\omega_E t & 0 \\ -\sin\omega_E t & \cos\omega_E t & 0 \\ 0 & 0 & 1 \end{bmatrix} X_{ECI} \tag{2.3}$$

where t is the Greenwich Sidereal Time.

2.1.2 Attitude Representations

Attitude is the orientation the satellite has relative to a frame of reference. Three terms commonly used describe the satellite's attitude: pitch, yaw, and roll :

- Moving the nose up and down is referred to as pitch.

- Moving the nose left and right is referred to as yaw.

- Rotating the nose clockwise or counterclockwise is referred to as roll.

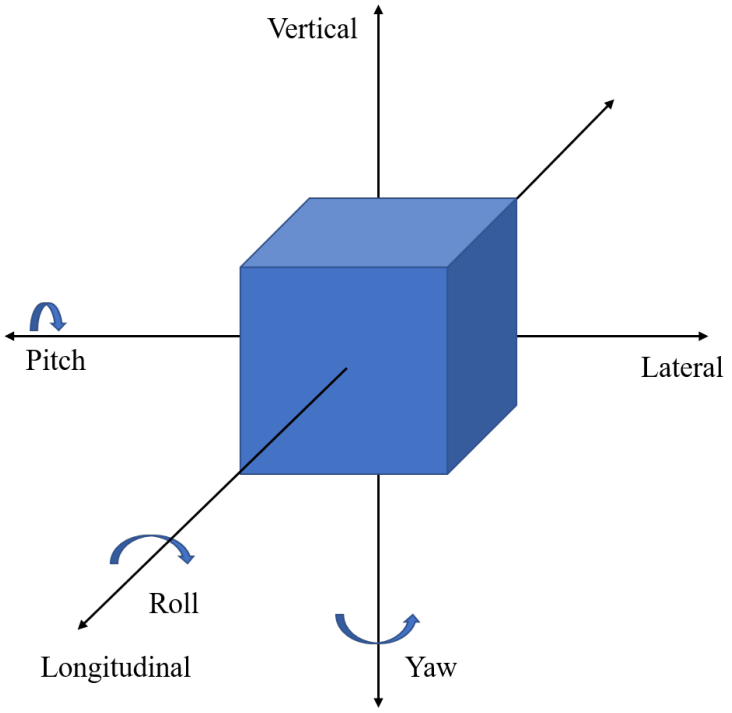

FIGURE 2.2: Definition of coordinate systems.

Mathematicians have developed many ways to represent rotation, two of commonly used techniques are Euler angles and Quaternions. In this dissertation, one of these two representation methods have been preferred for the construction of the mathematical model of the satellite, depending to the estimation algorithm. Related to their application area, Euler angles and quaternions may be more convenient than each other. Following table represents a brief comparison between them [5].

Representation	**Number of Parameters**	**Advantages**	**Disadvantages**
Euler Angles	3	No redundant parameters Clear physical interpretation Minimal set	Trigonometric functions in both rotation matrix and kinematic relations Singular for specific rotations No convenient product rule
Quaternions	4	Convenient product rule Simple kinematic relation No singularities	No clear physical interpretation One redundant parameter

TABLE 2.1: Characteristics of attitude representations of Euler angles and quaternions.

Euler Angles

A transformation from one coordinate frame to another can be carried out by three consecutive rotations about different axes. While describing the rotation of the axis with respect to another one, rotation matrixes formed by Euler angles are used. The direction cosine matrix of transformation will be the product of these three matrices. According to [5] there are 12 possible Euler angle representations and so direction cosine matrixes for transformation. They are categorized in two as:
- Case where three successive rotations take place around three different axes.
- In this case first and third rotations are performed around same axis and the second one takes place about one of the other two axes.

Euler angles for vector transformation

Suppose that $\psi \rightarrow \theta \rightarrow \phi$ rotation order about z, y and x axes, which may be also referred as 3-2-1 Euler angle rotation is followed. That means;

- a rotation ψ about z axis and a rotation matrix of,

$$A_3 = \begin{bmatrix} \cos(\psi) & \sin(\psi) & 0 \\ -\sin(\psi) & \cos(\psi) & 0 \\ 0 & 0 & 1 \end{bmatrix} \tag{2.4}$$

- a rotation θ about y axis and a rotation matrix of,

$$A_2 = \begin{bmatrix} \cos(\theta) & 0 & -\sin(\psi) \\ 0 & 1 & 0 \\ \sin(\theta) & 0 & \cos(\theta) \end{bmatrix} \tag{2.5}$$

- a rotation φ about x axis and a rotation matrix of,

$$A_1 = \begin{bmatrix} 1 & 0 & 0 \\ 0 & \cos(\varphi) & \sin(\varphi) \\ 0 & -\sin(\varphi) & \cos(\varphi) \end{bmatrix} \tag{2.6}$$

Then the direction cosine matrix (DCM) that is used for transformation from reference to body frame can be obtained as the product of these three matrices.

$$A_{321} = [A_1][A_2][A_3] = \begin{bmatrix} c(\theta)c(\psi) & c(\theta)c(\psi) & -s(\theta) \\ -c(\varphi)s(\psi) + s(\varphi)s(\theta)c(\psi) & c(\varphi)c(\psi) + s(\varphi)s(\theta)s(\psi) & s(\varphi)c(\theta) \\ s(\varphi)s(\psi) + c(\varphi)s(\theta)c(\psi) & -s(\varphi)c(\varphi) + c(\varphi)s(\theta)s(\psi) & c(\varphi)c(\theta) \end{bmatrix} \tag{2.7}$$

Here $c(\cdot)$ and $s(\cdot)$ represent the cosines and sinus functions. Per contra, matrix, which transforms a vector from body to reference frame, is simply the transpose of this matrix as $A_{321}^T = [A_3]^T[A_2]^T[A_1]^T$. Besides, for the small angle rotations, the sinus functions become $\sin(\psi) \rightarrow \psi, \sin(\theta) \rightarrow \theta, \sin(\varphi) \rightarrow \varphi$ as well as the cosines functions approaches to the unity. When these approximations are used and the products of angles, which become insignificant, are ignored as $\psi\theta = \varphi\theta = \cdots = 0$, then the skew symmetric direction cosine matrix for small angles can be gained.

$$A_{321} = \begin{bmatrix} 1 & \psi & -\theta \\ -\psi & 1 & \varphi \\ \theta & -\varphi & 1 \end{bmatrix} \tag{2.8}$$

Propagation of Euler angles by time

In order to find kinematic equations, which relate the Euler angles with the angular velocities in body frame, first, derivatives of the Euler angles must be transformed to the body angular rates.

$$\begin{bmatrix} p \\ q \\ r \end{bmatrix} = [A_1][A_2][A_3] \begin{bmatrix} 0 \\ 0 \\ \dot{\psi} \end{bmatrix} + [A_1][A_2] \begin{bmatrix} 0 \\ \dot{\theta} \\ 0 \end{bmatrix} + [A_1] \begin{bmatrix} \dot{\varphi} \\ 0 \\ 0 \end{bmatrix} \tag{2.9}$$

After the matrix multiplications;

$$p = \dot{\varphi} - \dot{\psi} \sin(\theta) \tag{2.10}$$

$$q = \dot{\theta} \cos(\varphi) + \dot{\psi} \cos(\theta) \sin(\varphi) \tag{2.11}$$

$$r = \dot{\psi} \cos(\theta) \cos(\varphi) - \dot{\theta} \sin\varphi \tag{2.12}$$

If these equations are solved for $\dot{\varphi}$, $\dot{\theta}$ and $\dot{\psi}$, then the kinematic equation via Euler angles can be determined.

$$\dot{\varphi} = p + \sin(\varphi) \tan(\theta) q + \cos(\varphi) \tan(\theta) r \tag{2.13}$$

$$\dot{\theta} = \cos(\varphi) p - \sin(\varphi) q \tag{2.14}$$

$$\dot{\psi} = \sin(\varphi) / \cos(\theta) q + \cos(\varphi) / \cos(\theta) r \tag{2.15}$$

Quaternions

The quaternion attitude representation is a technique based on the idea that a transformation from one coordinate frame to another may be performed by a single rotation about a vector $\vec{e}$ defined with respect to the reference frame. The quaternion, denoted here by the symbol $\vec{q}$, is a four element vector, the elements of which are functions of vector and the magnitude of the rotation,Φ:

$$q_1 = e_1 \sin(\frac{\Phi}{2}) \tag{2.16}$$

$$q_2 = e_2 \sin(\frac{\Phi}{2}) \tag{2.17}$$

$$q_3 = e_3 \sin(\frac{\Phi}{2}) \tag{2.18}$$

$$q_4 = \cos(\frac{\Phi}{2}) \tag{2.19}$$

Here e_1, e_2, e_3 are the components of the vector $\vec{e}$ which is to be rotated around with an angle of Φ. As a result by the use of quaternions a transfer from reference frame to body frame can be denoted by a single rotation around a vector defined in the reference frame.

A quaternion with components q_1, q_2, q_3 and q_4 may also be expressed as a four parameter complex number with a real component q_4 and theree imaginary components q_1, q_2 and q_3 as follows:

$$\vec{q} = q_4 + iq_1 + jq_2 + kq_3 \tag{2.20}$$

where i, j, k are hyper-imaginary numbers with characteristics of;

$$i^2 = j^2 = k^2 = -1 \tag{2.21}$$

$$ij = -ji = k \tag{2.22}$$

$$jk = -kj = i \tag{2.23}$$

$$ki = -ik = j \tag{2.24}$$

Also, redundancy of quaternions must be noted as

$$q_1^2 + q_2^2 + q_3^2 + q_4^2 = 1 \tag{2.25}$$

Quaternions for vector transformation

A vector quantity defined in body axes, r_B may be expressed in reference axes as r_R using the quaternion directly. First define a quaternion, r_B^q, in which the complex components are set equal to the components of r_B, and with a zero scalar component, that is, if:

$$r_B = ix + jy + kz \tag{2.26}$$

$$r_B^q = 0 + ix + jy + kz \tag{2.27}$$

This is expressed in reference axes as r_R^q using:

$$r_R^q = \vec{q} r_B^q \vec{q}^* \tag{2.28}$$

where $\vec{q}^* = q_4 - iq_1 - jq_2 - kq_3$, the complex conjugate of $\vec{q}$.

Hence,

$$\begin{aligned} r_R^q &= (q_4 + iq_1 + jq_2 + kq_3)(0 + ix + jy + kz)(q_4 - iq_1 - jq_2 - kq_3) = \\ &= 0 + (q_4^2 + q_1^2 - q_2^2 + q_3^2)x + 2(q_1q_2 - q_4q_3)y + 2(q_1q_3 - q_4q_2)zi + \\ &+ 2(q_1q_2 + q_4q_3)x + (q_4^2 - q_1^2 + q_2^2 - q_3^2)y + 2(q_2q_3 - q_4q_1)zj + \\ &+ 2(q_1q_3 - q_4q_2)x + 2(q_2q_3 + q_4q_1)y + (q_4^2 - q_1^2 + q_2^2 - q_3^2)zk \end{aligned}$$

Alternatively, r_R^q may be expressed in matrix form as follows

$$r_R^q = A' r_B^q \tag{2.29}$$

where $A' = \begin{bmatrix} 0 & 0 \\ 0 & A \end{bmatrix}$, $r_R^q = \begin{bmatrix} 0 & r_B \end{bmatrix}$ and

$$A_= \begin{bmatrix} q_1^2 - q_2^2 - q_3^2 + q_4^2 & 2(q_1q_2 + q_3q_4) & 2(q_1q_3 - q_2q_4) \\ 2(q_1q_2 - q_3q_4) & -q_1^2 + q_2^2 - q_3^2 + q_4^2 & 2(q_2q_3 + q_1q_4) \\ 2(q_1q_3 + q_2q_4) & 2(q_2q_3 - q_1q_4) & -q_1^2 - q_2^2 + q_3^2 + q_4^2 \end{bmatrix} \tag{2.30}$$

which is equivalent to writing:

$$r_R^q = A r_B \tag{2.31}$$

Here A is the same direction cosine matrix that is used for transformation from body to reference frame.

Propagation of quaternions by time

While defining the kinematic equations of motion with quaternions, time dependence of them must be used and that can be derived from the product relation [**4**]. Multiplication of quaternion is performed in a way not too different from complex number multiplications. However the order of the process must be regarded. By using characteristic of

hyper-imaginary numbers:

$$\vec{q}'' = \vec{q}\vec{q}' = (q_4 + iq_1 + jq_2 + kq_3)(q'_4 + iq'_1 + jq'_2 + kq'_3) \tag{2.32}$$

$$\vec{q}'' = -q_1q'_1 - q_2q'_2 - q_3q'_3 + q_4q'_4$$

$$i(q_1q'_4 + q_2q'_3 - q_3q'_2 + q_4q_1 +$$

$$+j(-q_1q'_3 + q_2q'_4 + q_3q'_1 + q_4q'_2) +$$

$$+k(q_1q'_2 - q_2q'_1 + q_3q'_4 + q_4q'_3)$$

If it is written in matrix form,

$$\begin{bmatrix} q''_1 \\ q''_2 \\ q''_3 \\ q''_4 \end{bmatrix} = \begin{bmatrix} q'_4 & q'_3 & -q'_2 & q'_1 \\ -q'_3 & q'_4 & q'_1 & q'_2 \\ q'_2 & -q'_1 & q'_4 & q'_3 \\ -q'_1 & -q'_2 & -q'_3 & q'_4 \end{bmatrix} \begin{bmatrix} q_1 \\ q_2 \\ q_3 \\ q_4 \end{bmatrix} \tag{2.33}$$

Now assume that, $\vec{q}$ and $\vec{q}''$ correspond to the orientation of the body at t and $t + \Delta t$, respectively. Also $\vec{q}'$ is for the representation of position at $t + \Delta t$ in a relative way to the position that has been occupied at t.

$$q'_1 \equiv e_1 \sin(\frac{\Delta\Phi}{2}) \tag{2.34}$$

$$q'_2 \equiv e_2 \sin(\frac{\Delta\Phi}{2}) \tag{2.35}$$

$$q'_3 \equiv e_3 \sin(\frac{\Delta\Phi}{2}) \tag{2.36}$$

$$q'_4 \equiv \cos(\frac{\Delta\Phi}{2}) \tag{2.37}$$

When the necessary multiplication is done it is obvious that

$$\vec{q}(t + \Delta t) = \left\{ \cos(\frac{\Delta\Phi}{2})I + \sin(\frac{\Delta\Phi}{2}) \begin{bmatrix} 0 & e_3 & -e_2 & e_1 \\ -e_3 & 0 & e_1 & e_2 \\ e_2 & -e_1 & 0 & e_3 \\ -e_1 & -e_2 & -e_3 & 0 \end{bmatrix} \right\} \vec{q}(t) \tag{2.38}$$

where e_1, e_2, e_3 are the components of rotation axis unit vector and I is the $4x4$ identity matrix. After that by small angle approximation

$$\cos\left(\frac{\Delta\Phi}{2}\right) \approx 1 \tag{2.39}$$

$$\sin\left(\frac{\Delta\Phi}{2}\right) \approx \frac{1}{2}\vec{\omega}_{BR}\Delta t \tag{2.40}$$

It is possible to show that

$$\vec{q}(t+\Delta t) = \left\{ I + \frac{1}{2} \begin{bmatrix} 0 & r & -q & p \\ -r & 0 & p & q \\ q & -p & 0 & r \\ -p & -q & -r & 0 \end{bmatrix} \Delta t \right\} \vec{q}(t) \tag{2.41}$$

here p, q, r are components of $\vec{\omega}_{BR}$ and they indicate angular velocity of the rigid body with respect to the reference frame. Hence if a skew-symmetric matrix is defined as

$$\Omega(\vec{\omega}_{BR}) = \begin{bmatrix} 0 & r & -q & p \\ -r & 0 & p & q \\ q & -p & 0 & r \\ -p & -q & -r & 0 \end{bmatrix} \tag{2.42}$$

equation becomes

$$\vec{q}(t+\Delta t) \approx \left\{ I + \frac{1}{2}\Omega(\vec{\omega}_{BR})\Delta t \right\} \vec{q}(t) \tag{2.43}$$

Finally it is known that

$$\frac{d\vec{q}(t)}{dt} \cong \frac{\vec{q}(t+\Delta t) - \vec{q}(t)}{\Delta t} = \frac{1}{2}\Omega\vec{q}(t) \tag{2.44}$$

Euler angles and quaternions relationship

Quaternions can be expressed in terms of Euler angles as well as angles can be used to define quaternions. Formulas used for transformation are simple and given below:

- Euler Angle to Quaternion:

$$\begin{bmatrix} q_1 \\ q_2 \\ q_3 \\ q_4 \end{bmatrix} = \begin{bmatrix} \cos\frac{\theta}{2}\cos\frac{\psi}{2}\sin\frac{\varphi}{2} - \sin\frac{\theta}{2}\sin\frac{\psi}{2}\cos\frac{\varphi}{2} \\ \sin\frac{\theta}{2}\cos\frac{\psi}{2}\sin\frac{\varphi}{2} + \cos\frac{\theta}{2}\sin\frac{\psi}{2}\cos\frac{\varphi}{2} \\ \sin\frac{\theta}{2}\cos\frac{\psi}{2}\cos\frac{\varphi}{2} + \cos\frac{\theta}{2}\sin\frac{\psi}{2}\sin\frac{\varphi}{2} \\ \cos\frac{\theta}{2}\cos\frac{\psi}{2}\cos\frac{\varphi}{2} - \sin\frac{\theta}{2}\sin\frac{\psi}{2}\sin\frac{\varphi}{2} \end{bmatrix} \tag{2.45}$$

- Quaternion to Euler Angle:

$$\varphi = \sin^{-1}\left(2(q_2q_3 + q_1q_4)\right) \tag{2.46}$$

$$\theta = \tan^{-1}\frac{q_3 + q_2}{q_4 + q_1} + \tan^{-1}\frac{q_3 - q_2}{q_4 - q_1} \tag{2.47}$$

$$\psi = \tan^{-1}\frac{q_3 + q_2}{q_4 + q_1} - \tan^{-1}\frac{q_3 - q_2}{q_4 - q_1} \tag{2.48}$$

2.1.3 Sensors Models

The Measurement Model for Gyroscopes

The on-board triad rate gyros measure the angular velocity of the body frame with respect to the inertial frame. Widely used model [20][21] for the gyro measurement is given as

$$\omega_{mea} = \omega + \varepsilon + \eta_1 \tag{2.49}$$

where ω_{mea} is the measured angular velocity of the satellite, ε is a bias of the gyro and η_1 represents a zero-mean Gaussian white noise characteristic of

$$E[\eta_{1k}\eta_{1j}^T] = I_{3\times3}\sigma_v^2\delta_{kj} \tag{2.50}$$

where σ_v is the standard deviation of each gyro random error, δ_{kj} is the Kronecker symbol and $I_{3\times3}$ is the identity matrix with the dimension of 3×3. Furthermore, the dynamics of the non-static bias of the gyro is modelled as a random walk process

$$\dot{\varepsilon} = \eta_2 \tag{2.51}$$

where η_2 represents a zero-mean Gaussian white noise characteristic of

$$E[\eta_{2k}\eta_{2j}^T] = I_{3\times3}\sigma_u^2\delta_{kj} \tag{2.52}$$

Here, σ_u is the standard deviation of gyro biases. Moreover, the estimated angular velocity is given by

$$\hat{\omega} = \omega_{mea} + \hat{\varepsilon} \tag{2.53}$$

here, the circumflex $\hat{}$ means estimated value for a variable.

The Camera Model

The basic pinhole camera model is selected in this chapter to infer the mapping between a 2D point in image coordinates and a 3D point in camera coordinates, which is based on triangle similarity as given in *Equation 2.54* and *Equation 2.55*.

$$x = fX/Z \tag{2.54}$$

$$y = fY/Z \tag{2.55}$$

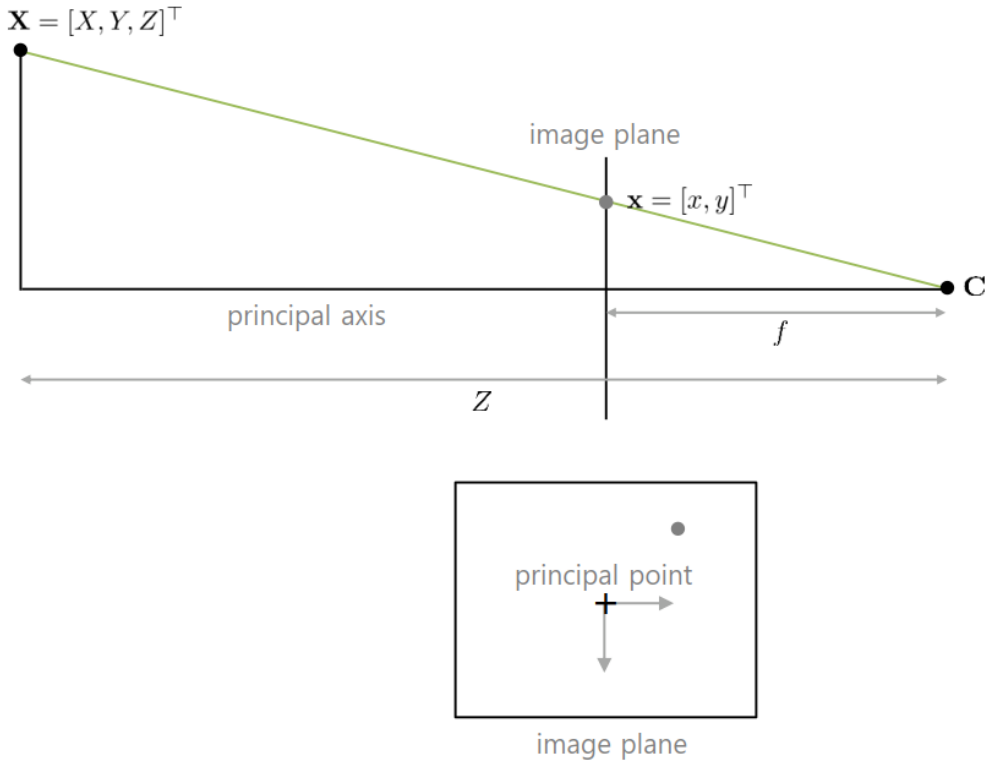

FIGURE 2.3: The Pinhole Camera Model.

By introducing homogeneous coordinates, previous equations can be written as a matrix multiplication denoted in *Equation 2.56*.

$$\begin{bmatrix} x \\ y \\ 1 \end{bmatrix} = s \times \begin{bmatrix} fX/Z \\ fY/Z \\ 1 \end{bmatrix} = s \times \begin{bmatrix} f & 0 & 0 & 0 \\ 0 & f & 0 & 0 \\ 0 & 0 & 1 & 0 \end{bmatrix} \begin{bmatrix} X \\ Y \\ Z \\ 1 \end{bmatrix} \tag{2.56}$$

where s is introduced as nonzero scale. The coordinates of a digital image are typically specified in pixels indexed from the top left corner. In order to describe a projected point in the pixel coordinate system p, the camera's intrinsic parameters have to be accounted for [22]. Therefore, *Equation 2.54* and *Equation 2.55* can be rewritten as

$$u = k_x x + c_x \tag{2.57}$$

$$v = k_y y + c_y \tag{2.58}$$

where k_x and k_y denote the number of pixels per unit of length (pixel/length) in x and y direction. Based on previous equations, the relationship between $(x, y)T$ and $(u, v)T$

can be easily described in *Equation 2.59*.

$$\begin{bmatrix} u \\ v \\ 1 \end{bmatrix} = \begin{bmatrix} k_x & 0 & c_x \\ 0 & k_y & c_y \\ 0 & 0 & 1 \end{bmatrix} \begin{bmatrix} X \\ Y \\ Z \\ 1 \end{bmatrix} \tag{2.59}$$

Combining Equation *Equation 2.56* and *Equation 2.59*, the mapping from the 3D point in camera coordinates to its corresponding 2D point in pixel coordinates can be easily expressed as follows using the camera's intrinsic calibration matrix K [37].

$$\begin{bmatrix} u \\ v \\ 1 \end{bmatrix} = \begin{bmatrix} k_x & 0 & c_x \\ 0 & k_y & c_y \\ 0 & 0 & 1 \end{bmatrix} \begin{bmatrix} X \\ Y \\ Z \\ 1 \end{bmatrix} = s\times \begin{bmatrix} f_x & 0 & c_x & 0 \\ 0 & f_y & c_y & 0 \\ 0 & 0 & 1 & 0 \end{bmatrix} \begin{bmatrix} X \\ Y \\ Z \\ 1 \end{bmatrix} = s\times K\times \begin{bmatrix} X \\ Y \\ Z \\ 1 \end{bmatrix} \tag{2.60}$$

where f_x and f_y are the so-called focal distances, which are derived from the focal length f multiplied by k_x and k_y respectively. After camera modeling and calibration, the baseline b between two consecutive images can be obtained for position estimation.

Measurement Models of the Vision-Based Method

The vision-based method provides direct measurements for the UKF framework. The measurement equations for the vision-based sensor is given as follows:

$$\varphi_{mea} = \varphi_0 + \varphi + v_\varphi \tag{2.61}$$

$$\theta_{mea} = \theta_0 + \theta + v_\theta \tag{2.62}$$

$$\psi_{mea} = \psi_0 + \psi + v_\psi \tag{2.63}$$

where φ_0, θ_0 and ψ_0 represent roll, pitch and yaw angle measurements of the spacecraft estimated by the absolute attitude sensor which used in the vision-based method as initial attitude measurements and v_φ, v_θ, and v_ψ represent the Gaussian white noise that containing all the remaining unmodeled effects. In order to fuse visual and inertial measurements into the UKF framework, the sensor measurements have to be synchronized. The proposed approach utilized time synchronized image acquisitions and inertial measurements. In addition, visual and inertial sensors are rigidly attached to the prototype's mechanical structure and relative rotation remains constant. After determining the relative rotation, the vision-based method's measurements were transformed and fused within the UKF framework with the triad rate gyro's measurements.

2.1.4 Equations of Motion

The kinematics equation of motion of the satellite via the quaternion attitude representation can be given as [5],

$$\dot{q}(t) = \frac{1}{2}\Omega(\omega_{BR}(t))q(t) \tag{2.64}$$

Here, q is the quaternion formed of four attitude parameters, $q = [q_1 q_2 q_3 q_4]^T$. First three of the terms represent the vector part and the last one is the scalar term, so we can rewrite the quaternion as $q = [g^T q_4]^T$ and $g = [q_1 q_2 q_3]^T$. Moreover in *Equation 2.64*, $\Omega(\omega_{BR})$ is the skew-symmetric matrix as

$$\Omega(\omega_{BR}) = \begin{bmatrix} 0 & \omega_3 & -\omega_2 & \omega_1 \\ -\omega_3 & 0 & \omega_1 & \omega_2 \\ \omega_2 & -\omega_1 & 0 & \omega_3 \\ -\omega_1 & -\omega_2 & -\omega_3 & 0 \end{bmatrix} \tag{2.65}$$

where, ω_1, ω_2 and ω_3 are the components of BR vector, which indicates the angular velocity of the body frame with respect to the reference frame. On the other hand, the body angular rate vector with respect to the inertial axis frame should be stated separately as $\omega_{BR} = [\omega_x \omega_y \omega_z]^T$. ω_{BI} and ω_{BR} can be related via

$$\omega_{BR} = \omega_{BI} - A \begin{bmatrix} 0 & -\omega_o & 0 \end{bmatrix}^T \tag{2.66}$$

Here, ω_o denotes the angular velocity of the orbit with respect to the inertial frame, found as $\omega_o = (\mu/r^3)^{1/2})$ for a circular orbit using μ , the gravitational constant and r, the distance between the centre of mass of the satellite and the Earth. In *Equation 2.66*, A is the attitude matrix that is related to the quaternions by

$$A = (q_4^2 - g^2)I_{3\times 3} + 2gg^T - 2q_4[g\times] \tag{2.67}$$

$I_{3\times 3}$ is the identity matrix with the dimension of 3×3 and $[g\times]$ is the skew-symmetric matrix given as,

$$[g\times] = \begin{bmatrix} 0 & -g_3 & g_2 \\ g_3 & 0 & -g_1 \\ -g_2 & g_1 & 0 \end{bmatrix} \tag{2.68}$$

In case of using quaternions for the kinematic modeling of the satellite's motion, the attitude filtering algorithms cannot be implemented straightforwardly. The reason of

such drawback is the constraint of quaternion unity given by $q^T q = 1$. If the kinematics *Equation 2.64* is used in the filter directly, then there is no guarantee that the predicted quaternion mean of the filter will satisfy this constraint.

Moreover, the dynamic equations of the satellite can be derived based on the Euler's equations

$$J\frac{\omega_{BI}}{dt} = N_t - \omega_{BI} \times (J\omega_{BI}) \tag{2.69}$$

where J is the inertia matrix consists of principal moments of inertia as $J = diag(J_x, J_y, J_z)$ and N_d is the vector of environmental disturbance torques affecting the satellite which can be given as a sum of

$$N_d = N_{gg} + N_{ad} + N_{sp} + N_{md} \tag{2.70}$$

where:
N_{gg} is the gravity gradient torque,
N_{ad} is the aerodynamic disturbance torque,
N_{sp} is the solar pressure disturbance torque,
N_{md} is the residual magnetic torque that is caused by the interaction of the satellite's residual dipole and the Earth's magnetic field.

2.2 Attitude Determination and Control System

The ADCS subsystem includes both the components used for attitude determination and attitude control. This subsystem is primarily used for guidance, navigation, and control applications. With limited the volume and power requirements of small satellites, ADCS subsystem has to occupy less space and consume low power. Earlier launched CubeSats used simple ADCS, which requires a low pointing accuracy. However, due to the increasing complexity of small satellite missions, ADCS has become more and more critical for mission success. In recent years, the usage of relatively high-performance hardware for ADCS of small satellite increasing due to miniaturization of satellite technology components and availability of advanced technologies [23]. In case of achieving a more precise pointing and stabilization, the attitude knowledge would be determined by employing a good combination of attitude sensors, proper attitude determination algorithms, attitude actuators and proper control schemes. *Figure 2.4* shows a typical attitude determination and control system block diagram for a satellite equipped with the sensors and actuators. Here, the yellow shaded block for attitude determination system in the ADCS subsystem. The attitude determination system processes sensor data and form an estimate of the vehicle's attitude. The control system compares this estimate to the desired attitude estimate. If there is a discrepancy between the two attitude estimates, the control system applies torques to change the attitude of the satellite. Torques are applied until the desired and estimated are close so that the measurement error is minimized.

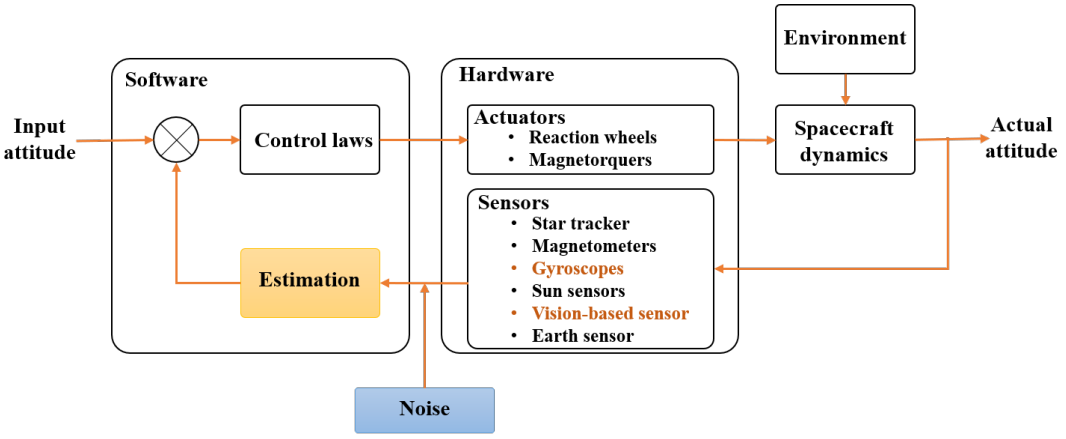

FIGURE 2.4: A generic attitude determination and control system block diagram.

2.2.1 Attitude Determination Algorithms

It is common for small satellites to obtain more accurate attitude estimation by combining the low-cost COTS attitude sensors. In order to handle this rough information, ADCS has to utilize the proper attitude determination algorithms. Here we briefly introduce Batch Estimation approaches and Advanced attitude filters that widely used in CubeSat attitude determination system. Following algorithms most common used and solves the relevant attitude determination problems:

Batch Estimation approaches
- TRIAD algorithm
- Q-method
- QUEST algorithm

Advanced attitude filters
- Complementary Filters
- Extended Kalman Filter
- Unscented Kalman Filter

The TRIaxial Attitude Determination algorithm (TRIAD) has been widely used in small satellites to determine attitude from set of 2 nonparallel vector measurements [15]. The two vectors are typically the unit vector to the Sun and the Earth's magnetic field vector for coarse "Sun-Mag" attitude determination. By utilizing TRIAD algorithm, combination of the Sun and the Earth's magnetic field vectors yields coarse attitude knowledge. However, when the two vector measurements are not accurate enough, TRIAD algorithm cannot provide accurate attitude knowledge to meet the requirements of payloads. In order to overcome this limitation, Kalman Filter would be used to improve the output attitude. The sensor fusion capability of Kalman filter, which makes a more accurate sensor out of a combination of various sensors [21]. The main purposes of the Kalman filter are the estimation of state variables and noise removal in measurement. The Kalman filter has been developed as an algorithm for a linear system, hence it cannot be applied to a nonlinear system. However, most of the systems are inherently nonlinear in nature. Extended Kalman Filter (EKF) is a representative algorithm for a Kalman filter being expanded and applied to a nonlinear system [24]. By utilizing Jacobian, EKF linearizes the nonlinear model. This process allows EKF to apply on nonlinear systems. Furthermore, another popular substitute for EKF is an Unscented Kalman filter (UKF). UKF is mainly based on Unscented Transformation (UT) and free from the problem of divergence which is caused by linear model obtained through Jacobian. The UT takes a unique approach which eliminates the linearization process [25][26]. UKF is widely used for larger satellite attitude estimation and recently proposed for small satellite attitude

determination. Kasper et al., (2011) proposed the approach that implemented quaternion representation of UKF for 3U CubeSat attitude determination [27]. The proposed UKF approach used measurements of a sun vector, magnetic field vector and angular velocity. Li et al., (2013), presented Adaptive UKF (AUKF) for a 3U CubeSat. The AUKF approach used the measurements of three axis magnetometer and three axis MEMS gyroscopes. This approach showed a good convergence time and estimation accuracy [28]. Vlad et al., (2015) introduced the implementation of UKF on a 3U CubeSat. The proposed UKF approach used low-rate attitude motion star trackers and achieved accuracy of 1 arcminute [29].

Chapter 3

Earth-horizon based Approach

3.1 Overview

This chapter describes our Earth-horizon based approach that estimates the small satellite's attitude based on the Earth's horizon image using low-cost vision sensor. An Earth horizon-based method - we highlight our image processing algorithm that tracks Earth's horizon curvature in the imager's field of view (FOV) and provides roll and pitch angle measurements. The first part of this chapter discusses theoretical background relevant to this work and includes the literature review of related works. In the next part, the implementation of the proposed image processing algorithm and least square circle fitting method explained in detail. The last part will present the experimental setup, results of vision-based approach's experiments on different scenarios and discussions of the proposed approach's performance.

3.2 Earth-horizon based attitude determination method

In this research, we propose Earth-horizon based attitude determination method that provides accurate roll and pitch angles estimation from Earth horizon curvature using image processing algorithm. Using the advantages of Earth horizon curvature, the roll and pitch angles are estimated by horizontal and vertical movement of Earth center in relation to the centre of imagery sensor. Moreover, we focused on pitch and roll estimation based on Earth horizon curvature and aim at developing robust and accurate vision-based attitude estimation algorithm.

Research on Earth horizon based attitude determination system using CMOS camera is not a new idea [8][9]. Using the advantage of Earth horizon curvature in imager's field of view to estimate spacecraft's nadir vector parameter has been one main focus. Other related research is using CMOS camera as Star tracker sensor to estimate spacecraft's relative motion in 3 degrees of freedom [23]. In [13] the authors propose an image-based method for remote sensing satellite's attitude determination and control system in order to derive attitude knowledge from tracked features in imager's field of view.

In Earth horizon curvature based methods, when the horizon is visible in imager's field of view, it can provide an absolute attitude knowledge from captured images [5]. Main advantage of using CMOS camera as motion sensor is efficient, fuse with other sensors to refine the attitude accuracy and relatively inexpensive approach in terms of achieve more accurate attitude determination system for small satellites. Our approach in this research is also based on Earth horizon curvature detection using image processing algorithm to estimate satellite's critical roll, pitch and nadir parameters.

3.3 Attitude from Earth Horizon Curvature

This section presents a geometric relationship between orientation of vision sensor and Earth horizon curvature as viewed from satellite. Attitude of the spacecraft is the rotation from Earth Centered Inertial frame to the satellite body-fixed coordinate frame. In this work, we assume that vision sensor is rigidly attached to the spacecraft structure and z-axis of satellite body-fixed coordinate frame is defined to be the optical axes of the vision sensor and lies in same plane as the z-axis of camera frame. *Figure 3.1* shows a certain area of the earth is in the line of sight of the satellite. Moreover, the relationship between geometry as viewed from space and horizon curvature in image plane shown in *Figure 3.2*.

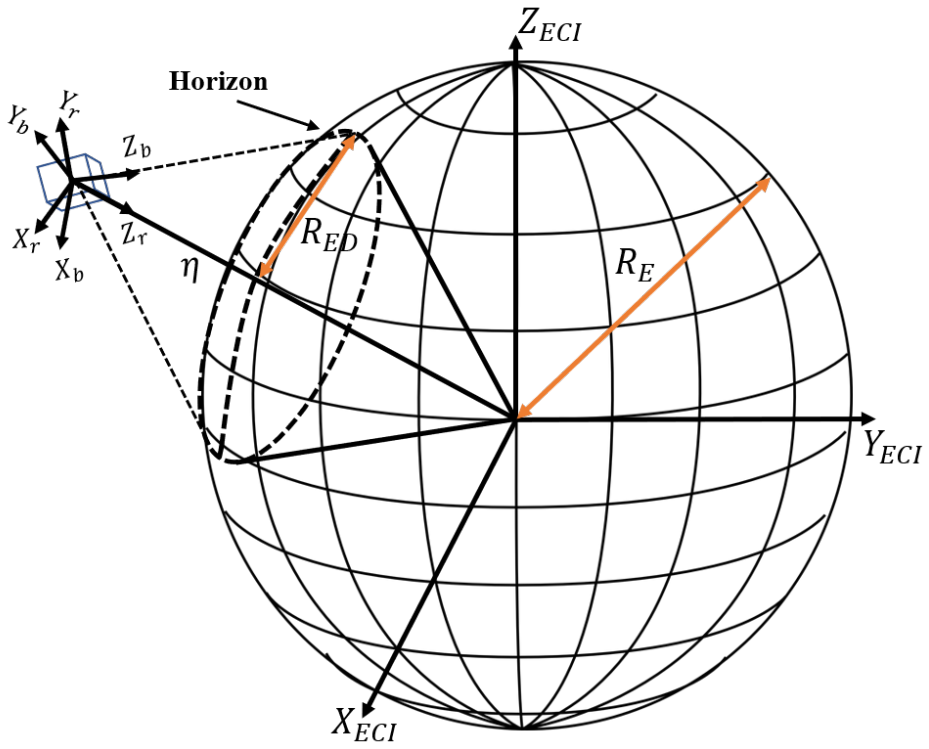

FIGURE 3.1: Definition of coordinate systems.

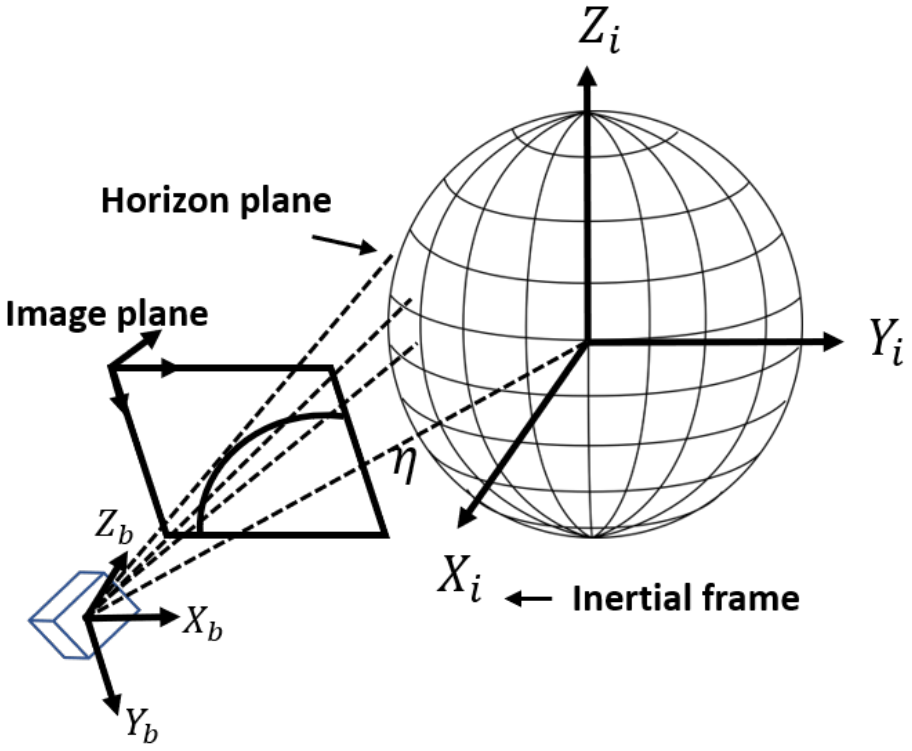

FIGURE 3.2: Illustration of the relationship between image plane and satellite attitude.

Earth's portion viewed from space in imager's field of view depends on vision sensor's parameters and altitude of spacecraft. Most small satellites launched in LEO, often used small and low-cost CMOS camera for its defined mission. These vision sensors have fixed lenses, focal length and field of view.

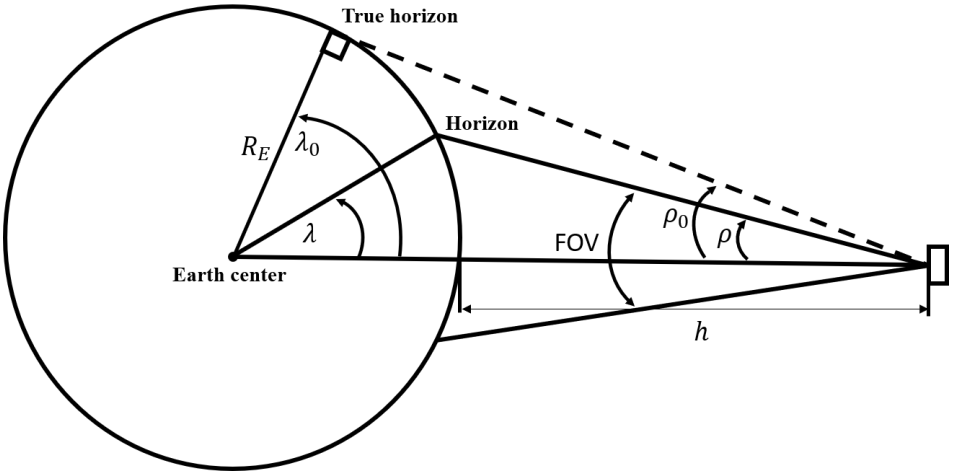

FIGURE 3.3: .

] Portion of the Earth viewed and seen by spacecraft [**4**]

In LEO, an Earth-pointing attitude of the camera system would lead to a FOV completely covered by the camera. It is important to note that the higher altitude, the most of Earth's portion appears in the imager's field view and most of its radius. In order to design accurate Earth-horizon detection algorithm, knowledge of Earth's portion appears in FOV is necessary. For this reason, we carried out the simulation of camera with fixed FOV parameters and at different altitudes. Following table represents a parameters camera that used in simulation to calculate the relationship between altitude, FOV and focal length.

Parameters	**Value**
Focal length	4.63mm
Resolution (LxH)	640x480 (pixels)
Sensor size (LxH)	3.984x2.952 (mm)
Earth radius	6371 km

TABLE 3.1: Parameters of simulation.

According to simulation of camera with fixed FOV illustrated in *Figure 3.4* shows a plot of the ratio of candidate image plane area in imager's field of view and area of full-sized Earth in image plane as function of satellite altitude.

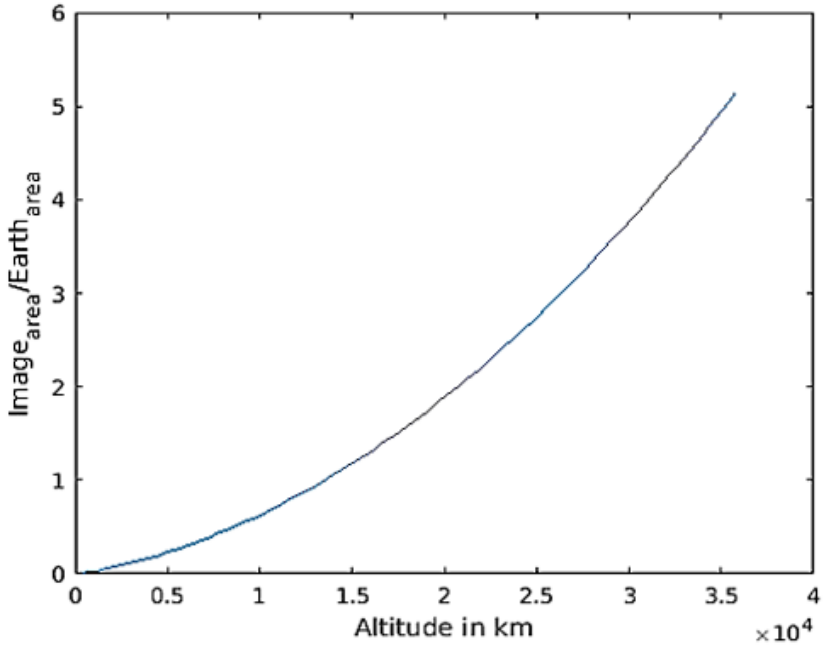

FIGURE 3.4: Ratio of candidate image plane area in imager's field of view and area of full-sized Earth in image plane as function of satellite altitude.

Moreover, *Figure 3.5* shows a plot of the ratio of radius of Earth horizon disk in imager's field of view and actual Earth radius as a function of altitude in range of interest according to simulation of camera with fixed FOV.

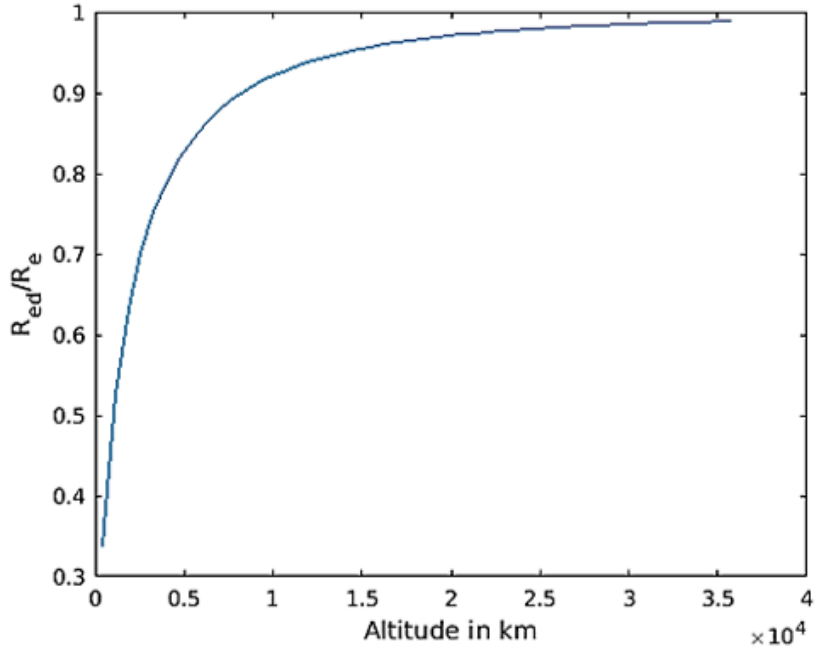

FIGURE 3.5: Ratio of radius of Earth horizon in imager's field of view and actual radius of Earth as function of satellite altitude.

3.4 Earth horizon detection algorithm

When looking at a picture like the one in *Figure 3.6* it is easy for the human mind to identify the earth's horizon, the empty space and even landmarks. We can tell where the center of the earth must be at rst glance. That is because our brain can recognize objects and is able to compare them with familiar objects from the memory.

FIGURE 3.6: Apollo 17 Hasselblad image 148/NN - Earth, LM Inspection.

However, to make it possible for computers to acquire the earth's horizon and find the center of the earth needs an image processing algorithms. The usefulness of image processing algorithms is apparent in many different fields covering medicine through remote sensing.

In order accurately measure the orientation angles of satellite based on earth-horizon image, first the algorithm needs to detect the earth's horizon then calculate center of the earth in image plane. Our approach attempts to solve this problem illustrated in following *Figure 3.7*.

The first step of the algorithm is the reads images from vision sensor and apply low pass filter in order to minimize noise in measurements. Morphological smoothing filter and thresholding is then performed on image. Edge estimation algorithm scans the entire image to detect the position of Earth horizon curvature edge. Once contour search algorithm performed, the Least-square circle fitting algorithm is used to estimate candidate radius and position of Earth center in image plane. The relationship between image plane and Earth horizon parameters from an isometric view shown in *Figure 3.8*.

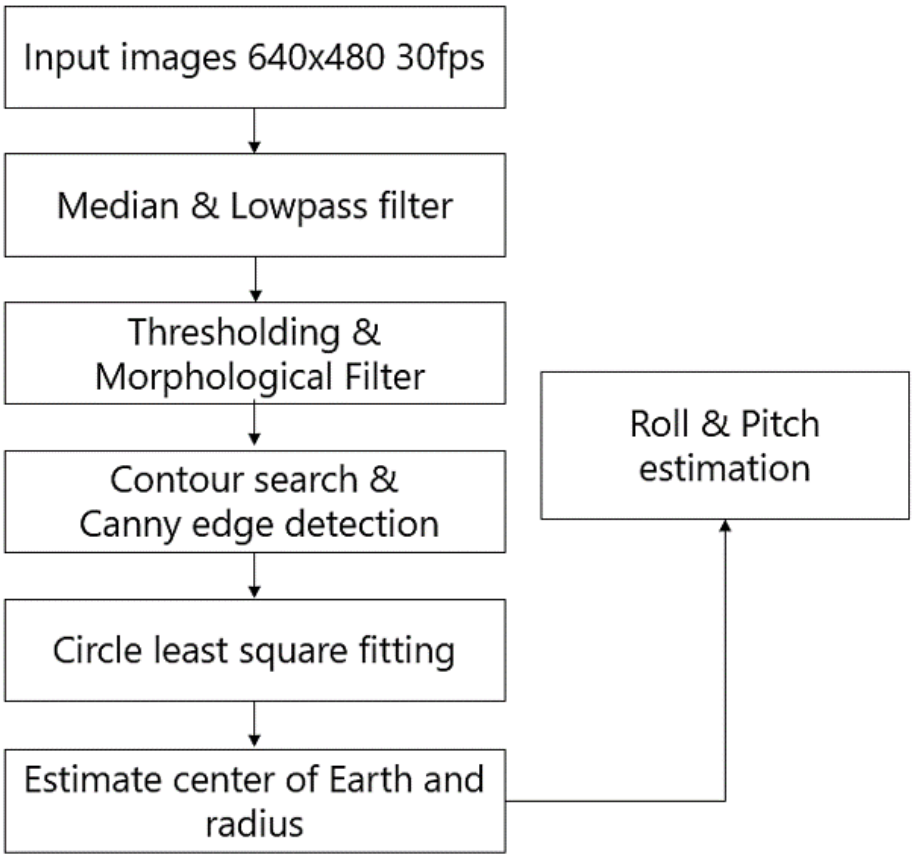

FIGURE 3.7: Flowchart of the proposed image processing algorithm for the Earth horizon detection.

The open source cross-platform library OpenCV [30] is used in our image processing approach which has a lot of dierent lters and functions built-in. OpenCV was built to provide a common infrastructure for computer vision applications and to accelerate the use of machine perception in the commercial products. The library has more than 2500 optimized algorithms, which includes a comprehensive set of both classic and state-of-the-art computer vision and machine learning algorithms.

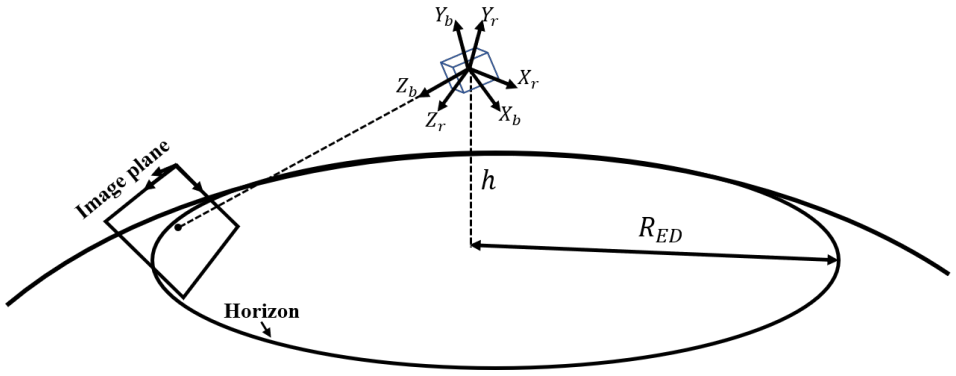

FIGURE 3.8: Isometric view of the image intersecting the Earth disk.

3.5 Least square circle fitting method

Our approach used a Least Square Method to calculate the center of Earth from detected horizon curvature in image plane. It takes the horizon line H, which must contain at least γ points, as input and calculates the best tting circle to these data points. Not only the center is calculated but also the radius of the earth in the image plane. This allows to check if the calculation returned a valid result by comparing the radius with the expected radius given by the height above ground.

The Least Square method minimizes the error $e(\lambda_{1,2}, \lambda_3, ...) = f_d(\lambda_{1,2}, \lambda_3, ...)$ of a function f to its desired value f_d by finding the optimal parameters λ_i.

$$\lambda_1^2 = (x - \lambda_2)^2 + (y - \lambda_3)^2 \tag{3.1}$$

where $p = (x, y) \in H$ is a data point, λ_1 is the radius and (λ_2, λ_3) are the center of the circle. The error e is then:

$$e(\lambda_1, \lambda_2, \lambda_3) = (x - \lambda_2)^2 + (y - \lambda_3)^2 - \lambda_1^2 \tag{3.2}$$

The non-linear *Equation 3.1* can be linearized by the substitutions

$$A := 2\lambda_2 \tag{3.3}$$

$$B := 2\lambda_3 \tag{3.4}$$

$$C := \lambda_1^2 - \lambda_2^2 - \lambda_3^2 \tag{3.5}$$

$$Ax + By + C = x^2 + y^2 \tag{3.6}$$

To minimize the error of the complete data set the sum of every error square

$$E(\lambda_1, \lambda_2, \lambda_3) = \sum_{i=1}^{|H|} e_i^2(\lambda_1, \lambda_2, \lambda_3) \tag{3.7}$$

$$E(\lambda_1, \lambda_2, \lambda_3) = \sum_{i=1}^{|H|} [(x_i - \lambda_2)^2 + (y_i - \lambda_3)^2 - \lambda_1^2]^2 \tag{3.8}$$

$$E(\lambda_1, \lambda_2, \lambda_3) = \sum_{i=1}^{|H|} [Ax_i + By_i + C - x_i^2 - y_i^2]^2 \tag{3.9}$$

must be minimized. This is done by solving the system

$$\begin{pmatrix} \frac{\delta E}{\delta \lambda_1} & \frac{\delta E}{\delta \lambda_2} & \frac{\delta E}{\delta \lambda_3} \end{pmatrix} = (0 \quad 0 \quad 0) \tag{3.10}$$

All following sums in this section without indicated limits are $\sum_{i=1}^{|H|}$. The solution *Equation 3.10* is the following system:

$$\begin{pmatrix} \sum x_i^2 & \sum x_i y_i & \sum x_i \\ \sum x_i y_i & \sum y_i^2 & \sum y_i \\ \sum x_i & \sum y_i & |H| \end{pmatrix} \begin{pmatrix} A \\ B \\ C \end{pmatrix} = \begin{pmatrix} \sum x_i(x_i^2 + y_i^2) \\ \sum y_i(x_i^2 + y_i^2) \\ x_i^2 + y_i^2 \end{pmatrix} \tag{3.11}$$

The substitutions *Equation 3.12* and *Equation 3.13* are done to simplify the view:

$$\begin{pmatrix} K & L & M \\ L & P & O \\ M & O & N \end{pmatrix} := \begin{pmatrix} \sum x_i^2 & \sum x_i y_i & \sum x_i \\ \sum x_i y_i & \sum y_i^2 & \sum y_i \\ \sum x_i & \sum y_i & |H| \end{pmatrix} \tag{3.12}$$

$$\begin{pmatrix} Q \\ R \\ S \end{pmatrix} := \begin{pmatrix} \sum x_i(x_i^2 + y_i^2) \\ \sum y_i(x_i^2 + y_i^2) \\ x_i^2 + y_i^2 \end{pmatrix} \tag{3.13}$$

The equation *Equation 3.11* can be solved for A, B and C as follows:

$$A = \frac{O^2Q - NPQ + LNR - MOR - LOS + MPS}{L^2N - 2LMO + KO^2 + M^2P - KNP} \tag{3.14}$$

$$B = \frac{LNQ - MOQ + M^2R - KNR - LMS + KOS}{L^2N - 2LMO + KO^2 + M^2P - KNP} \tag{3.15}$$

$$C = \frac{MPQ - LOQ - LMR + KOR + L^2S - KPS}{L^2N - 2LMO + KO^2 + M^2P - KNP} \tag{3.16}$$

The desired values reveal then as:

$$(radius) \quad \lambda_1 = \frac{\sqrt{4C + A^2 + B^2}}{2} \tag{3.17}$$

$$(center_x - coordinate) \quad \lambda_2 = \frac{A}{2} \tag{3.18}$$

$$(center_y - coordinate) \quad \lambda_3 = \frac{B}{2} \tag{3.19}$$

3.6 Circle fitting algorithm test

In order to validate the performance of the proposed approach first we tested the algorithm on simple Earth shape model image as shown in following image. A set of experiments were undertaken using different parameters each test images.

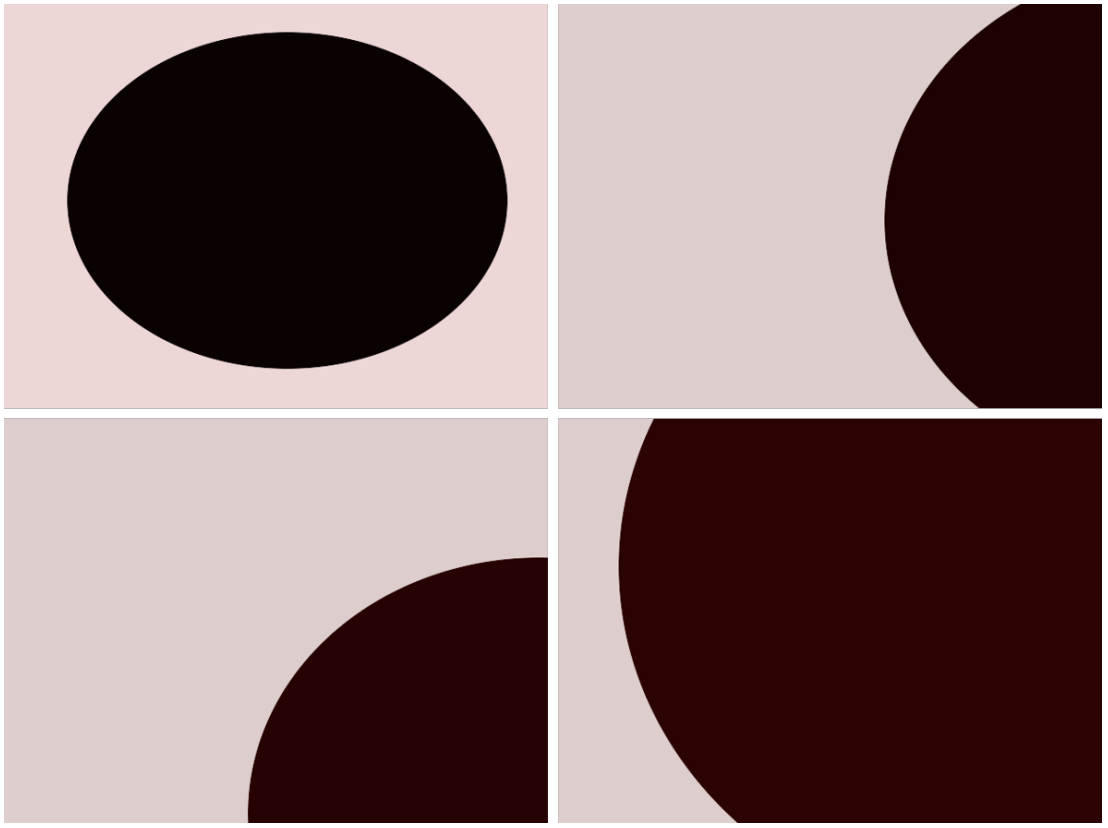

FIGURE 3.9: Simple Earth shape model - generated images.

Regarding very simple Earth shape model images, the proposed image processing algorithm performed well on finding the horizon of the shape model. After detection of horizon line from the test images, we applied least square circle fitting algorithm on acquired horizon line points. Following *Figure 3.10*, *Figure 3.11* and *Figure 3.12* show the results of the least square circle fitting algorithm. A center of the shape model is presented as blue cross symbol and horizon line is presented as red line.

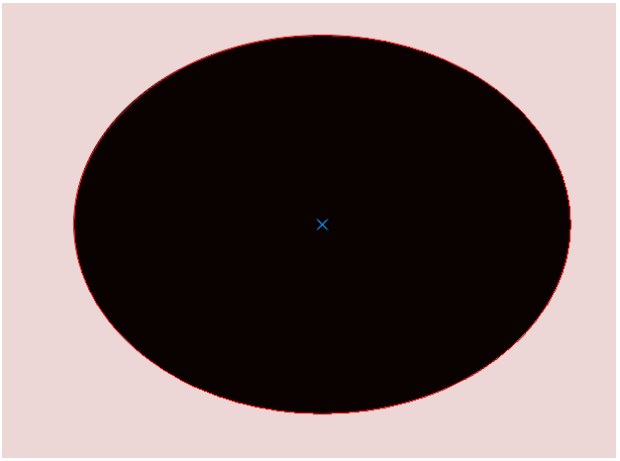

FIGURE 3.10: Resulting image of horizon line and center of shape model detected.

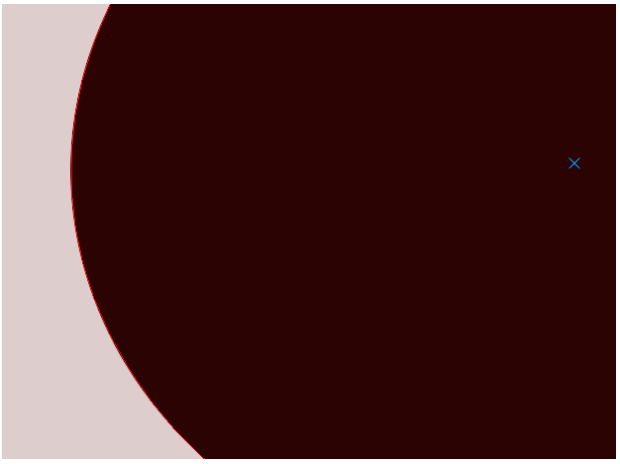

FIGURE 3.11: Resulting image of horizon line and center of shape model detected.

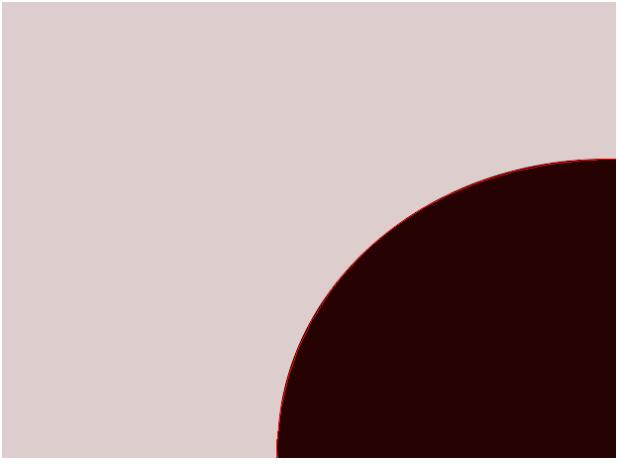

FIGURE 3.12: Resulting image of horizon line of shape model detected.

Calculating Roll and Pitch angles

The Roll and Pitch angles are calculated from the center coordinate of the horizon circle and principal point of image plane. The mathematical relationships of Pitch angle and horizon curvature in image plane are shown in following images.

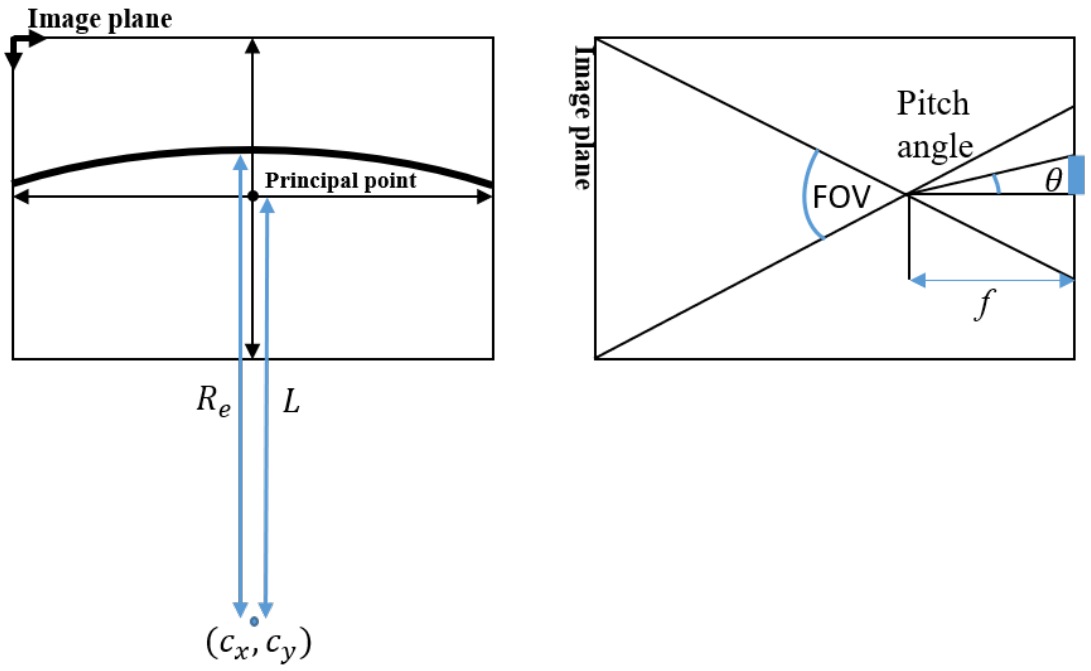

FIGURE 3.13: The illustration of mathematical relationships of Pitch angle, horizon curvature and principal point.

After calculation of the radius of horizon curvature and coordinates of the center in image plane using least square circle fitting algorithm, the pitch angle can be estimated as follows:

$$\theta = \tan\left(\frac{L - R_e}{f}\right) \tag{3.20}$$

In this equation:

f - Focus length

R_e - Computed radius of Earth horizon

L - Length from center point to principal point

Moreover, the Roll is the angle between the image plane's Y axis and the vector from the center of the image plane to center of Earth. The mathematical relationships of Roll angle is shown in following image.

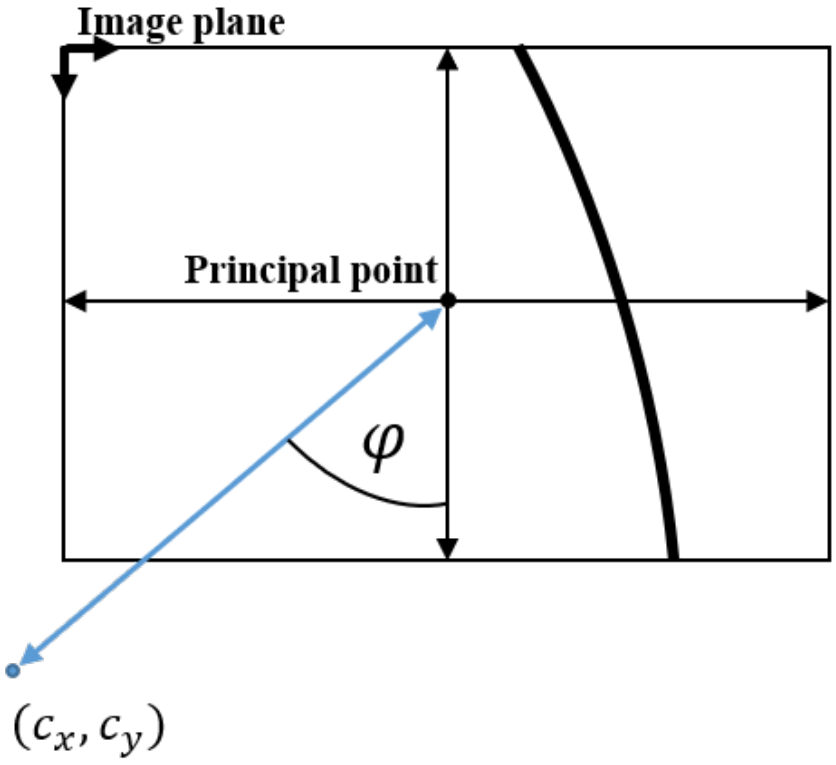

FIGURE 3.14: The illustration of mathematical relationships of Roll angle, horizon curvature and principal point.

From these computed values of the radius of horizon curvature and coordinates of the center in image plane, the algorithm estimates the roll angle as follows:

$$\varphi = \tan^{-1}(\frac{C_x}{C_y}) \tag{3.21}$$

In this equation:

C_x - x-coordinate of center of horizon circle

C_y - y-coordinate of center of horizon circle

3.7 Experimental Setup

We decided to use a Raspberry Pi 3 model B which features a Broadcom BCM2837 ARM Cortex-A53 quad core CPU running at 1200 MHz and 1 Gb of RAM. Furthermore, an inexpensive 5 mega pixel Omnivision 5647 camera module (version 2) is used which can record up to 90 FPS at 640×480 pixels. Furthermore in order to compare performance of vision-based method with inertial sensor, we used MPU6050 inertial sensor which consists of a 3-axis Accelerometer and 3-axis Gyroscope. *Figure 4.19.* shows a picture of the assembled hardware.

FIGURE 3.15: Assembled hardware of prototype of Vision-based attitude sensor.

Laboratory experiment test environment and experimental setup for a vision-based sensor approach are shown in following images. The main purpose of the laboratory experiment is the functional test of the system and image processing algorithms developed in the scope of this thesis. In order to generate a realistic simulated Earth horizon, we used real satellite captured images data and computer generated images. By capturing imagery data from the front scene, we estimated the attitude of the prototype setup by the proposed approach.

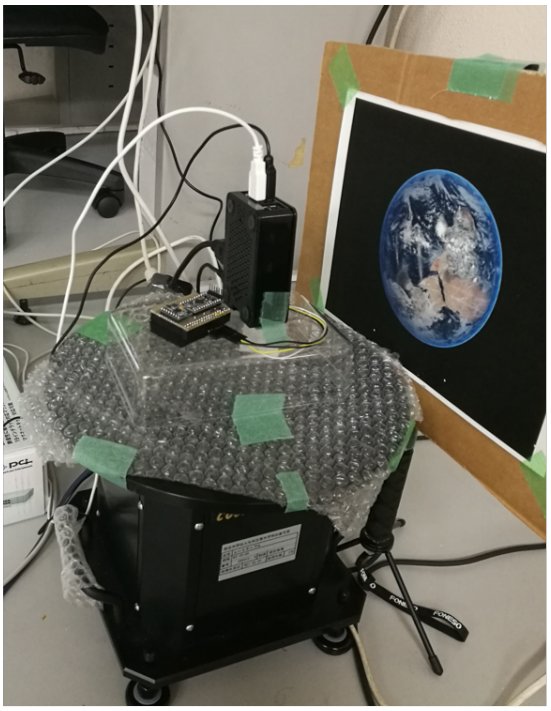

FIGURE 3.16: Laboratory setup as assembled and used for functional tests - Pitch angle estimation setup.

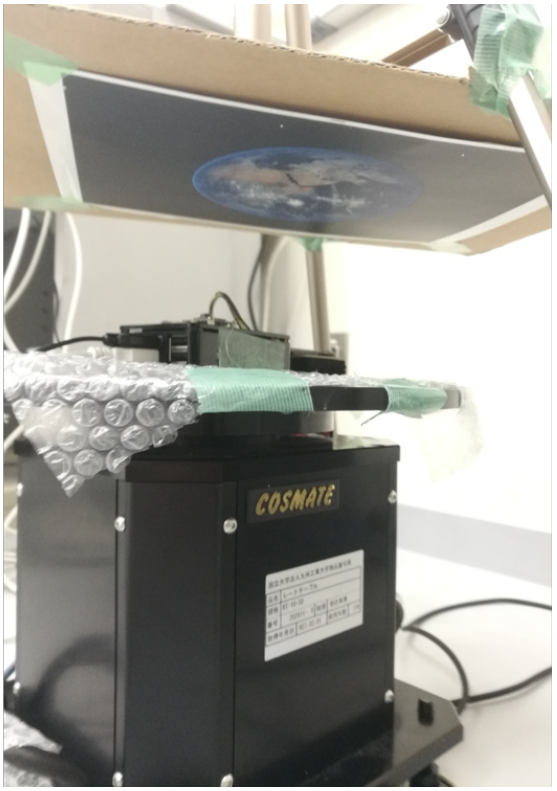

FIGURE 3.17: Laboratory setup as assembled and used for functional tests - Roll angle estimation setup.

3.8 Experimental Results and Performance Evaluation

The purpose of the experimental part is to test the performance of the proposed Earth-horizon based attitude determination sensor that combination with the developed algorithms concerning the image processing. In order to verify the robustness of proposed approach, we applied our algorithm to satellite captured images with actual roll and pitch changes. Furthermore, because of lacking the attitude data information of the corresponding satellite captured images data, we made the experiment by using realistic computer generated earth horizon curvature images and a high-precision one axis rate table. An image as taken by the Raspberry Pi single board computer's camera module is shown in first image of *Figure 3.18*. Here the each steps of proposed image processing algorithm's output images are presented in order to visualize the approach.

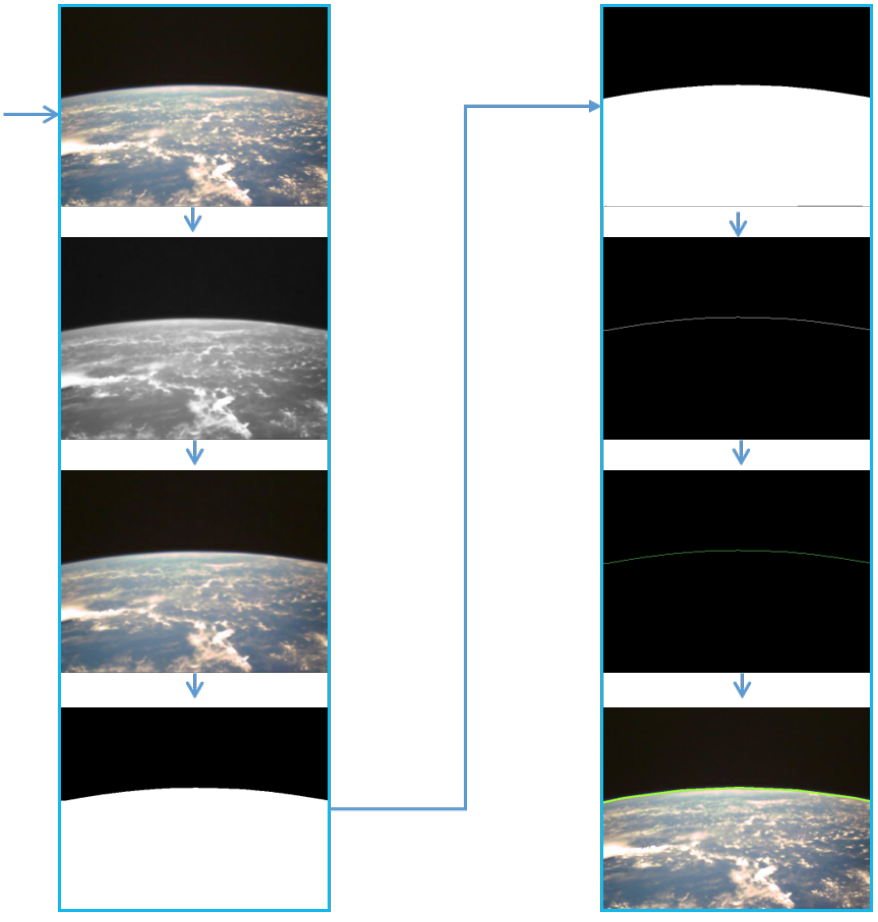

FIGURE 3.18: Image processing steps of the horizon curvature detection algorithm.

The results as obtained by the proposed approach using actual satellite (Horyu-4, KIT) captured images [31], can be seen in following *Figure 3.19* and *Figure 3.20*.

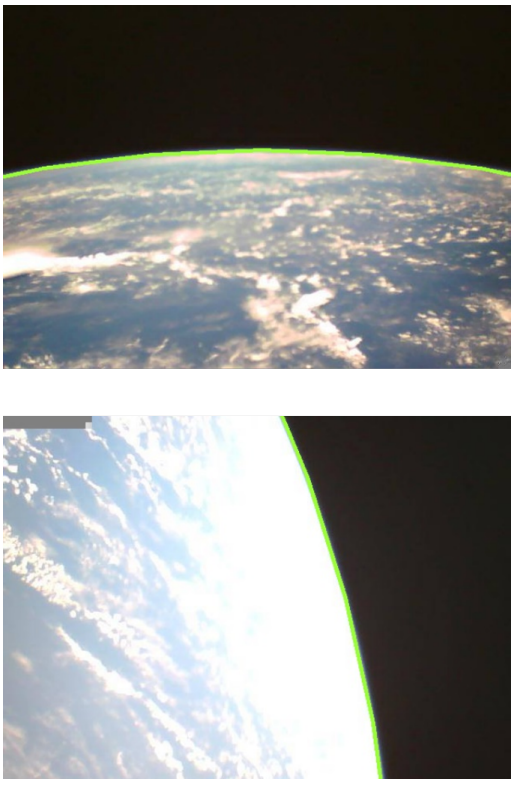

FIGURE 3.19: Horizon curvature detected by the proposed image processing algorithm.

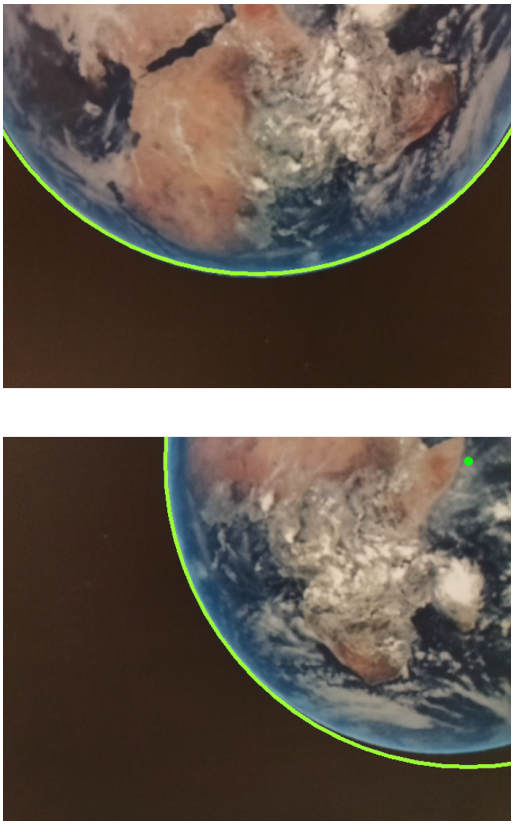

FIGURE 3.20: Horizon curvature detected by the proposed image processing algorithm.

The following results as obtained by the proposed approach using realistic computer generated earth horizon curvature images and a high-precision one axis rate table, can be seen in following figures.

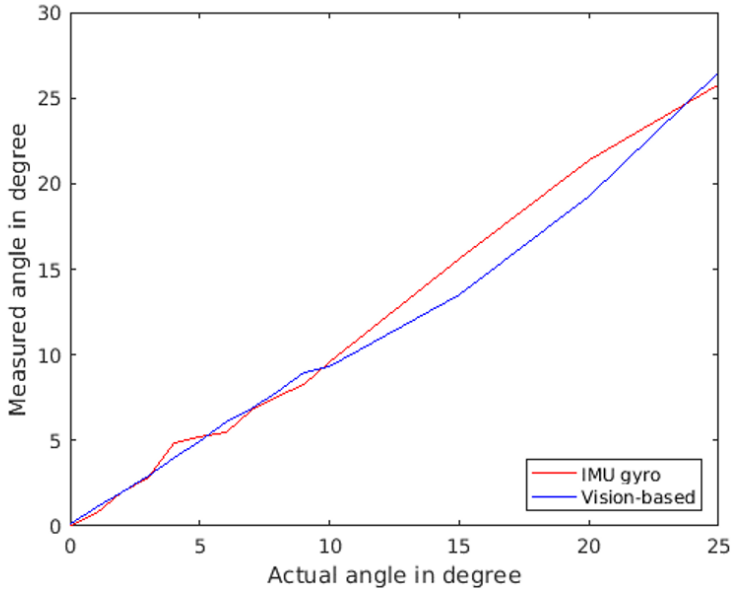

FIGURE 3.21: Earth-horizon based approach and MEMS gyro measurement comparison for the Pitch measurements.

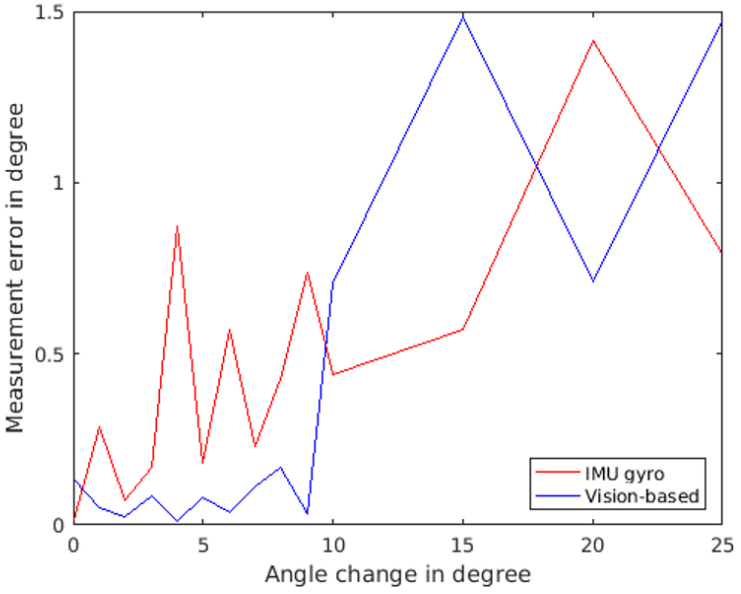

FIGURE 3.22: The measurement error comparison of Earth-horizon based approach and MEMS gyro for the Pitch measurements.

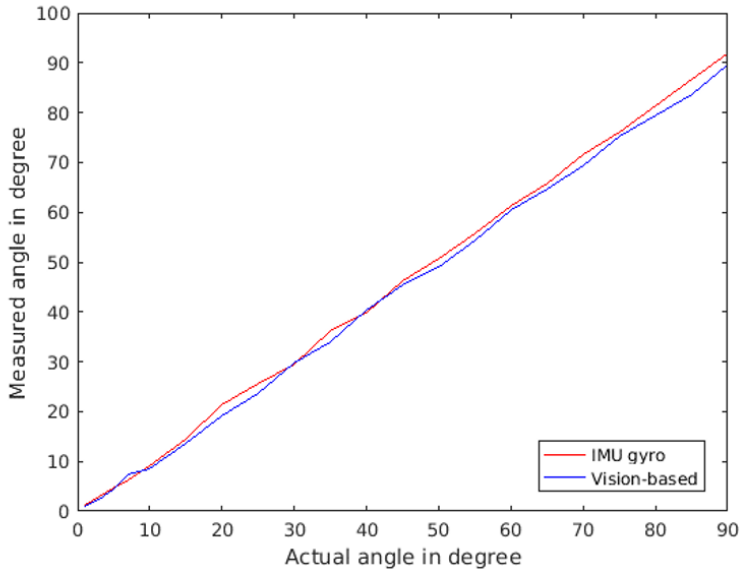

FIGURE 3.23: Earth-horizon based approach and MEMS gyro measurement comparison for the Roll measurements.

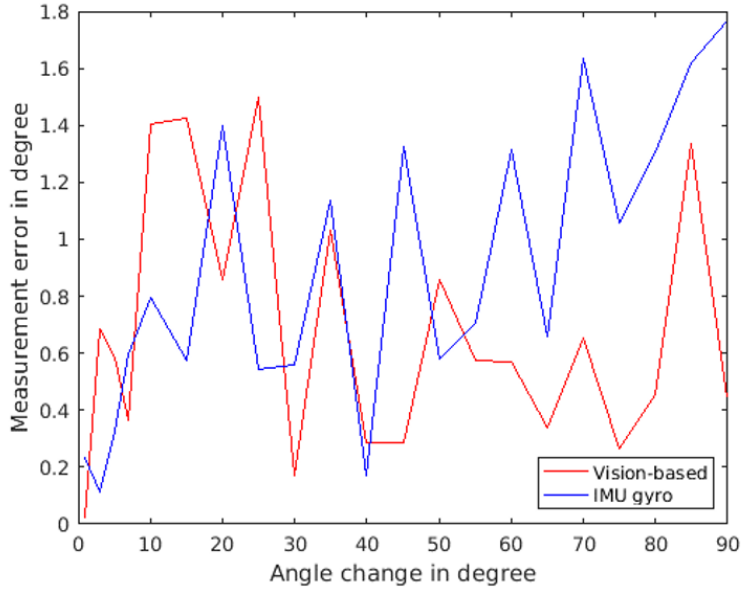

FIGURE 3.24: The measurement error comparison of Earth-horizon based approach and MEMS gyro for the Roll measurements.

The pitch angle accuracy measurement was tested first. The pitch angle was measured at 5.0° degrees interval over the full range of 0.0° to 25.0°. The results are shown in the graphs in *Figure 3.21* and *Figure 3.22*. In the measurement error graph it can be seen that the accuracy deteriorates towards big change of the pitch angle. Lens distortion

which was not well calibrated for and environmental conditions could be the reasons for this deterioration.

The roll angle accuracy measurement was tested in a similar way as the pitch angle with interval of 5.0°. It was tested over the full range of 0.0° to 90.0° and shown in *Figure 3.23* and *Figure 3.24*. In the measurement error graph it can be seen that a decrease in accuracy occurred from 10.0° to 25.0° and at 85.0°.

In both pitch and roll angle measurement result graphs, it is apparent that the vision-based approach showed slightly better accuracy compare with MEMS gyro sensor. In order to quantify the experimental results, the average and maximum error of each measurement was calculated and these are listed in following *Table 3.2*.

Parameters	**Average error**	**Maximum error**
Pitch	0.37 degrees	1.48 degrees
Roll	0.67 degrees	1.49 degrees

TABLE 3.2: Measurement errors of test result graphs.

Regarding processing time of the proposed image processing algorithm, the Raspberry Pi single board computer was not be able to run fast enough to provide attitude measurement in real-time. The following *Table 3.3* shows the average process time comparison of the proposed image processing algorithm and single board computer camera capturing speed without image processing.

Parameters	**Processed approach**	**Without image processing**
Time (ms)	71	31
Camera speed (FPS)	14	32

TABLE 3.3: Average process time comparison between the proposed image processing algorithm and without image processing.

Moreover, the power consumption of the proposed vision-based attitude system is measured and presented in following *Table 3.4*. The Raspberry Pi 3 Model B single board computer has a less power efficiency, because of the Gigabit-Ethernet chip, the Wi-fi module and other additional integrated chips.

Parameters	**Current (A)**	**Power (W)**
Idle mode	0.484	2.42
During processing of algorithm	0.862	4.31

TABLE 3.4: Average power consumption comparison between the during processing algorithm and idle mode.

Chapter 4

Visual-Inertial Attitude Propagation Approach

4.1 Overview

In this chapter, we discuss Visual-Inertial attitude propagation approach that provides nominal attitude in 3 degrees of freedom (3DOF) based on homography of two sequentially captured images of a planar scene. In a first step, we focus in particular on the methodology of our approach, including the geometrical image relationships with satellite attitude, the image processing techniques used in the vision-based method, and the implementation of the sensor fusion framework. In the next step, the proposed approach is applied to real Earth-observation raw imagery data and simulated realistic imagery data. Finally, discussions of simulation and experiment results are presented.

4.2 Visual-Inertial methodology

The integration between visual and inertial sensors is motivated by what happens with the vestibular and vision system in humans and animals [16], and the basic principle for integrating vision and inertial sensors together is their complementary properties. Inertial sensors offer good signals with higher update rates during fast motions but are sensitive to accumulated drift due to the integration during the estimation of attitude. In contrast, visual sensors provide precise ego-motion estimation with low rate in long term, but suffer from blurred features under fast and unpredicted motions. The aim of visual-inertial sensor integration is to overcome some fundamental limitations of vision-only tracking and inertial measurement unit (IMU) only tracking using their complementary properties.

In this thesis the problem of attitude estimation of small satellites is approached using the combination of a vision and an inertial sensors. Many methods were proposed for satellite attitude estimation based on vision sensors, such as CMOS Earth horizon sensors, Stellar gyroscopes and Image-based attitude estimation and control methods. CMOS Earth horizon sensor tracks Earth's horizon curvature in the imager's field of view (FOV) and provides roll and pitch angle measurements [8][9]. The image-based attitude estimation and control methods usually are based on Earth's surface feature tracking and feature-correspondences matching techniques with different outlier rejection methods and provide nominal attitude in 3 degrees of freedom (3DOF) [13][15]. The Stellar gyroscope approach tracks the motion of stars in the imager's FOV and provides the relative attitude (3DOF) information [14]. In unmanned aerial vehicle (UAV) navigation studies, sensor fusion of visual and inertial sensors has been widely investigated [17][18].

In this chapter, we introduce and implement a visual-inertial attitude propagation approach for small satellites which employs a 2D image sensor as an attitude sensor and a triad MEMS rate gyro sensor. This approach used triad MEMS rate gyros to obtain useful information with high update rates during fast rotational motions and a vision sensor was employed to provide accurate relative attitude estimation with low update rates.

The vision-based attitude estimation approach is based on the principle that two sequentially captured images of a planar scene are related by a homography [22]. The planar scene corresponds to the Earth surface, which is assumed to be relatively at, and observed by the nadir- pointing camera on the satellite. Between sequentially captured images, the motion of the Earth surface features in camera's FOV contains information about the camera movement. Based on this constraint, the relative attitude (3DOF) information between the images can be calculated from the homography which is induced by

sequentially captured images of the Earth surface. In order to estimate the homography, a set of corresponding feature points must be obtained from two sequentially captured images. First set of feature points extracted from the first captured image and tracked on the second image. Then, the image coordinates of each feature in both images used to calculate the homography. But, between two sequentially captured images the camera center shifts due to the satellite translational motion. This process causes a parallax shift [12] that the image coordinates of tracked feature points shifts relative to satellite motion.

Also, due to the Earth's rotational motion the image coordinates of tracked feature points shifts [32]. After compensation of these shifts from the image coordinates of tracked feature points, the estimated homography used to calculate a relative attitude information. Based on the homography decomposition algorithm [33] a relative attitude information with respect to the spacecraft's initial orientation derived and integrated with triad rate gyro's measurements in the unscented Kalman Filter framework.

In our study, the main purpose of the integration of visual and inertial sensors is to improve the accuracy of attitude estimation capabilities by using a vision-based approach to compensate the rate gyro's continually increasing drifts within an unscented Kalman filter (UKF) framework. *Figure 4.1* shows a framework of the proposed approach for small satellite attitude determination.

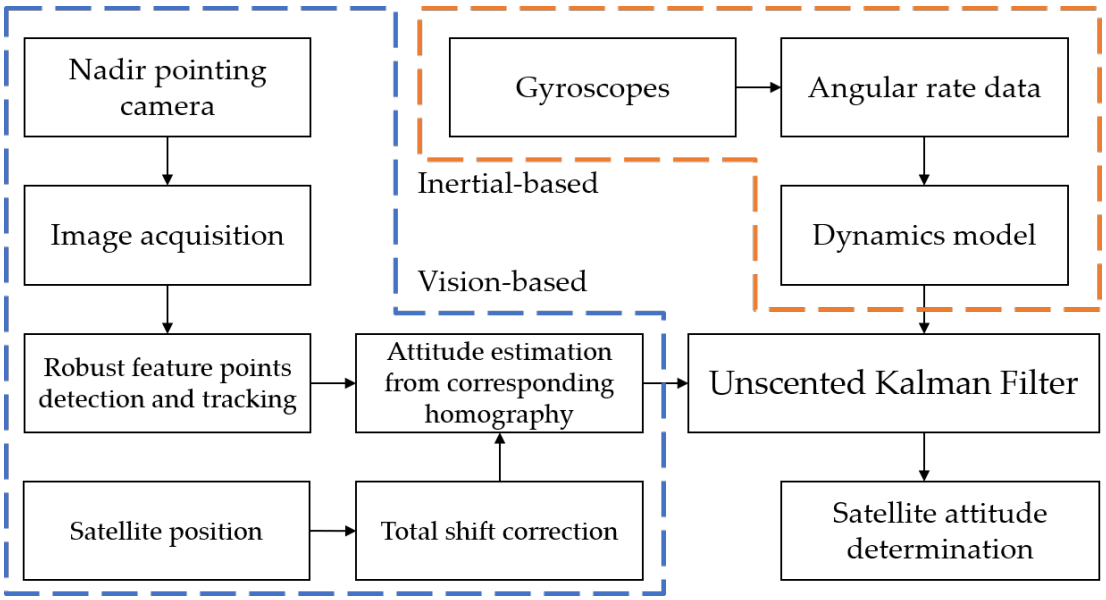

FIGURE 4.1: Framework of the proposed approach for attitude propagation.

4.3 Vision-Based Method

Conceptually, the attitude propagation of the visual-inertial approach consists of three main parts. The first part obtains a nominal attitude (3DOF) estimation from the vision-based method. The second part directly obtains angular velocity from the triad MEMS rate gyro sensor and provides it into the sensor fusion framework. The third part integrates the vision-based and inertial-based methods within the sensor fusion framework and propagates the satellite attitude in 3 degrees of freedom. *Figure 4.2* shows a block diagram of the proposed vision-based approach for estimation of attitude information with camera sensor.

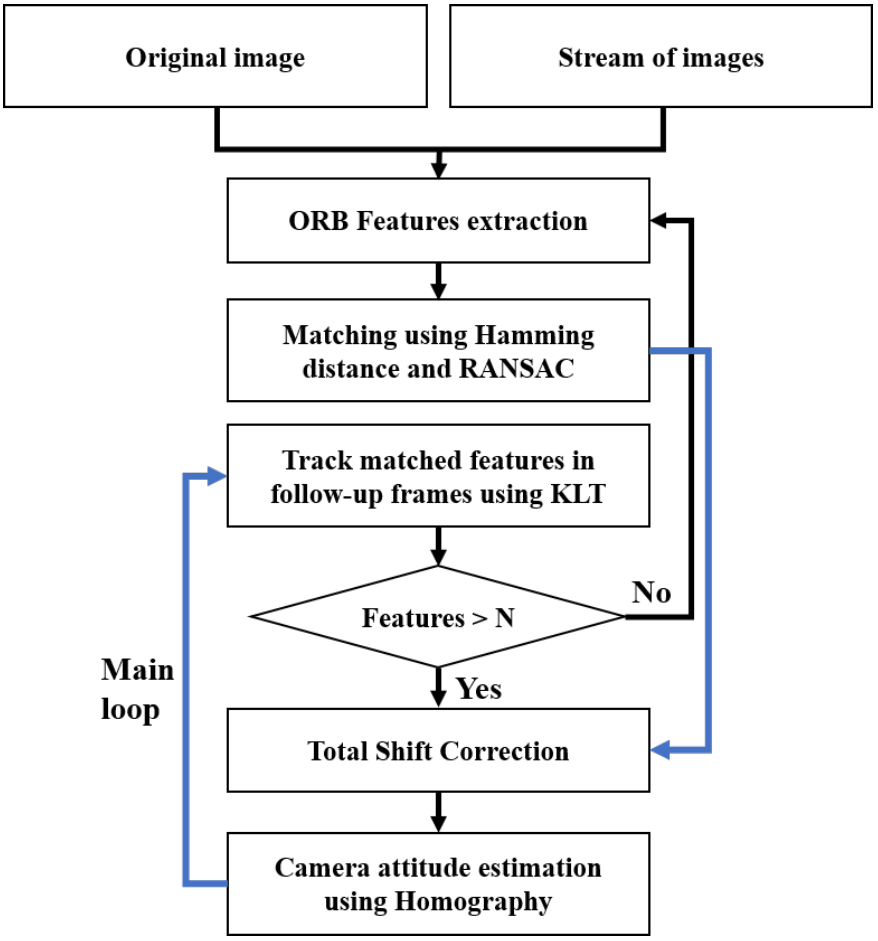

FIGURE 4.2: The block diagram of the proposed vision-based method.

The proposed vision-based approach employed an Oriented FAST and Rotated BRIEF (ORB) features detection algorithm [34] due to its computational efficiency compared to other local feature descriptors such as SIFT (Scale-Invariant Feature Transform) [35][36]. First, a set of feature points are extracted from the first captured image using ORB descriptor. Then, the KLT (Kanade–Lucas–Tomasi) feature tracker [37] is used to track

the extracted set of feature points of the first image on the second captured image to obtain the image coordinates of tracked feature points. After that, the total shift correction method is applied to compensate the displacement of feature points on image plane which is occurred due to the satellite's translational and Earth's rotational motions. Then, a corresponding homography is computed from a set of feature points using the Direct Linear Transform (DLT) algorithm [38] with outlier rejection random sample consensus (RANSAC) method [39] by removing mismatched feature pairs. Finally, the satellite's nominal attitude is derived by using a Singular Value Decomposition (SVD) algorithm from the estimated homography.

4.3.1 Perspective projection

We consider two sequentially camera frames that have overlapping regions as shown in *Figure 4.3*. By using homogeneous coordinates [22], the previous frame point x_i on the image plane and current frame point x_i' can be computed from the corresponding world point X_i which can be expressed as

$$x_i = \begin{bmatrix} u \\ v \\ 1 \end{bmatrix}, \quad x_i' = \begin{bmatrix} u' \\ v' \\ 1 \end{bmatrix}, \quad X_i = \begin{bmatrix} X \\ Y \\ Z \\ 1 \end{bmatrix}, \quad i = 1, 2, 3, ...n \tag{4.1}$$

$$x_i = sK \begin{bmatrix} R & 0 \\ t & 1 \end{bmatrix} X_i \tag{4.2}$$

where s is the scale factor, the matrix K is the camera calibration matrix, and R and t are the camera's extrinsic parameters. Using homogeneous camera projection, the matrix P world point X_i and image point x_i relation can be written succinctly in up to a scale as

$$x_i \approx PX_i \tag{4.3}$$

We assume that the images obtained are without the translational motion of the camera center and that the camera is rotated about its axis without a change in the internal parameters. It then follows that the image points of a world point X_i by the two frames are related as

$$x_i = PX_i = KR[I|-C]X_i \tag{4.4}$$

$$x_i' = P'X_i = KR'[I|-C]X_i \tag{4.5}$$

$$P' = (KR')(KR)^{-1}P \tag{4.6}$$

$$x_i' = (KR')(KR)^{-1}Px_i \tag{4.7}$$

where C is the position of the camera optical centre in the world reference frame. Corresponding image points in two frames related by a planar homography are expressed as

$$H = (KR')(KR)^{-1}P \tag{4.8}$$

$$x_i' = Hx_i \tag{4.9}$$

After that, total shift compensation and scale factor are taken into account in the above equations yields as

$$x_i' = \mu(KR')(KR)^{-1}P(x_i + (\Delta d_t + \Delta d_e)) \tag{4.10}$$

where μ is the scale factor and the total shift consists of the parallax shift [12] Δd_t between sequential images that occurred by the satellite's translational motion and land surface shift Δd_e due to Earth's rotational motion.

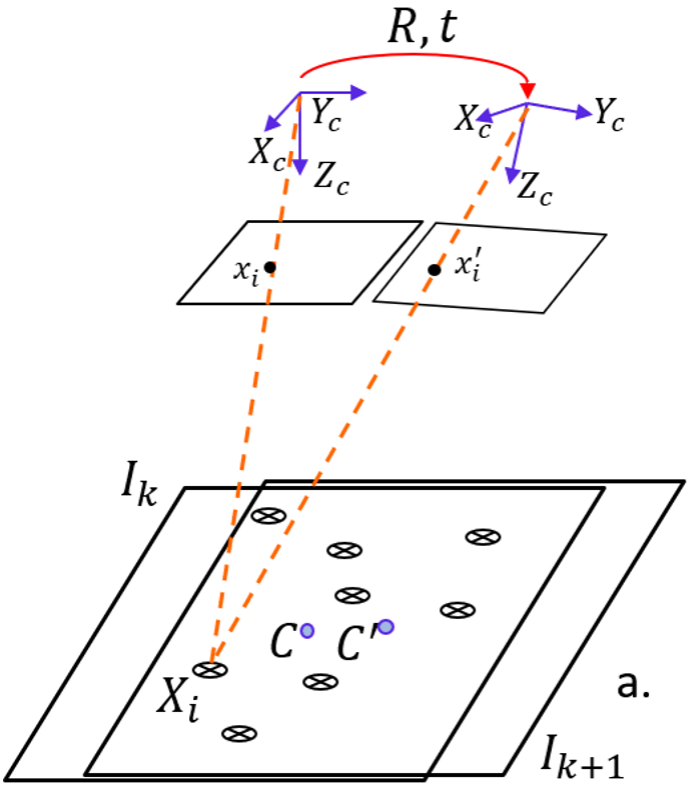

FIGURE 4.3: Previous and current camera frames with the relationship between world points and image points .

4.3.2 Total Shift Correction Method

The parallax shift Δd_t in captured sequential images depends on the satellite's ground speed represented by satellite's altitude of orbit and the camera's frame rate. We assumed that satellite position information was obtained from Global Positioning System (GPS) and that the camera's frame rate remained constant. If the direction of the flight is along the x axis of the image plane, then the camera's principal point will move along the x axis of image plane. *Figure 4.4* shows a schematic view of feature point shifts.

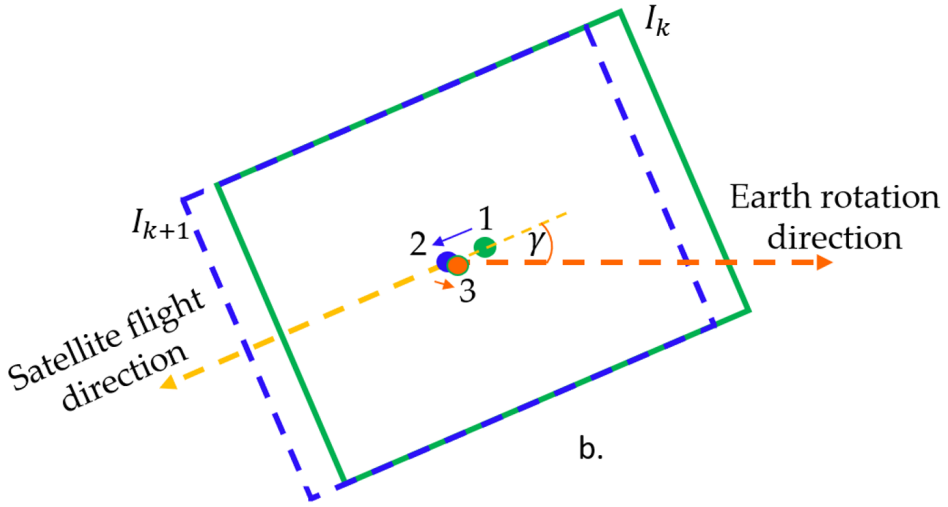

FIGURE 4.4: Feature points location shift due to satellite translation and Earth's rotation.

In this study, we approximated the parallax shift from the relation between the satellite orbit parameters and the nadir-pointing camera parameters. First, we calculated the satellite's ground velocity as

$$T = 2\pi(R_E + h)\sqrt{\frac{R_E + h}{Gm_E}} \tag{4.11}$$

$$v_g = \frac{2\pi R_E}{T} \tag{4.12}$$

where h is the altitude of the satellite, R_E is the radius of the Earth, m_E is the mass of the Earth, T is an orbital period, and G is the gravitational constant. Then, we calculated the resolution of the camera with respect to the Earth's surface as:

$$\tan\frac{\theta}{2} = \frac{Ny}{2f} = \frac{Z/2}{L} \tag{4.13}$$

where θ is the field of view (FOV) of satellite camera, f is the focal length of camera, N is the pixel number of the corresponding axis of the camera's sensor, y is the physical length of a single pixel of the image sensor, Z is the relative length of the Earth's surface with the corresponding image sensor's axis length, and L is the distance from the camera sensor to the Earth's surface. Then, the relative shift of feature points on the image plane can be computed from Equations (11), (12) and (13) as follows:

$$\Delta d_t = \begin{bmatrix} \upsilon_g(t_1 - t_0)/(Z/N) \\ 0 \\ 1 \end{bmatrix} \tag{4.14}$$

where $(t_1 - t_0)$ is the time interval between the current and previous captured images. The land surface shift δd_e occurs because of the Earth's rotational motion and depends on the latitude of the satellite camera's line-of-sight on Earth's surface due to Earth's circumference difference at different latitudes. Relative shift of feature points on the image plane can be computed based on satellite position, flight direction relative to Earth's rotation, the Earth's rotation rate, and satellite orientation angle, and can be represented as follows:

$$l = R_E \cos(\alpha) \frac{N}{Z} \Omega_E (t_1 - t_0) \tag{4.15}$$

$$\Delta d_e = \begin{bmatrix} l_x \cos(\gamma) - l_y \sin(\gamma) \\ l_x \sin(\gamma) + l_y \cos(\gamma) \\ 1 \end{bmatrix} \tag{4.16}$$

where l is the displacement of the Earth surface between the time interval $(t_1 - t_0)$, γ is the satellite orientation angle calculated from trigonometry in the local tangent plane at the point X_i [**18**], α is the latitude of the corresponding Earth's surface captured by the satellite camera, $\frac{N}{Z}$ is an image resolution per pixel of the corresponding axis of the image sensor, and Ω_E is the Earth's rotation rate.

4.3.3 Oriented FAST and Rotated BRIEF (ORB)

Robust feature extraction and matching play a crucial role in camera motion estimation based on feature correspondences. A number of feature detection algorithms have been developed in recent years which can be used for wide range of image processing applications. However, the computational complexity and accuracy of feature matches limits the applicability of these algorithms. For instance, SIFT (Scale-Invariant Feature Transform), SURF (Speeded-Up Robust Features), Oriented FAST and Rotated BRIEF (ORB) and FREAK (Fast Retina Key point) feature detection algorithms are mostly used in camera motion estimation approaches due to their robust for finding interesting points even under scale, illumination, small affine, and pose changes.

In our vision based approach, ORB feature detector is used due to its computational efficiency compared to other local feature descriptors. ORB is fast binary descriptor based on BRIEF and FAST which is rotation invariant and resistant to noise. This approach developed in 2011, it is specically built to be fast and computationally low-cost for real time applications. ORB detector works with a modied version of FAST, called oFAST, which retains only the best features within a multi-scale pyramid and adds the orientation component to them. Harris corner measure is rst used to order FAST keypoints. For a target set of N keypoints, rst a low threshold is used to get more than N points, then these are ordered according to their Harris measure and only the better N are retained. This process is repeated for each scale of a pyramid which is generated from the basic image in order to obtain multi-scale features. Corner orientation is then added by a simple measure exploiting the intensity centroid. Intensity centroid assumes that a corner's intensity is offset from its center. Dening the moment of a patch as

$$m_{pq} = \sum_{x,y} x^p \cdot y^p \cdot I(x, y) \tag{4.17}$$

The centroid may be found as

$$C = \left(\frac{m_{1,0}}{m_{0,0}}, \frac{m_{0,1}}{m_{0,0}} \right) \tag{4.18}$$

Constructing a vector from the corner center to the centroid, then the orientation can be simply compute as

$$\theta = \arctan(\frac{m_{0,1}}{m_{1,0}}) \tag{4.19}$$

To improve rotation invariance of this measure, moments are computed with x and y remaining within a circle of radius r equal to the patch size. ORB descriptor is obtained from a modication of BRIEF, called rBRIEF. First BRIEF descriptor is steered according to orientation of keypoints. For any set of n binary test at location x_i, y_i the following

matrix is dened as

$$S = \begin{bmatrix} x_1 & \cdots & x_n \\ y_1 & \cdots & y_n \end{bmatrix} \tag{4.20}$$

Using patch orientation θ and corresponding rotation matrix R_θ a steered version of S is computed as

$$S_\theta = R_\theta \cdot S \tag{4.21}$$

and the steered BRIEF operator becomes:

$$g_n(p, \theta) = f_n(p) | (x_i, y_i) \in S_\theta \tag{4.22}$$

angle is discretized to increment of $2\pi/30$ and a lock up table of precomputed BRIEF patterns is constructed. Once BRIEF is oriented along keypoint direction, it loses his property of having each bit feature with high variance and mean near 0.5, which becomes more distributed. High variance makes a feature more discriminative, since it responds differently to inputs. Another desirable property is to have the tests uncorrelated, since then each test will contribute to the result. To resolve all these, ORB runs a search among all possible binary tests to nd the ones that have both high variance and means close to 0.5, as well as being uncorrelated. ORB offers performance quite superior both than SIFT and SURF, being orders of magnitude faster with lower computational effort needed. *Figure 4.5* and *Figure 4.6* show the comparisons of average detection time and average number of detected features of various feature detectors [40].

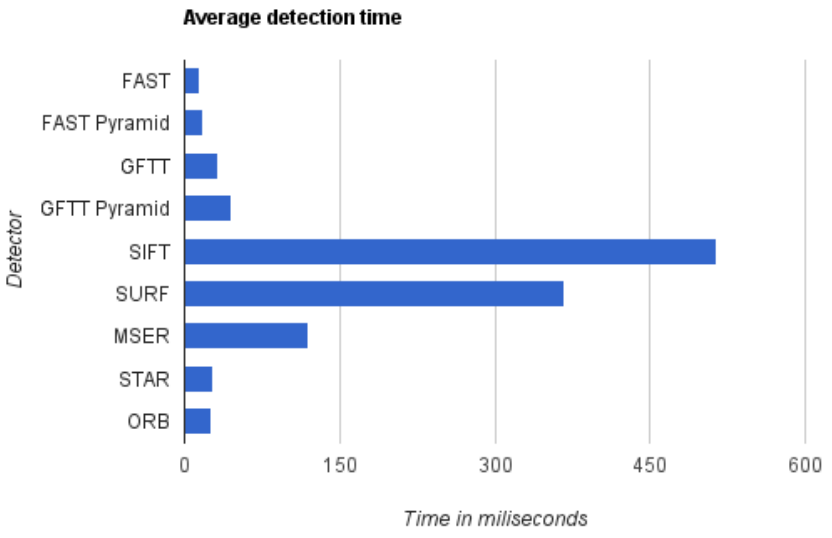

FIGURE 4.5: Average detection time of feature detectors.

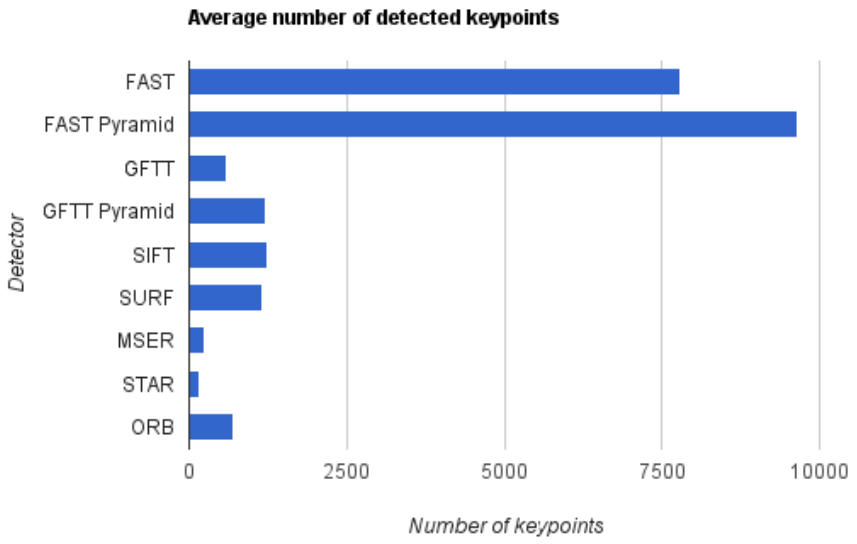

FIGURE 4.6: Average number of detected features of detectors.

Moreover, the feature matching consists that given two images along with their respective keypoints and descriptors extracted, in correlating as precisely as possible each keypoint in the rst image with its corresponding one in the second image. This process can be done by comparing all the descriptors of the two images in terms of a distance, which can be different depending on the kind of descriptor extracted. Each feature in the rst image is then matched with the corresponding feature in the second image which has the lowest distance. The simplest approach is the so called Brute-Force matching each descriptor from the rst set of features is matched with all other feature descriptors in the second set. Matches are then retained in order of distance and only the lowest ones are taken. Distance used are the classical L2 Norm or the Hamming distance. L2 Norm can be expressed as

$$d(D_1, D_2) = \sqrt{\sum_{i=1}^{n} (D_{1i} - D_{2i})^2} \tag{4.23}$$

in which $D1$, $D2$ are the descriptors and d the distance between them. Euclidean distance perfectly fists for SIFT and SURF. Hamming distance is used instead for binary string based descriptors, being a measure in two string of the same length of the number of position in which corresponding symbols are different

$$e.g. \quad dH(D_1, D_2) = dH(1011101, 1001001) = 2 \tag{4.24}$$

This kind of measure works optimally for ORB and BRIEF descriptors, and is particularly fast to compute with respect to the L2 Norm. In using feature matching it has to be considered the fact that not all the features extracted in one image can always be found

in the second one and also that, for similar textured objects, more features can be very similar to each other. This can result in lot of false matches which have to be rejected.

Furthermore, in order to track the detected features of one image in another image, our approach used the Kanade-Lucas-Tomasi (KLT) feature tracker. KLT feature tracker is used for nding sparse pixel wise correspondences and assumes that a point in the nearby space, and uses image gradients to nd the best possible motion of the feature point. If during the tracking procedure, the number of feature points go below 2000, then a new detection is triggered. Also, RANSAC short for "RANdom SAmple Consensus" [39] is an iterative method to fit models to data that can contain outliers. The basic idea is that the data contains inliers, the data points that can be described by the model, and outliers, those that do not fit the model. RANSAC is a very useful outlier rejection algorithm and our approach used it for accurately match the corresponding feature points of two images. *Figure 4.7*, *Figure 4.8* and *Figure 4.9* show varoius possible image changes during camera motion estimation and overall performance of ORB features detector with RANSAC method in two consecutive images.

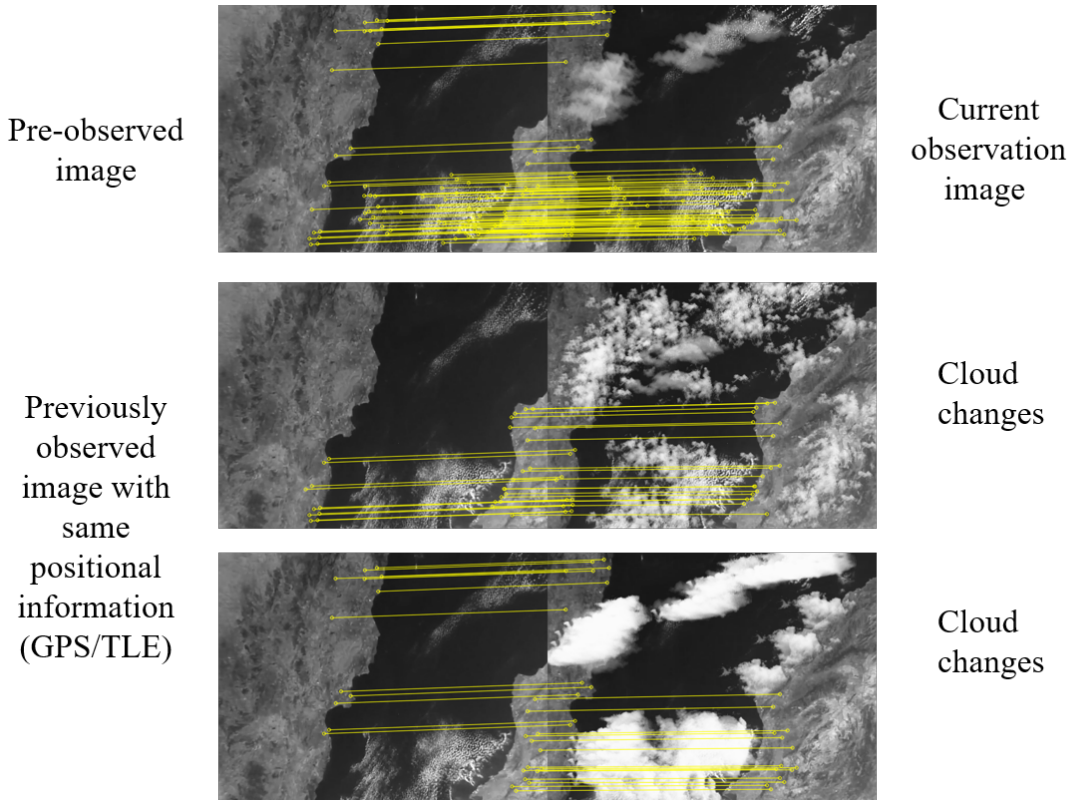

FIGURE 4.7: Simulated images matched with observation image after cloud changes and shifts.

.

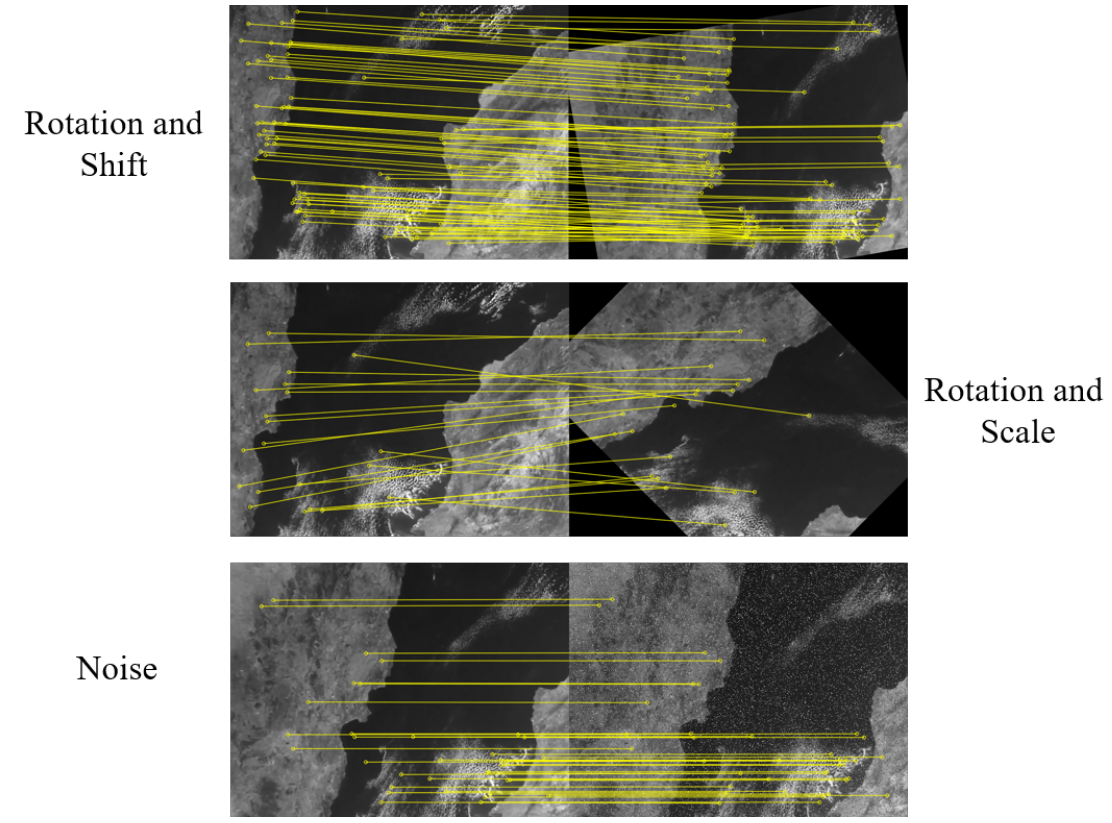

FIGURE 4.8: Simulated images matched with observation image after various transformations and noise applied.

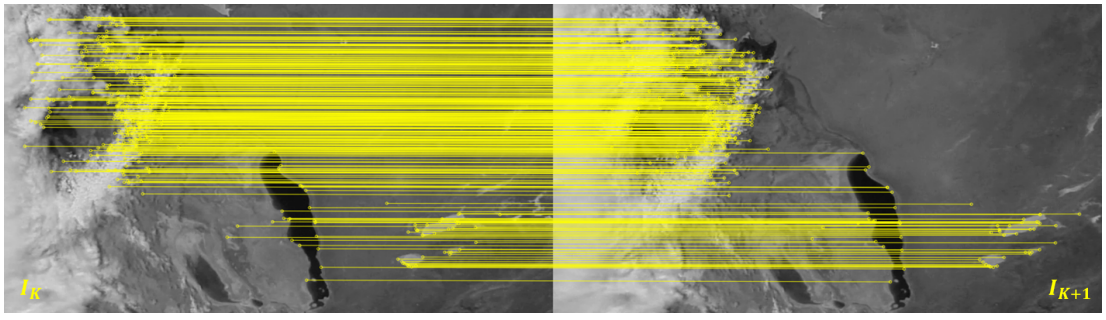

FIGURE 4.9: Corresponding of feature points detected by ORB detector and matched in two successive images.

4.3.4 The planar homography estimation

The planar homography relates the transformation between two image planes. For particular cases where the scene viewed by the camera is planar, it exist the possibility to exploit homography to reconstruct the relation between the features seen in the rst image and the second image and then retrieve motion. The homography matrix is a 3×3 matrix but with 8 degrees of freedom as it is estimated up to a scale. In essence, the homography H maps 2D points in homogeneous coordinates according to

$$\begin{bmatrix} x' \\ y' \\ w' \end{bmatrix} = \begin{bmatrix} h_1 & h_2 & h_3 \\ h_4 & h_5 & h_6 \\ h_7 & h_8 & h_9 \end{bmatrix} \begin{bmatrix} x \\ y \\ w \end{bmatrix} \quad or \quad x' = Hx \tag{4.25}$$

Homogeneous coordinates are a useful representation for points in image planes. As a consequence, the homography H is also only defined up to scale and often points are normalized with $w = 1$ to have a unique identication of the image coordinates x, y. It is generally normalized as

$$h_9 = 1 \quad or \quad h_1^2 + h_2^2 + h_3^2 + h_4^2 + h_5^2 + h_6^2 + h_7^2 + h_8^2 + h_9^2 = 1 \tag{4.26}$$

Moreover, the extra coordinate makes it easy to represent transformations with a single matrix. The following *Figure 4.10* shows a transformation and relationships of homographies of two image planes.

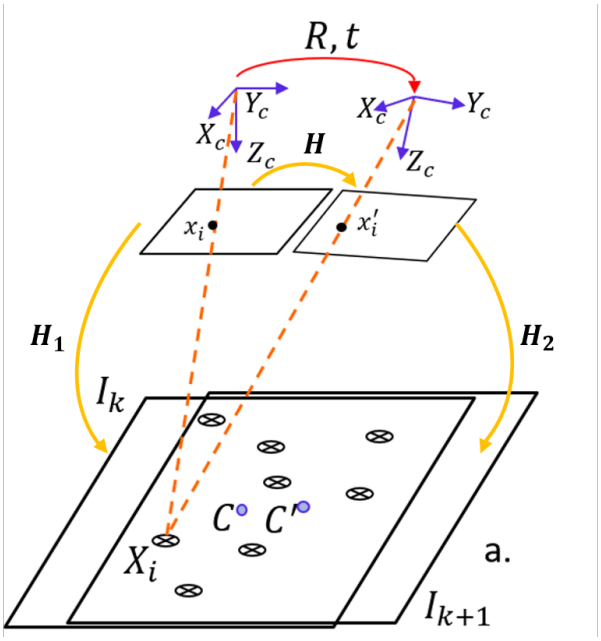

FIGURE 4.10: The relationships of a planar surface and two corresponding image planes.

Homographies can be computed directly from corresponding points in two images planes. As mentioned earlier, a full projective transformation has eight degrees of freedom. Each point correspondence gives two equations, one each for the x and y coordinates,and therefore at least four point correspondences are needed to compute H matrix. The Direct Linear Transformation (DLT) is an algorithm [38] for computing H given four or more correspondences. By rewriting the equation for mapping points using H for several correspondences, the equation will be

$$\begin{bmatrix} -x_1 & -y_1 & -1 & 0 & 0 & 0 & x_1x_1' & y_1x_1' & x_1' \\ 0 & 0 & 0 & -x_1 & -y_1 & -1 & x_1y_1' & y_1y_1' & y_1' \\ -x_2 & -y_2 & -1 & 0 & 0 & 0 & x_2x_2' & y_2x_2' & x_2' \\ 0 & 0 & 0 & -x_2 & -y_2 & -1 & x_2y_2' & y_2y_2' & y_2' \\ . & . & . & . & . & . & . & . & . \end{bmatrix} \begin{bmatrix} h_1 \\ h_2 \\ h_3 \\ h_4 \\ h_5 \\ h_6 \\ h_7 \\ h_8 \\ h_9 \end{bmatrix} = 0 \tag{4.27}$$

or we can write as

$$Ah = 0 \tag{4.28}$$

and then

$$A^TAh = A^T0 \tag{4.29}$$

$$(A^TA)h = 0 \tag{4.30}$$

$$A^TA = UDU^T \tag{4.31}$$

where A is a matrix with twice as many rows as correspondences of two images. By stacking all corresponding points, a least squares solution for H can be found using Singular Value Decomposition (SVD) method as shown above.

OpenCV library comes with an already implemented algorithm to calculate homography between two planes using RANSAC in order to improve the solution in case of outliers. Many different random subsets of points are used to estimate H along with a quality measurement, the best subset is then used to produce the initial H estimate which is further rened with the Levenberg-Marquardt method to reduce reprojection error.

4.3.5 Attitude estimation from the planar Homography

As mentioned previously, H is the homography matrix that maps the points in the first camera frame to the corresponding points in the second camera frame. Also, the homography related to a specific plane computed from the camera displacement can be expressed as

$$H = {}^{2}R_{1} - \frac{{}^{2}t_{1} \cdot n^{T}}{d} \tag{4.32}$$

where n is the normal vector of the plane and d the distance between the camera frame and the plane along the plane normal. Also, the rotation matrix that represents the rotation between the two camera frames is

$${}^{2}R_{1} = {}^{c_2}R_{0} \cdot {}^{c_1}R_{0}{}^{T} \tag{4.33}$$

and the translation vector between the two camera frames is

$${}^{2}t_{1} = {}^{c_2}R_{0} \cdot (- {}^{c_1}R_{0}{}^{T} \cdot {}^{c_1}t_{0}) + {}^{c_2}t_{0} \tag{4.34}$$

The problem of Euclidean homography decomposition, also called Euclidean reconstruction from homography, is that of retrieving the elements R, t and n from matrix H

$$H \Rightarrow \{R, t, n\} \tag{4.35}$$

Notice that the translation is estimated up to a positive scalar factor (as t has been normalized with respect to d').

SVD-based decomposition method

Decomposing an homography matrix in order to obtain attitude information of the camera between two consecutive frames in terms of rotation R and translation t is not straight forward. Different numerical procedures and analytical solutions exists to solve this problem [33]. The homography decomposition problem was first solved by Faugeras and Lustman (1988), and they proved that the decomposition problem has eight different solutions except in some special cases. The decomposition method proposed by Faugeras and Lustman (1988) uses a singular value decomposition $H = U\Lambda V^{T}$ to transform the problem to an equivalent problem with a diagonal homography matrix Λ. This transformed problem can be solved analytically, and then a transformation of the obtained solutions back to the original problem using U and V gives the sought congurations. Out of the eight mathematical solutions, only two are in fact physically possible, and it

is shown in the paper that the impossible ones can be discarded if one has access to a number of point correspondences that are mapped by the homography between the two views. This is done by requiring that all the viewed scene points are in front of both cameras.

If we perform the singular value decomposition of the homography matrix [33]:

$$H = U\Lambda V^T \tag{4.36}$$

we get the orthogonal matrices U and V and a diagonal matrix Λ, which contains the singular values of matrix H. We can consider this diagonal matrix as an homography matrix as well, and hence apply relation *Equation 4.37* to it:

$$\Lambda = R_\Lambda + t_\Lambda n_\Lambda^T \tag{4.37}$$

Computing the components of the rotation matrix, translation and normal vectors is simple when the matrix being decomposed is a diagonal one. First, t_Λ can be easily eliminated from the three vector equations coming out from *Equation 4.37*. Then, imposing that R_Λ is an orthogonal matrix, we can linearly solve for the components of n_Λ, from a new set of equations relating only these components with the three singular values. As a result of the decomposition algorithm, we can get up to 8 different solutions for the triplets: $R_\Lambda, t_\Lambda, n_\Lambda$. Then, assuming that the decomposition of matrix Λ is done, in order to compute the nal decomposition elements, we just need to use the following expressions:

$$R = UR_\Lambda V^T \tag{4.38}$$

$$t = Ut_\Lambda \tag{4.39}$$

$$n = Vn_\Lambda \tag{4.40}$$

As already mentioned, there are up to 8 solutions in general for this problem. These are 8 mathematical solutions, but not all of them are physically possible. Several constraints can be applied in order to reduce this number of solutions.

4.4 Camera Calibration

In many vision-based approaches, the correction for lens distortion was considered to improve the accuracy of the estimation methods. In general, the calibrating a camera means determining the internal camera parameters. In this case the matrix K formed as

$$K = \begin{bmatrix} f_x & 0 & c_x \\ 0 & f_y & c_y \\ 0 & 0 & 1 \end{bmatrix} \tag{4.41}$$

where the camera calibration matrix contains the intrinsic parameters of the camera (the principal point c_x, c_y and the focal lengths f_x and f_y, can be factored out on the left.

No lenses are perfect and the low-cost lenses used in many vision sensors are far from perfect. Lens imperfections result in a variety of distortions including color fringing, spherical aberration or variation in focus across the scene, and geometric distortions where points on the image plane are displaced from where they should be according to in *Equation 4.43*.

Moreover, radial distortion causes image points to be translated along radial lines from the principal point. The radial error is well approximated by a polynomial as

$$\delta r = K_1 r^3 + k_2 r^5 + k_3 r^7 + \cdots \tag{4.42}$$

where r is the distance of the image point from the principal point.

$$u^d = u + \delta_u \quad v^d = v + \delta_y \tag{4.43}$$

where the displacement is

$$\begin{pmatrix} \delta_u \\ \delta_v \end{pmatrix} = \begin{pmatrix} u(K_1 r^2 + k_2 r^4 + k_3 r^6 + \cdots) \\ v(K_1 r^2 + k_2 r^4 + k_3 r^6 + \cdots) \end{pmatrix} + \begin{pmatrix} p_1 uv + p_2(r^2 + 2u^2) \\ p_1(r^2 + 2v^2) + 2p_1 uv \end{pmatrix} \tag{4.44}$$

In this equation, first part represents the radial distortion and second part describes the tangential distortion. This displacement vectors indicate the displacement required to correct the distortion at different points in the image, in fact $(-\delta_u, -\delta_v)$, and shows dominant radial distortion. Typically three coefficients are sufficient to describe the radial distortion and the distortion model is parameterized by $(k_1, k_2, k_3, p_1, p_2)$ which are considered as additional intrinsic parameters. *Figure 4.11* shows examples of a distorted and undistorted images.

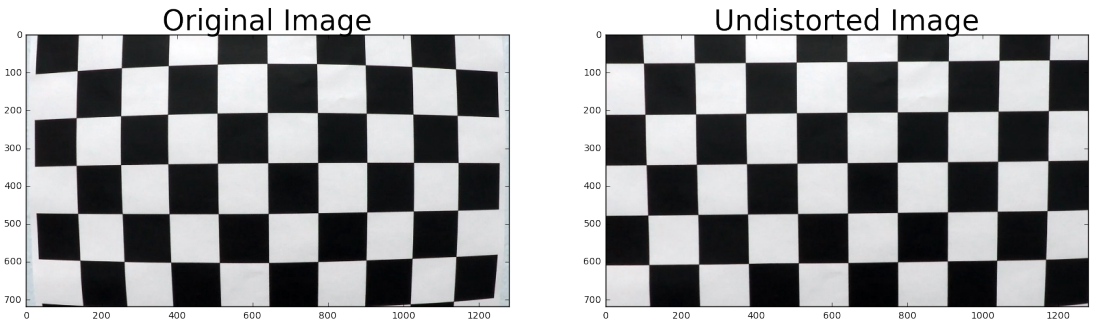

FIGURE 4.11: Distorted image with the curvature of the top row of the squares and undistorted image.

In our vision-based approach, the experimental camera is calibrated using the Camera Calibration Toolbox developed by Jean-Yves Bouguet [41]. Following set of checkerboard pattern images captured by the experimental camera and analyzed. *Figure 4.12* shows the set of the calibration poster images in various different positions that are used in the calibration algorithm. *Figure 4.12* and *Figure 4.13* show the computed extrinsic parameters and complete distortion model of radial and tangential on each pixel of the image.

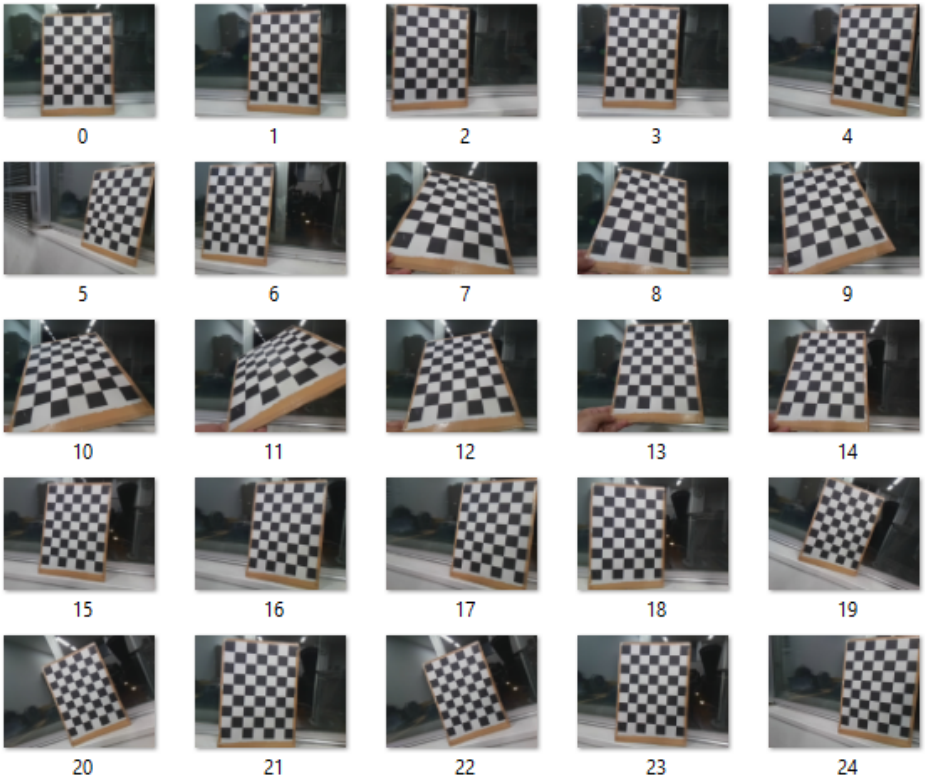

FIGURE 4.12: Images of the calibration checkerboard.

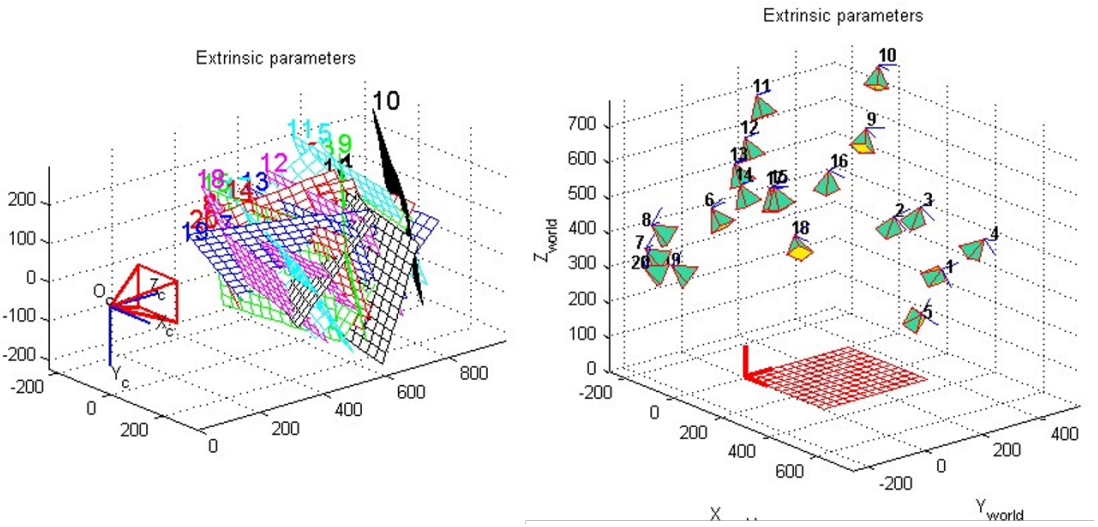

FIGURE 4.13: Computed extrinsic parameters.

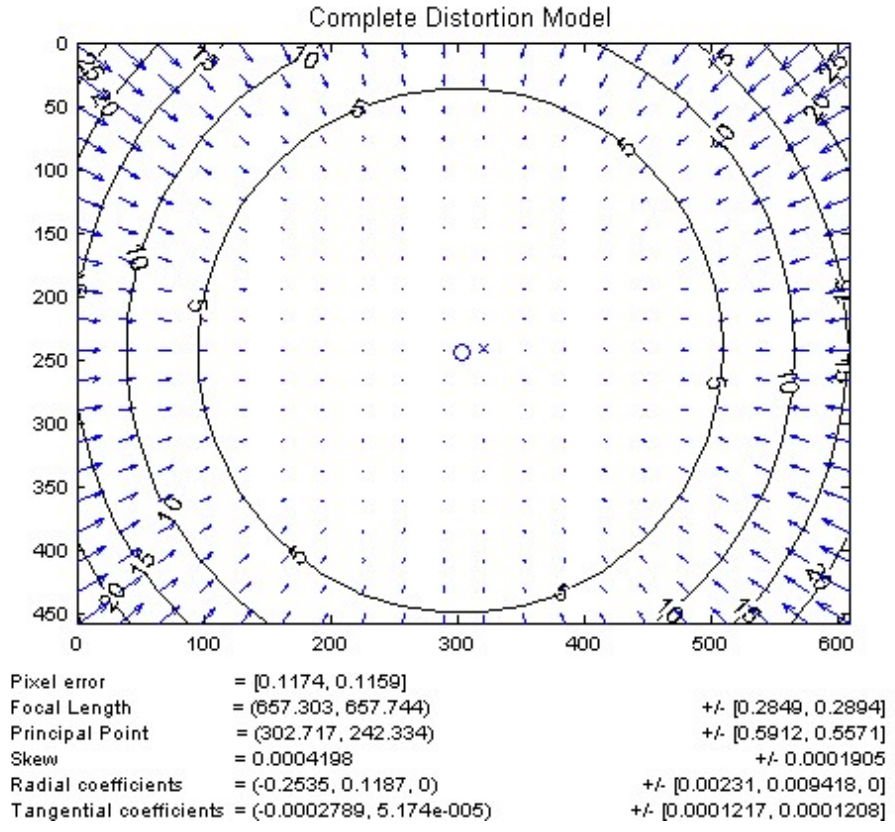

FIGURE 4.14: The calculated complete distortion model of radial and tangential.

4.5 Sensor Fusion Framework

As noted earlier, the attitude determination system that will be used on a particular CubeSat depends on many things including size, available power, and cost. In what follows, system architecture for a multisensor attitude determination system is described. Before describing the system architecture, a brief overview of the sensor fusion algorithm used is given. An illustration of the proposed sensor fusion framework is shown in *Figure 4.15*.

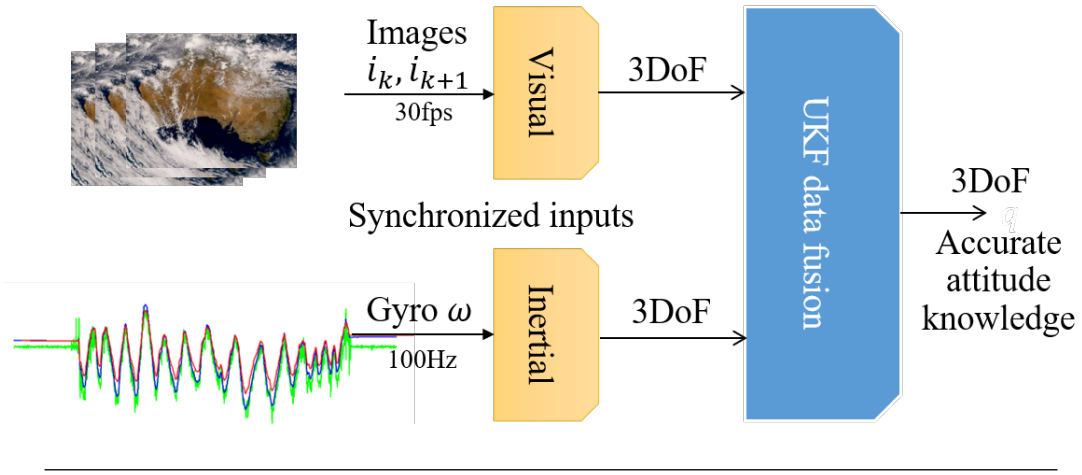

FIGURE 4.15: Sensor fusion approach using Unscented Kalman Filter.

Combining information from multiple sensor types can be achieved with a sensor fusion algorithm. Kalman filter and its extensions are among the most popular methods of data fusion. The Kalman filter was invented in the 1950's by Rudolph Emil Kalman, as a technique for filtering and prediction in linear systems. It is a method applicable only to systems represented with continuous states and uses moment representation with mean and covariance to calculate momentary estimates of the state. In order to obtain Gaussian estimations of the state given some measurements, state and measurements probability must be linear with Gaussian noise, and initial state estimate must be normal distributed. These assumptions of linear state transitions and linear measurements with Gaussian noise are rarely met in practice. For this reason Extended Kalman Filter has been developed: EKF overcomes the linearity assumption making use of non-linear state and measurements probability functions. The EKF has become in recent years the most popular method for state estimation in wide range variety of applications. Its strength lies in its simplicity and in its computational efciency. However, a limitation of the EKF arises however from the fact that it approximates state transitions and measurements using linear Taylor expansions. While an EKF solves the problem of nonlinearity with gradual expansion of linear algorithm, an Unscented Kalman Filter takes unique appraoch which eliminates this linearization process. UKF is mainly based

on Unscented Transformation (UT) and free of the problem of divergence which is caused by linear models obtained through Jacobian [42].

4.5.1 The Unscented Transformation

The unscented transformation takes samples from a Gaussian distribution that then have the system nonlinear function applied to them individually. UT is similar in its concept with Monte Carlo simulation which randomly selects sample, but this method makes a delicate selection of weighting for each sample. This significantly reduces the number of samples required compared to Monte Carlo simulation. An illustration of the principle is given in *Figure 4.16*, from Julier and Uhlmann (1997) [25]. For whatever sample set estimating, an appropriate vector length of the random variable, x, of size n for the appropriate state and parameters. A set of $2n + 1$ sample points, also known as sigma points is taken from a Gaussian distribution such that the mean and covariance of the untransformed set are x_m and P_x respectively.

Consider a state variable x that follows a normal distribution with mean x_m and covariance P_x.

$$x \approx N(x_m, P_x) \tag{4.45}$$

The purpose of unscented transformation is to get the mean and covariance of an arbitrary function $f(x)$ when x satisfies *Equition 4.45*.

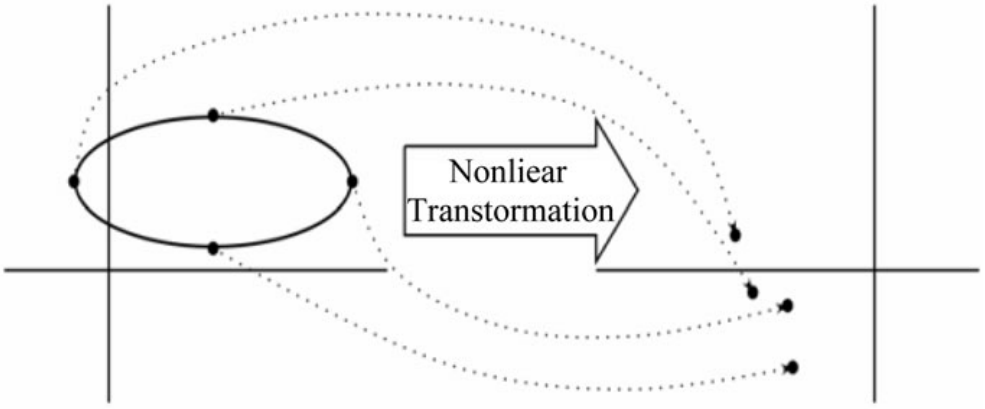

FIGURE 4.16: .

]Basic principle behind the unscented transformation [28].

First define the sigma points χ_i and weights W_i for x as following

$$\chi_1 = x_m \tag{4.46}$$

$$\chi_{i+1} = x_m + u_i \qquad i = 1, 2, \cdots, n \tag{4.47}$$

$$\chi_{i+n+1} = x_m - u_i \qquad i = 1, 2, \cdots, n \tag{4.48}$$

$$W_1 = \frac{k}{n+k} \tag{4.49}$$

$$W_{i+1} = \frac{1}{2(n+k)} \qquad i = 1, 2, \cdots, n \tag{4.50}$$

$$W_{i+n+1} = \frac{1}{2(n+k)} \qquad i = 1, 2, \cdots, n \tag{4.51}$$

where u_i is a row vector from the following matrix U and k is an arbitrary constant.

$$U^T U = (n+k)P_x \tag{4.52}$$

Then the mean and covariance of the function $y = f(x)$ could be computed as following

$$\mathcal{y}_m = \sum_{i=1}^{2n+1} W_i f(\chi_i) \tag{4.53}$$

$$P_y = \sum_{i=1}^{2n+1} W_i \{f(\chi_i) - \mathcal{y}_m\}\{f(\chi_i) - \mathcal{y}_m\}^T \tag{4.54}$$

The weights W_i are the constants determining the weighting of each sigma point when computing mean and covariance. The sigma points and weights in *Equation 4.46* to *Equation 4.51* satisfy following characteristics

$$x_m = \sum_{i=1}^{2n+1} W_i(\chi_i) \tag{4.55}$$

$$P_x = \sum_{i=1}^{2n+1} W_i \{\chi_i - x_m\}\{\chi_i - x_m\}^T \tag{4.56}$$

The power in the unscented transformation lies in a few crucial differences from the EKF that allow it to capture the mean and covariance of the state to second order, be numerically stable with the appropriate matrix square root method.

4.5.2 The Unscented Kalman Filter for attitude estimation

The basic idea behind the Unscented Kalman Filter is that it is easier to approximate a Gaussian distribution than it is to approximate an arbitrary nonlinear function. Instead of linearizing the Jacobian matrices, the UKF uses a rational deterministic sampling approach to capture the mean and covariance estimates with a minimal set of sample points. In this section, we present an algorithmic description of the UKF omitting some theoretical considerations, left to [42].

The system model is given by

$$x_{k+1} = f(x_k) + G_k w_k \tag{4.57}$$

$$z_k = h(x_k) + v_k \tag{4.58}$$

where w_k and v_k represent the process and measurement-error noises, these are zero-mean Gaussian noise processes with covariances given by Q_k and R_k, respectively.

In order to estimate attitude, the state vector is composed of Euler attitude angles and gyro biases as

$$x(k) = \begin{bmatrix} \varphi & \theta & \psi & \varepsilon_x & \varepsilon_y & \varepsilon_z \end{bmatrix}^T \tag{4.59}$$

Attitude angles and gyro angular velocity biases are modelled as follows

$$\dot{\varphi}(t) = \hat{\omega_x} + \hat{\omega_y} \sin\hat{\varphi} \tan\hat{\theta} + \hat{\omega_z} \cos\hat{\varphi} \tan\hat{\theta} \tag{4.60}$$

$$\dot{\theta}(t) = \hat{\omega_y} \cos\hat{\varphi} - \hat{\omega_z} \sin\hat{\varphi} \tag{4.61}$$

$$\dot{\psi}(t) = \hat{\omega_y} \sin\hat{\varphi} \sec\hat{\theta} + \hat{\omega_z} \cos\hat{\varphi} \sec\hat{\theta} \tag{4.62}$$

$$\dot{\varepsilon}(t) = 0 \tag{4.63}$$

The measurement vector $z(k)$ is defined as follows

$$x(k) = \begin{bmatrix} \varphi_{vis} & \theta_{vis} & \psi_{vis} \end{bmatrix}^T \tag{4.64}$$

In the state vector, where φ (roll), θ (pitch) and ψ (yaw) are the rotation angles about the $x-$, $y-$ and $z-$ axes, but it is not of concern in this study. These come from the integration of the rate of change of gyros, while ε_x, ε_y and ε_z are biases from gyro in $x-$, $y-$ and $z-$ axis, respectively. We use the measurement from the vision-based based approach in order to calculate φ_{vis}, θ_{vis} and ψ_{vis} as measurement vector.

The computation algorithm starts with initial values

$$\hat{x_0} = E\big[x_0\big] \tag{4.65}$$

$$P_0 = E\big[(x_0 - \hat{x_0})(x_0 - \hat{x_0})^T\big] \tag{4.66}$$

Then, sigma points and weights are defined by

$$\chi_1 = \hat{x_{k-1}} \tag{4.67}$$

$$\chi_{i+1} = hatx_{k-1} + \sqrt{(n+k)P_{k-1}} \qquad i = 1, 2, \cdots, n \tag{4.68}$$

$$\chi_{i+n+1} = hatx_{k-1} - \sqrt{(n+k)P_{k-1}} \qquad i = 1, 2, \cdots, n \tag{4.69}$$

$$W_1 = \frac{k}{n+k} \tag{4.70}$$

$$W_{i+1} = \frac{1}{2(n+k)} \qquad i = 1, 2, \cdots, n \tag{4.71}$$

$$W_{i+n+1} = \frac{1}{2(n+k)} \qquad i = 1, 2, \cdots, n \tag{4.72}$$

where k is a scaling parameter, n is the state number, respectively. $\sqrt{P_{k-1}}$ can be computed with the lower triangular Cholesky factorization.

The state and error covariance are predicted by

$$\hat{x}_k^- = \sum_{i=1}^{2n+1} W_i f(\chi_i) \tag{4.73}$$

$$P_k^- = \sum_{i=1}^{2n+1} W_i \big\{f(\chi_i) - \hat{x}_k^-\big\}\big\{f(\chi_i) - \hat{x}_k^-\big\}^T + Q_k \tag{4.74}$$

The measurement and covariance are predicted by

$$\hat{z}_k^- = \sum_{i=1}^{2n+1} W_i h(\chi_i) \tag{4.75}$$

$$P_z^- = \sum_{i=1}^{2n+1} W_i \big\{h(\chi_i) - \hat{z}_k\big\}\big\{h(\chi_i) - \hat{z}_k\big\}^T + R_k \tag{4.76}$$

where R_k represents the measurement error covariance matrix.

Kalman gain is defined by

$$P_{xz} = \sum_{i=1}^{2n+1} W_i \big\{f(\chi_i) - \hat{x}_k^-\big\}\big\{h(\chi_i) - \hat{z}_k\big\}^T \tag{4.77}$$

$$K_k = P_{xz} P_z^{-1} \tag{4.78}$$

Finally, the estimate and error covariance equations are

$$\hat{x}_k = \hat{x}_k^- + K_k(z_k - \hat{z}_k) \tag{4.79}$$

$$P_k = P_k^- - K_k P_z K_k^T \tag{4.80}$$

The performance of the application of UKF sensor fusion approach with the formulated kinematic equations to the satellite attitude data is presented in following sections. *Figure 4.17* shows the structure of the proposed sensor fusion framework combined with the unscented Kalman filter algorithm.

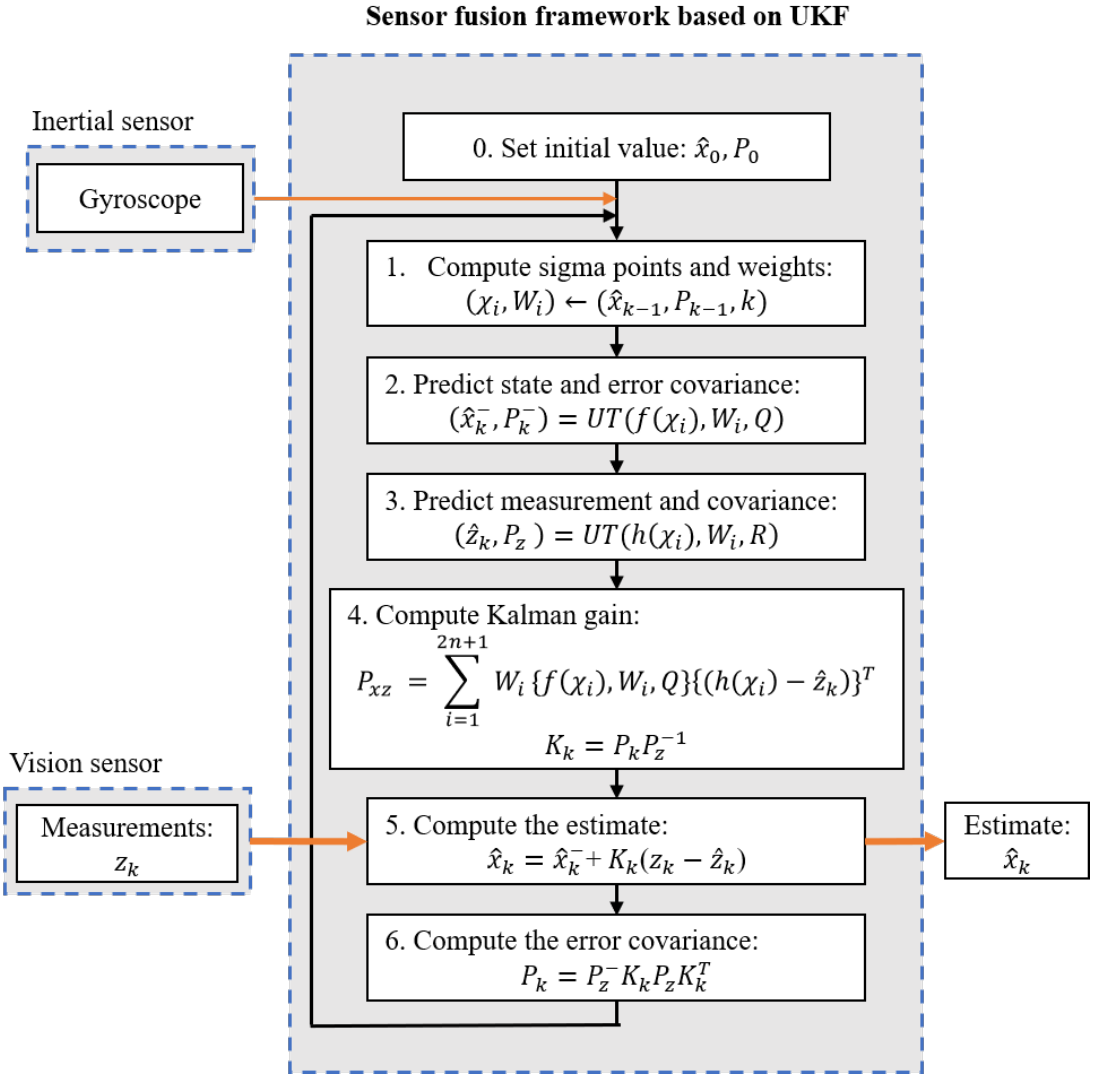

FIGURE 4.17: Structure of the proposed sensor fusion approach.

4.6 Experimental Setup

In order to evaluate the performance of the proposed visual-inertial approach, a controlled experiment is designed to generate data sets of known attitudes to support algorithm development and study variations, as well as studying the estimation accuracy and the computational cost. The experiments are based on images of the actual International Space Station's (ISS) HDEV payload's nadir-pointing camera's imagery data [43]. Regarding prototype hardware, we used Raspberry Pi 3 model B single board computer, an inexpensive 5 mega pixel Omnivision 5647 camera module and MPU6050 inertial sensor's 3-axis Gyroscope for logging synchronized data sets. Laboratory test environment and experimental setup for a visual-inertial attitude determination approach are shown in *Figure 4.18* and *Figure 4.19*. The main purpose of the laboratory experiment is accurately generate known attitude changes and same time provide a realistic input images for camera sensor. By projecting imagery data into the scene, we propagated the attitude information of the prototype by the proposed visual-inertial approach. However, lacking the attitude data information of the corresponding HDEV payload's imagery data, we carried out the experiment using a high-precision one axis rate table.

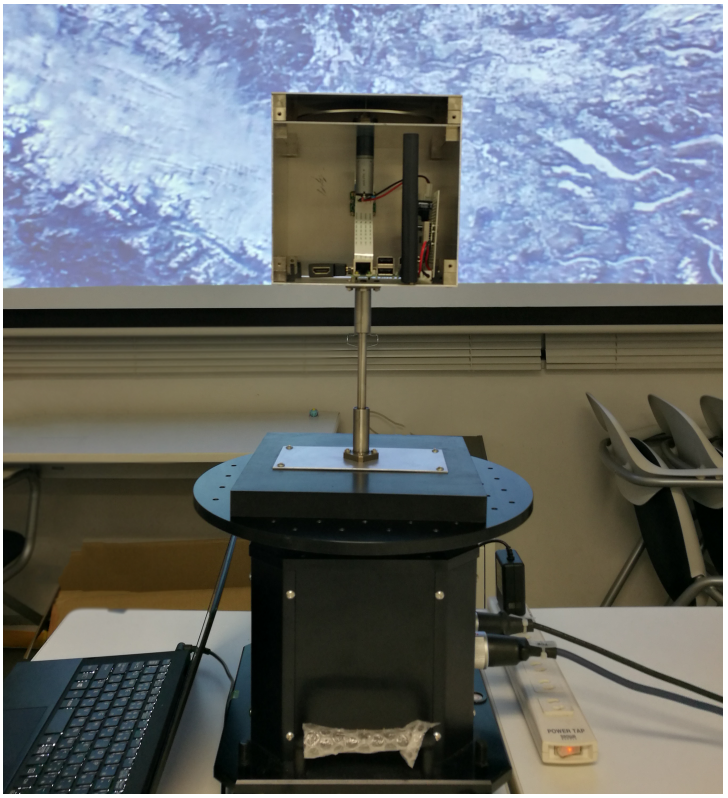

FIGURE 4.18: Laboratory test environment and experimental setup.

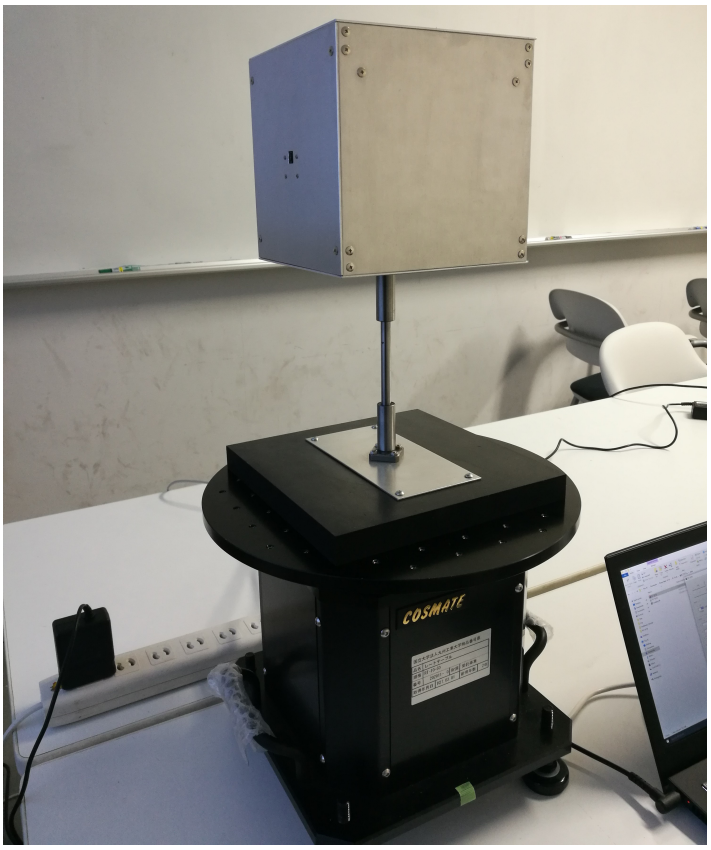

FIGURE 4.19: Prototype hardware design for the visual-inertial approach.

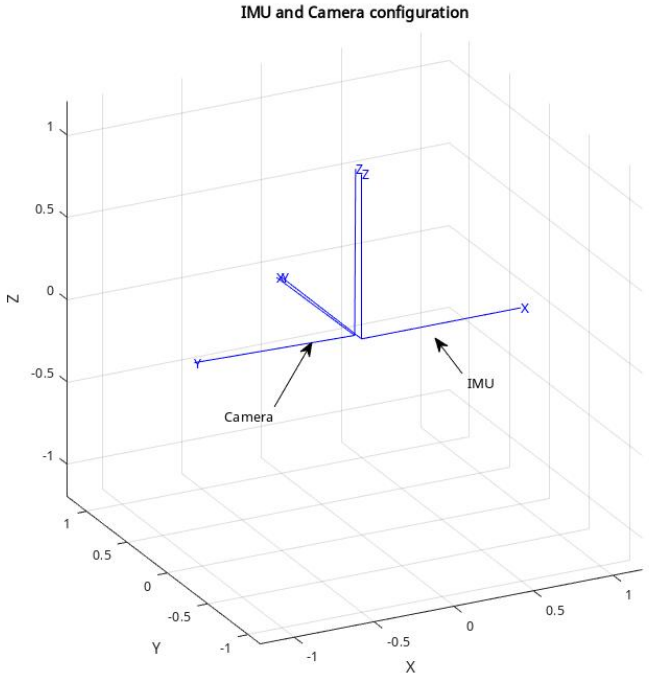

FIGURE 4.20: Transformation of visual and inertial sensor after the calibration.

In order to fuse visual and inertial measurements into the UKF framework, the sensor measurements have to be synchronized. The proposed approach utilized time synchronized image acquisitions and inertial measurements. In addition, visual and inertial sensors are rigidly attached to the prototype's mechanical structure and relative rotation and translation remains constant. After determining the transformation matrix (relative rotation and translation), the vision-based method's measurements were transformed and simultaneously fused within the UKF framework with the triad rate gyro's measurements. *Figure 4.20* shows the transformation of visual and inertial sensor after the calibration procedure.

4.7 Experimental Results and Performance Evaluation

Two different experiments are carried out to check the validity of the attitude estimation.

In only vision-based approach experiment, we propagated the attitude changes of the experimental prototype by only vision-based method. HDEV payload's imagery data and high-precision one axis rate table are used to provide attitude changes. The vision-based approach's experimental process consisted of two estimation steps:

- Initial attitude estimation test: we estimated the attitude of the experimental prototype by using HDEV payload's imagery data with the vision- based method without any additional change of attitude.
- Relative attitude estimation test: we applied a pitch angle change to the experimental prototype during the second attitude estimation process by using a high precision one axis rate table. After these experiments, we subtracted the first estimated attitude data from the second estimated attitude data to obtain the applied attitude change during the second estimation test. Therefore, the performance of the vision- based method can be verified by the high precision one axis rate table.

After these experiments, we subtracted the first estimated attitude data from the second estimated attitude data to obtain the applied attitude change during the second estimation test. Therefore, the performance of the vision-based method can be verified by the high precision one axis rate table. *Figure 4.21* shows the experimental result of the propagated pitch angle measurement during the experiment and its comparison with ground truth data.

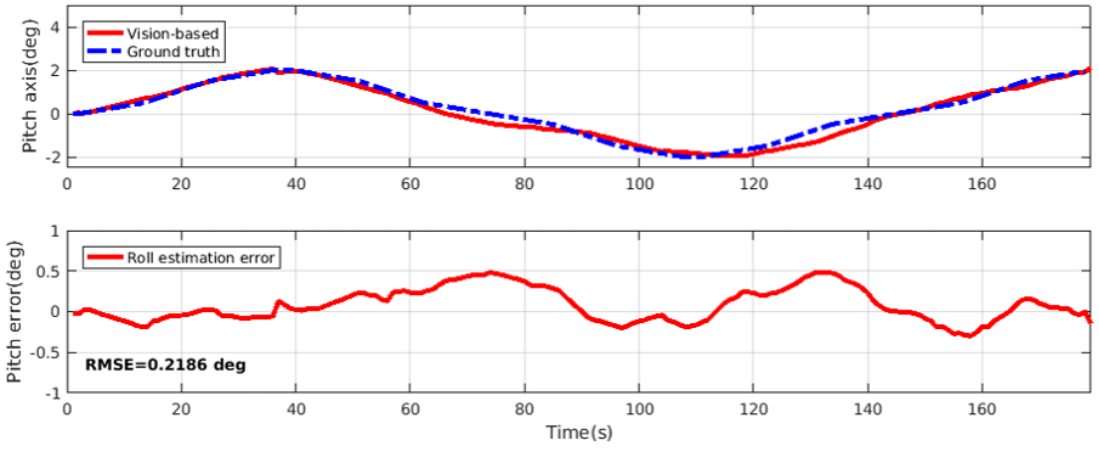

FIGURE 4.21: Experimental results of Vision-based method compared with ground truth data.

The results obtained by the proposed image processing algorithm using HDEV payload's imagery data, can be seen in following images.

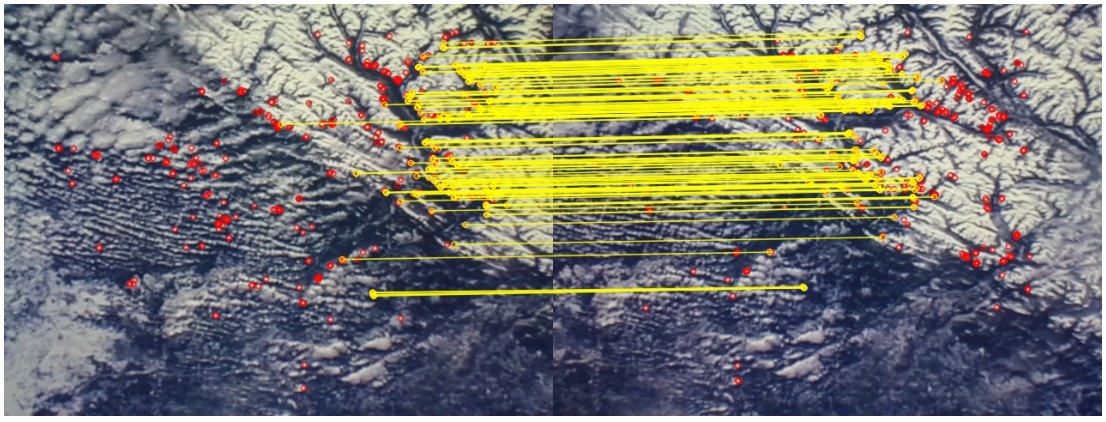

FIGURE 4.22: Result 1 obtained by the proposed image processing algorithm.

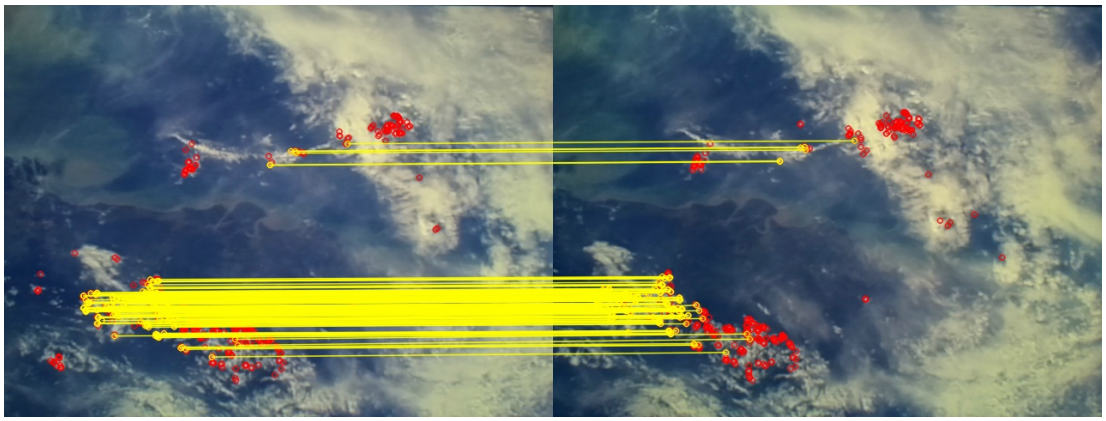

FIGURE 4.23: Result 2 obtained by the proposed image processing algorithm.

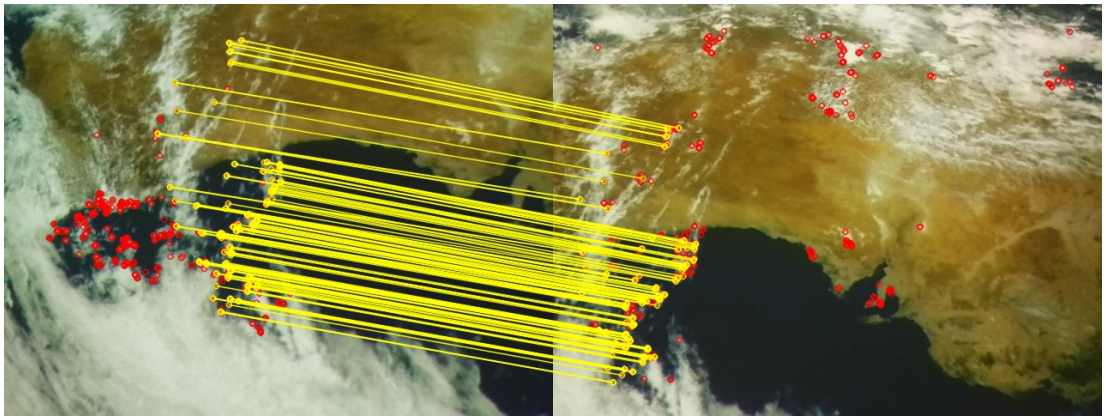

FIGURE 4.24: Result 3 obtained by the proposed image processing algorithm.

In the visual-inertial approach experiment, the performance of our proposed approach using UKF algorithm was tested by using simulated realistic imagery data of Earth-observing satellite and a high precision one axis rate table. UKF algorithm used following set of initial conditions:

- initial attitude: $\varphi = \theta = \psi = 0$ degree
- initial gyro bias: $\varepsilon_x = \varepsilon_y = \varepsilon_z = 10$ deg/hour
- initial covariance (P): $\sigma^2_{\varphi,\theta,\psi} = (0.5deg)^2$ and $\sigma^2_{gb} = (1deg/hour)^2$

The simulation model parameters are shown in *Table 4.1.* For the simulation process, we used the same orbital parameters with the ISS and used real imagery data. In the simulated imagery data projected to the scene, the Earth surface features induced by simulated satellite's translational and earth's rotational motions. During the experimental process, we continuously captured the projected imagery data by experimental prototype's camera and simultaneously we applied a pitch angle change to the experimental prototype by using a high precision one axis rate table. The experimental prototype's attitude (3DOF) propagated by the visual- inertial approach and compared to the high precision one axis rate table's reference value.

Name	**Parameters**	**Value**
Camera	Resolution	$640px \times 480px$
-	Frame rate	25 FPS
-	Pixel size	$1.4\mu m \times 1.4\mu m$
Gyrospoce	Sampling rate	200 Hz
-	Constant drift	10 deg/h
Simulation model	Altitude	$410km$
-	Ground velocity	7.2 km/s
-	Earth radius	6371 km
-	Earth's rotation rate	$7.272 \times 10^{-5} rad/s$

Table 4.1: Specifications of sensors and simulation model.

The following the results obtained by the proposed visual-inertial approach using the experimental prototype and a high-precision one axis rate table. *Figure 4.25*, *Figure 4.26*, *Figure 4.27* and *Figure 4.28* show the experimental results of visual-inertial attitude propagation approach compared to the reference value of the rate table.

.

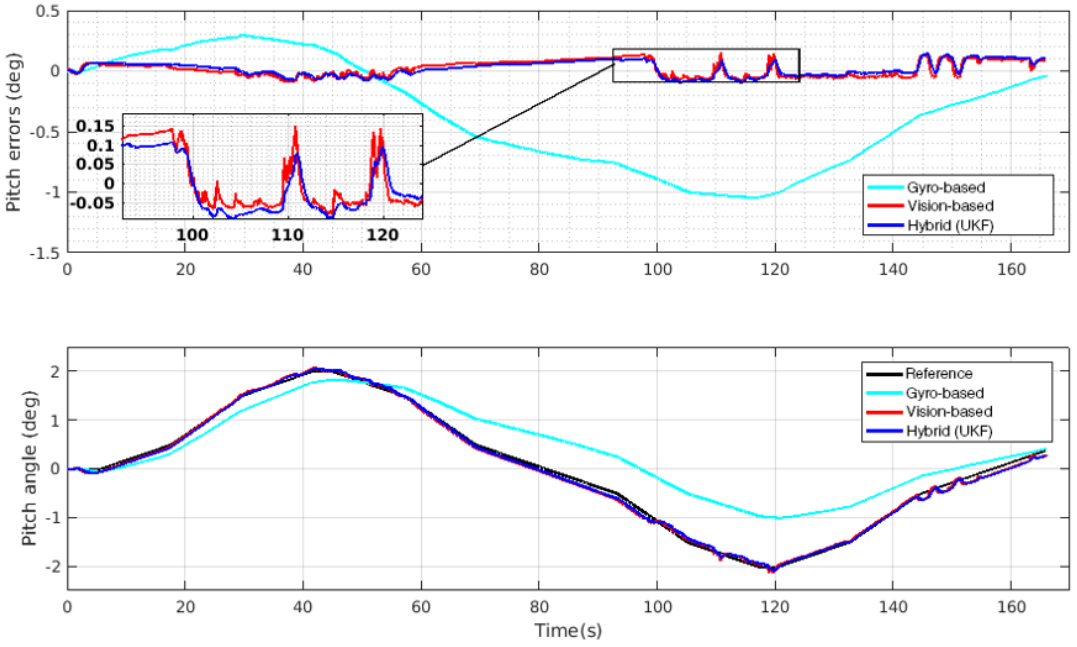

FIGURE 4.25: Comparison between pitch angle estimated by visual-inertial and different approaches.

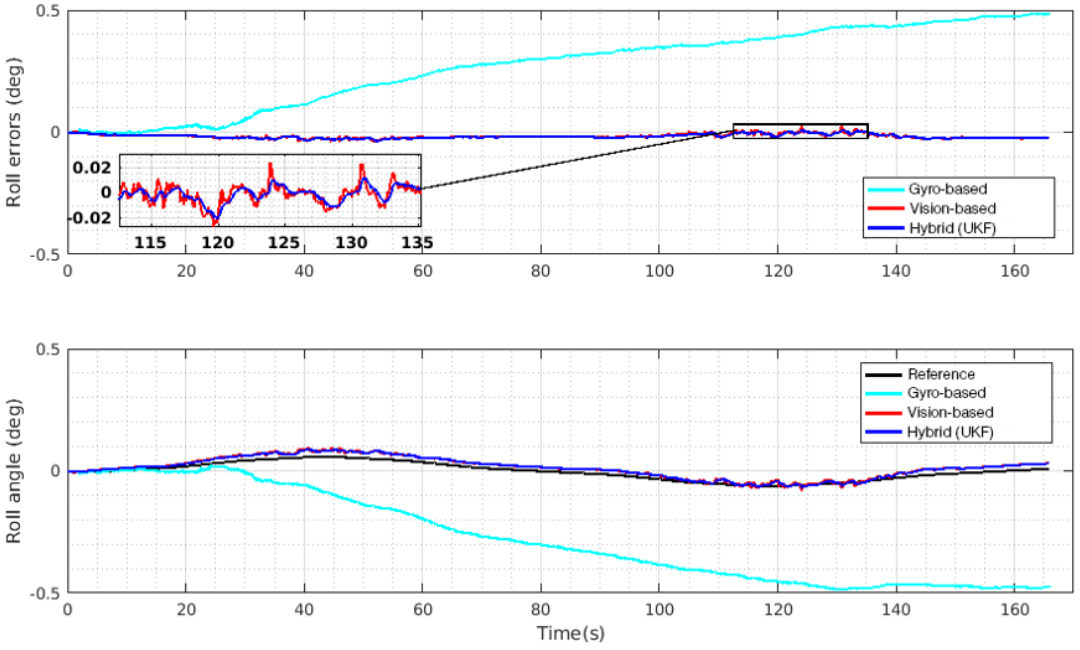

FIGURE 4.26: Comparison between roll angle estimated by visual-inertial and different approaches.

.

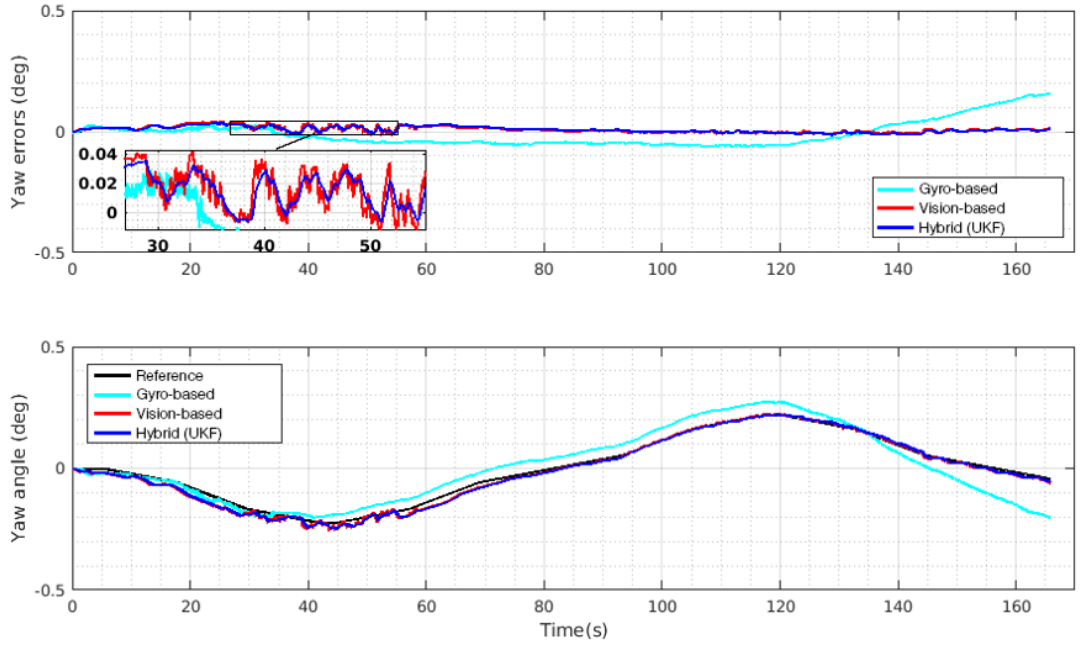

FIGURE 4.27: Comparison between yaw angle estimated by visual-inertial and different approaches.

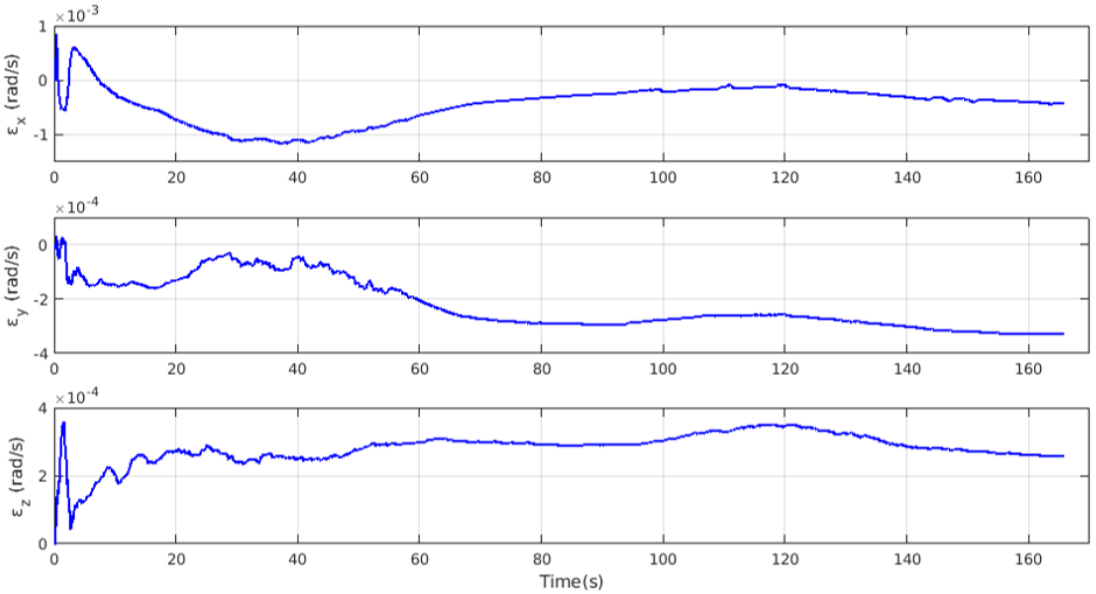

FIGURE 4.28: Gyro biases estimated by Unscented Kalman Filter.

In the only vision-based approach's experiment, the pitch angle measurement accuracy was tested. During the experiment, the high precision one axis rate table rotated its disk from 0.0° to 2.0° and from 2.0° to −2.0° and from −2.0° to 2.0° in period of 180 seconds. The measurement interval time was 0.04 seconds during the experiment. The root-mean square error (RMSE) and maximum error of the measurement are listed in following *Table 4.2*.

Method	RMSE	Maximum error
Only vision-based	0.2186 degrees	0.51 degrees

TABLE 4.2: Measurement errors of only vision-based approach.

Regarding the processing time of the proposed image processing algorithm, the Raspberry Pi single board computer was only used to capture and save images from the scene during experiment due to its limited processing power and portability. After the experiment, the experimental data transformed into the laboratory computer and applied the proposed image processing algorithm. The laboratory computer has a 2.8 GHz processor and 4 GB memory and has Ubuntu 16.04 operating system. The hardware specifications of the laboratory computer has been chosen based on single board computer's limited computational power. The following *Figure 4.29* shows the comparison of the laboratory computer's specification with its equivalent single board computers.

Component	Jetson Nano	Raspberry Pi 4	Virtual Machine
CPU speed	1.4 GHz 64-bit, 4 cores	1.5GHz 64-bit, 4 cores	1.8GHz 64-bit, 2 cores
RAM	4 GB	4GB	4GB
Power consumption	5W/10W	3.4-7.6 W	-
Weight	140grams	46 grams	-

FIGURE 4.29: Comparison between the laboratory computer and equivalent single board computers.

The following *Table 4.3* shows the average process time of the proposed image processing algorithm.

Method	**Time (ms)**	**Camera speed (FPS)**
Only vision-based	311	$\simeq 3$

TABLE 4.3: Average process time the proposed image processing algorithm.

The visual-inertial approach experiment used the same method as only vision-based approach. The Raspberry Pi single board computer was used to save captured images and measurements of triad gyro sensor in same time during the experiments. The each captured images from camera and triad gyro measurements are synchronized and logged with corresponding time-stamps. During the experiment, we applied same rotations to the prototype as only vision-based approach and only the pitch axis changed by rate table and another two axes remained not changed. However, due to small slope angle between the experimental prototype and rate table, it caused small attitude change in another two axes during the experimental process. *Table 4.4* shows measurements of RMSE comparisons of the visual-inertial and only vision-based approaches.

Axis / Approach	**Vision-based (deg)**	**Visual-Inertial (deg)**
Pitch (RMSE)	0.0670	0.0637
Roll (RMSE)	0.0171	0.0168
Yaw (RMSE)	0.0160	0.0154

TABLE 4.4: Comparison of root mean square error for the measurement of two approaches.

Regarding the processing time of the proposed visual-inertial approach, we used the same laboratory computer. The following *Table 4.5* shows the average process time of the proposed algorithm.

Method	**Time (ms)**	**Camera speed (FPS)**
Visual-Inertial	349	$\simeq 3$

TABLE 4.5: Average process time the proposed visual-inertial approach.

Another essential evaluation for the overall scheme is examining the accuracy of the attitude estimations. By using the proposed visual-inertial approach it is possible to determine the attitude of the small satellite with an accuracy of 0.07deg. That shows us it is possible to increase the attitude determination accuracy of a small satellites, which has camera, triad gyros onboard. The observability analysis of the proposed attitude estimation approach has shown that the sensor fusion approach of using complementary inertial sensors is better than using a single sensor. The only drawback of the proposed approach is the increased computational load when compared with the other attitude estimation sensors. In summary the overall attitude estimation scheme increases the accuracy of the attitude determination procedure but requires the computational power.

Chapter 5

Map-based Approach

5.1 Overview

In this chapter, we discuss the map-based attitude determination approach that provides absolute attitude in 3 degrees of freedom (3DOF) based on database images and homography of two sequentially captured images of a planar scene. In a first step, we focus in particular on the methodology of our approach, including the inverted file indexing, vector quantisation, and the absolute attitude determination process. In the next step, the proposed approach is applied to simulated realistic Earth-observation satellite imagery data. Moreover, discussions of simulation and experiment results are presented.

5.2 Image Representation with a visual words

One of the fastest methods for image rapid search and retrieval is bag-of-words (BoW) technique [44]. The bag of words is a technique that uses a visual vocabulary to convert an image into a sparse numerical vector, allowing to manage big sets of images. With a visual vocabulary, images can be represented by visual words. The visual word can be imagined as a representative of an often occurring image patch [45][46]. In order to detect revisited places in satellite captured images we use a map database composed of a bag-of-words and inverse indexes, as shown in following figure.

Visual words can be chosen from a space of descriptions (SIFT features). Each description (SIFT feature) can be understood as a point in this space. We used the visual words by vector quantisation - one visual word for each cluster of descriptors. The database will be represented as a sparse matrix database (DB). Each row of the matrix represents a bag of words representation of one document in the database. Each column of the DB matrix corresponds to a visual word. An element $DB(i, j)$ is non zero if and only if image i contains visual word j. The value of the element $DB(i, j)$ is proportional to the term-frequency of visual word j in image i (how many times this visual word appears in the image) and the inverse document frequency (IDF) weight of the visual word j. The bag of words vector is normalized to unit length: $\sum(DB(i,:)^2) == 1$.

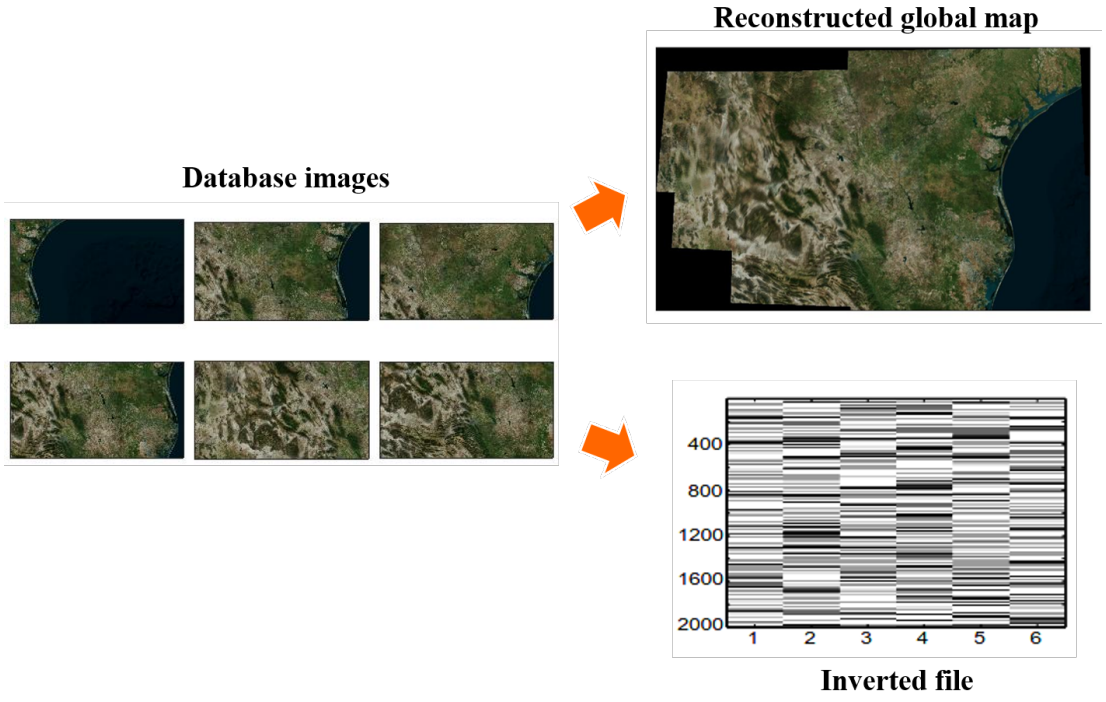

FIGURE 5.1: Visual words are extracted from images and indexed into an inverted file.

5.3 Inverted file indexing

Every images in database is represented by a vector of visual words. A vector representation of the image with counts of visual words can be obtained by summing the occurrences of the same words [47]. To be able to search effectively in the image database, our approach need to estimate the similarity. The standard way is to sum the distances of corresponding descriptions. In the bag of words method the vector quantisation is used to approximate the description distance. The distance between descriptions is 0 if they are assigned to the same visual word and infinity otherwise. For images represented as vectors of visual words we define similarity as:

$$score(x, y) = \cos\varphi = \frac{xy}{||x||||y||} = \frac{1}{||x||||y||}\sum_{i=1}^{D} x_i y_i \tag{5.1}$$

where x and y are vectors of visual words (bags of words). Moreover, a part of the similarity can be computed ahead and normalize the size of vectors. After that, the similarity can be computed as a simple dot product of two vectors.

The visual vocabulary can be very big, often with a few thousands or even millions of words. To simplify the distance estimation between such long vectors, the so called inverted file is used [48]. Inverted file is a structure, which for each visual word (A, B, C, D in the picture) contains a list of images α, β, γ in which the word appears together with the multiplicity. In Matlab is easy to implement this structure as a sparse matrix. Matlab represents a sparse matrix as column lists of elements. Therefore, our inverted file will be a 2D sparse matrix, where columns are visual words and rows are images.

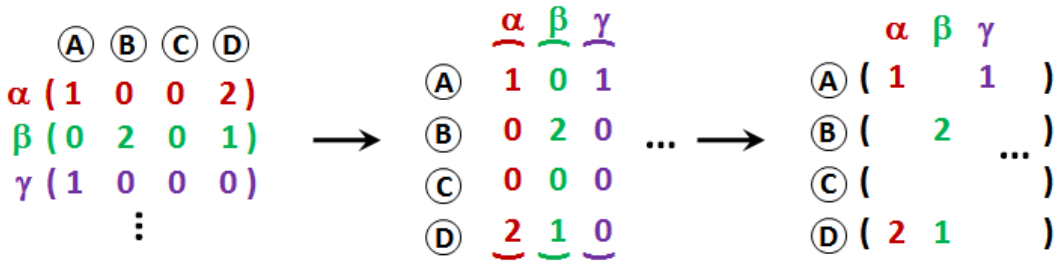

FIGURE 5.2: Inverted file is a structure.

5.3.1 Attitude determination from a global map

Conceptually, the map-based attitude determination approach consists of three main parts. The first part builds a global map and index file using feature extraction method and vector quantisation then efficiently store it in memory. The second part directly obtains satellite captured raw image then extract visual words histogram to rapidly search image features in global map. In the third part, based on similarity of between matched images in global map, the selected image is used to obtain absolute attitude knowledge by decomposing from the homography [49] from the captured image to the a global map matched image as described in previous chapter. *Figure 5.3* shows a block diagram of the proposed map-based approach for determination of attitude information with camera sensor.

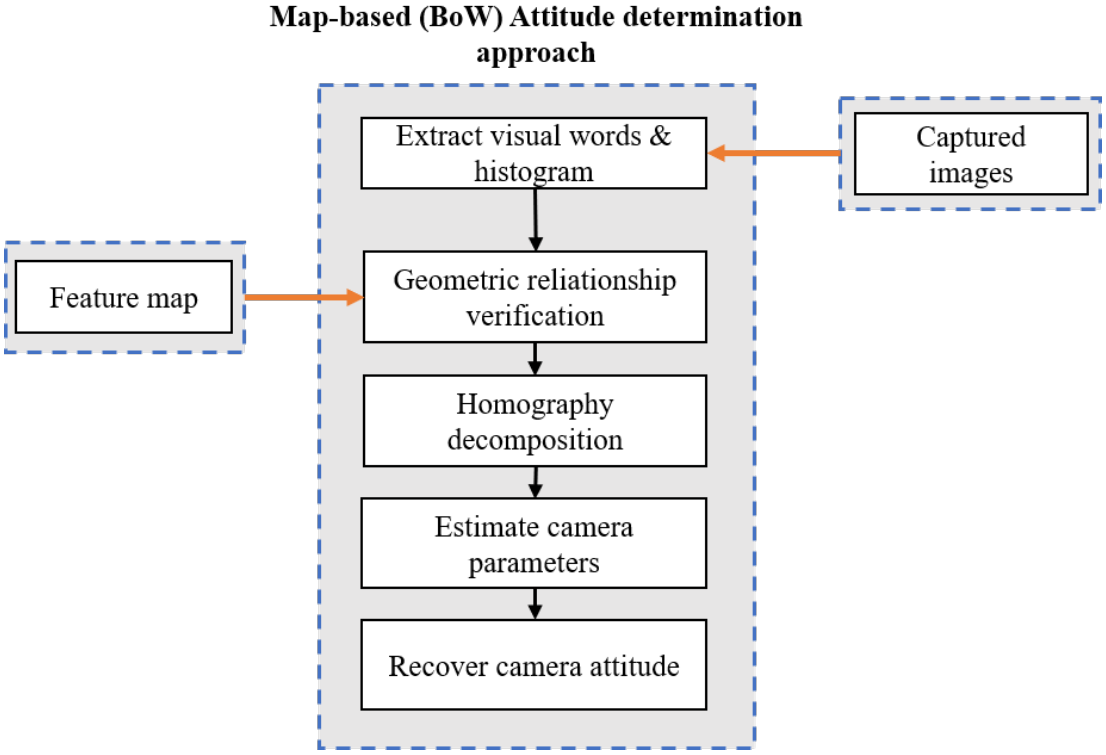

FIGURE 5.3: The block diagram of the proposed map-based method.

5.3.2 Simulation and experimental results

In the map-based approach, the performance of our proposed approach tested by using simulated realistic imagery data of Sentinel-2 Earth-observing satellite and Cesium web-based simulation platform [50]. The simulation model parameters were same as Visual-Inertial approach. For the simulation process, we used the same orbital parameters with the ISS and used Sentinel-2 imagery data. In the web-based simulation platform, the Earth surface features induced by simulated satellite's orbit parameters, attitude changes and camera parameters. During the experimental process, we captured the Earth imagery data by simulated satellite's camera and used the captured images to build global map. After the building global map, we applied our proposed approach to recover satellite attitude based on corresponding captured images. The simulation environment of proposed attitude determination approach is shown in *Figure 5.4*.

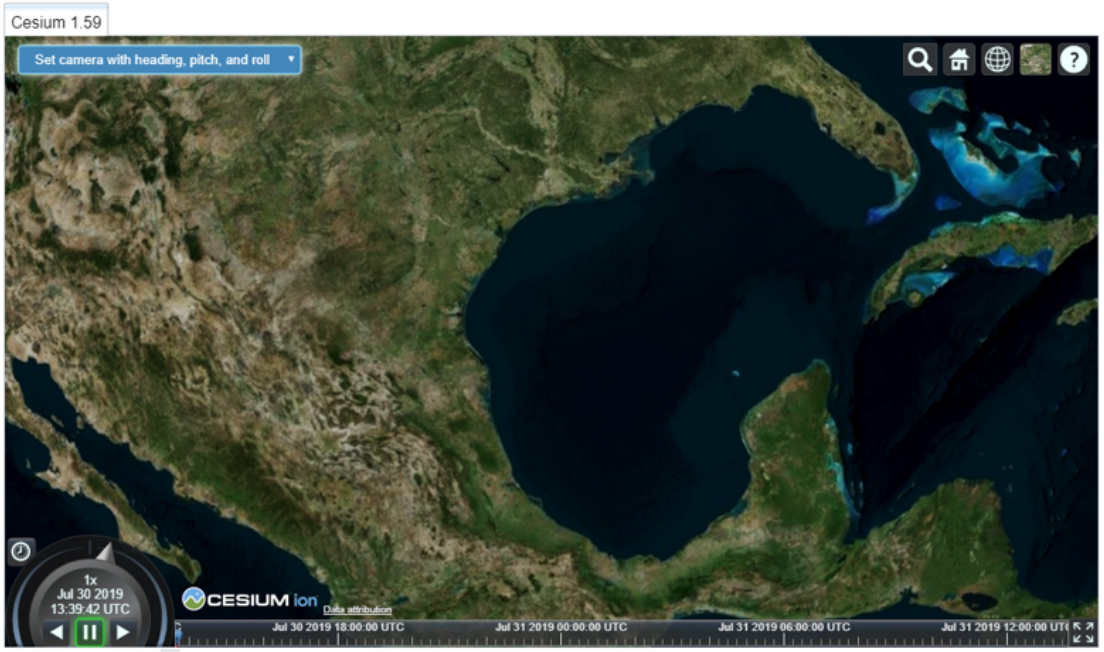

FIGURE 5.4: Cesium web-based simulation platform.

The following the results obtained by the proposed map-based approach using the simulation software and implemented algorithm of the approach in MATLAB environment. *Figure 5.5*, *Figure 5.6* and *Figure 5.7* show the simulation results of map-based attitude determination approach.

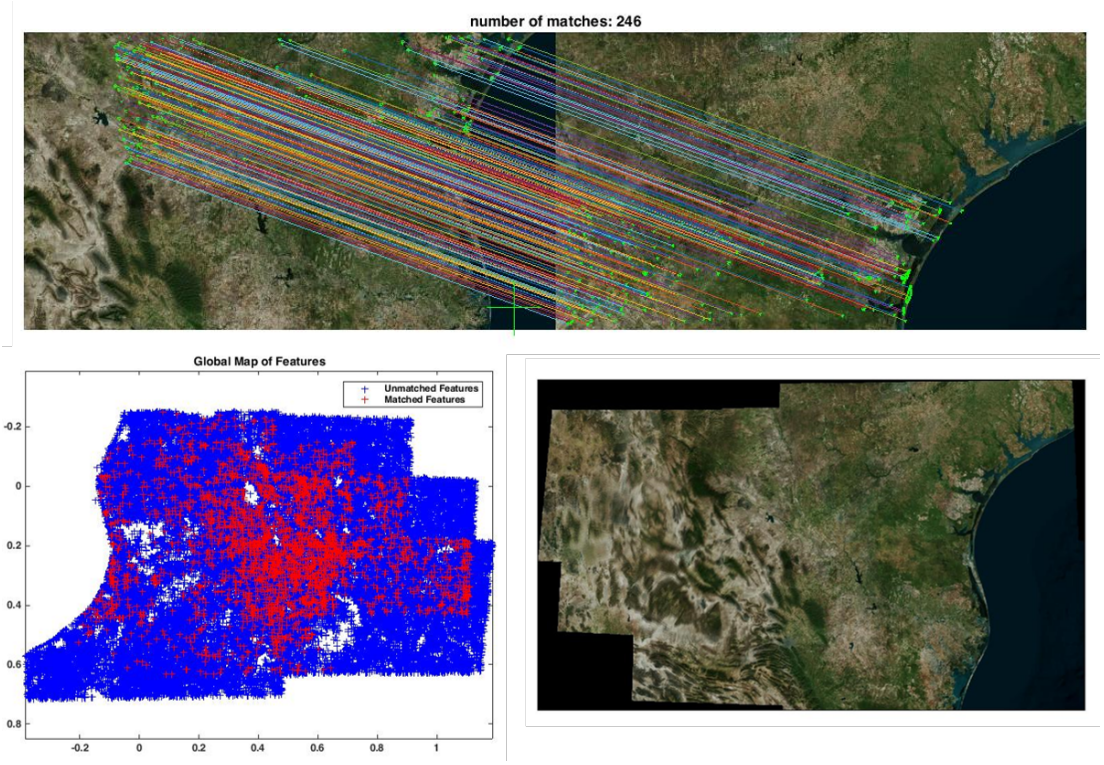

FIGURE 5.5: Stitching and Reconstruction of database images.

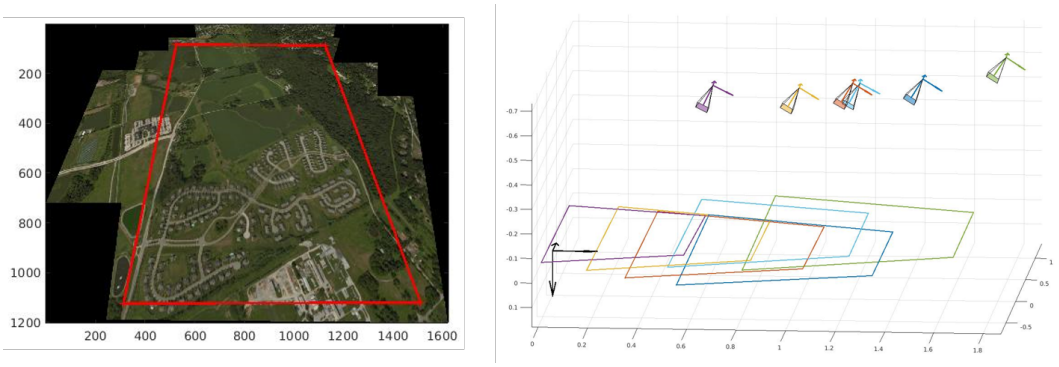

FIGURE 5.6: Simulation results using Sentinel-2 satellite imagery.

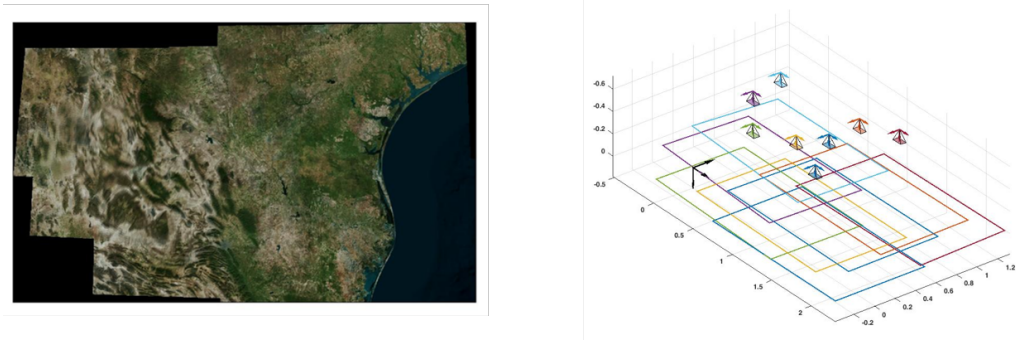

FIGURE 5.7: Simulation results using Sentinel-2 satellite imagery.

Chapter 6

Conclusions

In this dissertation the problem of attitude determination of the satellite is approached using a combination of vision and inertial sensors. The primary aim of this dissertation was to propose an accurate attitude determination and propagation method for small satellites with camera and triad gyros. The conclusions are given in *Section* 6.1.

6.1 Thesis summary

This thesis has sought to design and develop a comprehensive attitude estimation methods for Earth-observation small satellites, using the vision and inertial sensors. Three different approaches have been developed to accurately estimate the satellite attitude based on captured images and a detailed analysis of each approach and their experiments have been performed. Implementations of each of the proposed approaches have been developed as a proof of concept by utilizing the OpenCV and Matlab image-processing libraries. This section summarizes each chapter and outlines the steps taken to achieve the objective of this dissertation.

Chapter 1 provides motivation for this thesis by analyzing trends of small satellite missions over two decades. It was seen that small satellite missions have become increasingly popular due to the relatively inexpensive access to space and standardized deployment system. While these missions have begun with relatively modest objectives, such as educational tools and technology demonstrations, they have recently shifted to real science missions. The more ambitious missions have increased more requirements on the attitude determination and control subsystems. Early small satellite missions could be carried out via a passive attitude control system. Nevertheless, the most recent missions require highly accurate pointing and a 3-axis attitude control subsystem which has increased

the amount of required ADCS hardware on board. It is apparent that a low available volume and limited weight constraints are major challenges that limit the available hardware systems. As a result, it is necessary to develop attitude determination and control methods for these small satellites in this hardware-restricted environment.

Chapter 2 describes the overall background information of ADCS and sensor models. A detailed description of the attitude representations and sensor measurement models relevant to the ADCS are presented. The attitude determination algorithms are also delineated, which includes a description of the various approaches and advanced filtering methods. This chapter also introduces the pinhole camera model and measurement models of the vision-based method necessary for the remaining chapters.

Chapter 3 presents the vision-based algorithms that were developed to efficiently estimate two axes attitude information of small satellite based on Earth-horizon's position in the image. When there are problems in gyros or coarse Sun sensor's measurements, small satellite's attitude information becomes complicated since it cannot directly measure or calculate the attitude of the satellite. A literature review was performed, which showed that while it is possible to estimate two axes attitude information from Earth-horizon images captured by low-cost vision sensors. A set of Earth-horizon image processing algorithms were then developed, which are able to derive roll and pitch angle measurements of the satellite. Laboratory experiments and simulations were then used to show an accuracy and reliability of the proposed approach. The roll and pitch angles are properly estimated, and the average error was 0.67 degrees compared to high-precision one axis rate table.

Chapter 4 solves the problem of estimating complete attitude information, while simultaneously using both measurements of camera and gyro sensors. A literature review showed that many approaches exist for estimating complete attitude information based on the camera sensor but mostly rely on pre-recorded images. While the visual-inertial sensor integration architecture developed in this chapter can be used and overcome some fundamental limitations of vision-only tracking and inertial measurement unit (IMU) only tracking methods using their complementary properties. A Vision-based attitude propagation approach is developed to obtain a nominal attitude (3DOF) estimation based on the planar homography that relates the transformation between two captured image planes. Also, a sensor fusion framework is developed to efficiently fuse both measurements of Vision-based attitude propagation approach and IMU method, and refine overall attitude estimation accuracy by employing unscented Kalman Filter. Laboratory experiments show that this approach can properly estimate and propagate nominal attitude over time with overall RMSE accuracy of 0.067 degrees.

Chapter 5 presents the map-based attitude determination approach that provides absolute attitude in 3 degrees of freedom (3DOF) based on database images and homography of two sequentially captured images of a planar scene. This chapter explored the possibility of improving the robustness of the image-based approaches using the inverted file indexing method. The map-based attitude determination approach is developed to obtain absolute attitude information by decomposing the homography from the captured image to the global map matched image as described in the chapter 4. Finally, the results are obtained by the proposed map-based approach using the "Cesium" simulation platform and implemented algorithm of the approach in the MATLAB environment.

6.2 Discussions and Future work

This section provides a concise, retrospective synopsis of the work presented in this dissertation and emphasizes the notable results. From these results, directions for possible future research are proposed.

Compared to 'vision-based' approach, the combination of the complementary sensors yields a more accurate and robust attitude estimation system. The unscented Kalman Filter is used in proposed sensor fusion framework. The implementation of unscented Kalman filter has been chosen based on its robustness, ability to fuse multiple sensor observations from different reference frames and their good performance with respect to noisy measurements. During the experiments, a high precision one-axis rate table is used to move the experimental multi-sensor setup and experimental results show that this setup is able to estimate the prototype's attitude with an accuracy of 0.07 degrees. The proposed visual-inertial attitude estimation system achieves 3 frames per second (FPS) estimation by fusing vision and inertial sensors using the framework of nonlinear state estimation on the computer with limited computational power equivalent to single board computers. Regarding the experimental results, background research in the camera ego-motion estimation and attitude dynamics show that vision-based approaches (Earth-horizon, Visual-Inertial, Map-based) are can be useful and provide enough attitude information for various small satellite missions.

An overall attitude estimation method for small satellites carrying the vision sensor and triad gyros was presented and tested. The performance of the overall attitude estimation scheme is evaluated by demonstrations for a hypothetical Earth-observation small satellite.

Several avenues for future research related to this dissertation are the following:

- Further investigate possible methods for reducing the computational power of the overall attitude estimation algorithm (for example: use a FPGA boards).
- Further study the performance of the Earth-horizon based approach integrating with additional sensors (such as: triad-Gyro sensors).
- Extend the experiments of the map-based attitude determination approach to determine the absolute attitude and localization of the satellite orbiting the Moon Mars.
- Further study the performance of the map-based attitude determination approach with Vision-based attitude control methods using 3-axis reaction wheels.
- Extend the current research approach into Vision-based navigation system for autonomous planetary landing.
- Validate the performance of the proposed overall attitude determination method using CubeSat class of satellite with applications in the space.

Abbreviations

LEO	**L**ow **E**arth **O**rbit
EHS	**E**arth **H**orizon **S**ensor
CMOS	**C**omplementary **M**etal **O**xide **S**emiconductor
CPU	**C**entral **P**rocessing **U**nit
FOV	**F**ield **O**f **V**iew
DOF	**D**egree **O**f **F**reedom
UAV	**U**nmaned **A**erial **V**ehicle
UKF	**U**nscented **K**alman **F**ilter
EKF	**E**xtended **K**alman **F**ilter
ECEF	**E**arth **C**entered **E**arth **F**ixed
ECI	**E**arth **C**entered **I**nertial
IMU	**I**nertial **M**easurement **U**nit

Bibliography

[1] *H. Heidt, J. Puig-Suari, A. S. Moore, S. Nakasuka, and R. J. Twiggs, CubeSat: A New Generation of Picosatellite for Education and Industry Low-Cost Space Experimen-tation, in Proc. of the 14th Annual AIAA/USU Conference on Small Satellites, Logan,UT, USA, August, 2001.*

[2] *C. Underwood, S. Pellegrino, V. Lappas, C. Bridges, and J. Baker, Using CubeSat micro-satellite technology to demonstrate the Autonomous Assembly of a Reconfigurable SpaceTelescope (AAReST), Acta Astronautica, vol. 114, pp. 112-122, 2015.*

[3] *C. Moore, A. Caspi, T. Woods, P. Chamberlin, B. Dennis, A. Jones, J. Mason, R.Schwartz, and A. Tolbert, The Instruments and Capabilities of the Miniature X-RaySolar Spectrometer (MinXSS) CubeSats, Solar Physics, vol. 293, pp. 21-61, 2018.*

[4] *Nanosats Database, www.nanosats.eu.*

[5] *J.R. Wertz, Spacecraft Attitude Determination and Control. Reidel: Boston, MA, USA, 1978.*

[6] *A. Dagvasumberel and K. Asami, "Vision-based attitude determination system for small satellites using unscented Kalman filter", in Proc. of the 68th International Astronautical Congress, Adelaide, Australia, September, 2017.*

[7] *R. Shimmin, "Using a smartphone camera for nanosatellite attitude determination", Proc. of the Advanced Maui Optical and Space Surveillance Technologies Conference, Hawaii, USA, September, 2017.*

[8] *Dol Bahar, Mohamad, Mohd Effandi, Mohd Hassan, Norhizam Hamzah, Ahmad Arshad, Xandri Farr, Lourens Visagie and Willem Steyn, "Modular CMOS Horizon Sensor for Small Satellite Attitude Determination and Control Subsystem", Proc. of the AIAA/USU Conference on Small Satellites, Utah, USA, August, 2006.*

[9] *David Meller, Prapat Sripruetkiat and Kristin Makovec, "Digital CMOS Cameras for Attitude Determination", Proc. of the AIAA/USU Conference on Small Satellites, Utah, USA, August, 2000.*

[10] *Jansen Van Rensburg, "An Infrared Earth Horizon Sensor for a LEO Satellite", Thesis, Matieland, South Africa, March, 2008.*

[11] *Alessandro Bevilacqua, Alessandro Gherardi, and Ludovico Carozza, "A vision-based approach for high accuracy assessment of satellite attitude", 2009 IEEE 12th ICCV International Conference, Kyoto, Japan, October, 2009.*

[12] *L. Carozza and A. Bevilacqua, "Error analysis of satellite attitude determination using a vision-based approach", ISPRS Journal of Photogrammetry and Remote Sensing, vol. 83, pp. 19-29, 2013.*

[13] *G. Klančar, S. Blažič, D. Matko, and G. Mušič, "Image-Based Attitude Control of a Remote Sensing Satellite", Journal of Intell Robot Syst., vol. 66, pp. 343-357, 2012.*

[14] *A. Rawashdeh, W. Danhauer, and E. Lumpp, "Design of a stellar gyroscope for visual attitude propagation for small satellites", in Proc. of IEEE Aerospace Conference, Big Sky, MT, USA, March, 2012.*

[15] *T. Kouyama, A. Kanemura, S. Kato, N. Imamoglu, T. Fukuhara, and R. Nakamura, "Satellite Attitude Determination and Map Projection Based on Robust Image Matching", Remote Sensing, vol. 9, no. 1, pp. 1-20, 2017.*

[16] *P. Corke, J. Lobo, and J. Dias, "An Introduction to Inertial and Visual Sensing", The International Journal of Robotics Research, vol. 26, pp. 519-535, 2007.*

[17] *Hwangbo and T. Kanade, "Visual-inertial UAV attitude estimation using urban scene regularities", in Proc. of 2011 IEEE International Conference on Robotics and Automation, Shanghai, China, pp. 2451-2458, May, 2011.*

[18] *H. G. de Marina, F. Pereda, J.M.G. Sierra, and F. Espinosa, "UAV attitude estimation using unscented kalman filter and TRIAD", IEEE Trans. Ind. Electron., vol. 59, pp. 4465–4474, 2012.*

[19] *N. D. Tan, T.Q. Vinh, and B. T. Tuyen, "A New Approach for Small Satellite Gyroscope and Star Tracker Fusion", Indian Journal of Science and Technology, vol. 9, no. 17, pp. 1-7, 2016.*

[20] *R. V. Garcia, H. K. Kuga, and M. C. Zanardi, "Unscented Kalman filter applied to the spacecraft attitude estimation with euler angles", Mathematical Problems in Engineering, vol. 2012, pp. 1-12, 2012.*

[21] *E. J. Lefferts, F. L. Markley and M. D. Shuster, "Kalman ltering for spacecraft attitude estimation", J. Guid. Control Dyn., vol. 5, no. 5, pp. 417-429, 1982.*

[22] *R. Hartley and A. Zisserman, Multiple view geometry in computer vision. Cambridge university press: New York, USA, 2003.*

[23] *M. Wei, J. Bao, F. Xing, Z. Liu, T. Sun, and Z. You, "System-on-a-Chip Based Nano Star Tracker and Its Real-Time Image Processing Approach", in Proc. of the 30th Annual AIAA/USU Conference of Small Satellite, Logan, UT, USA, August, 2016.*

[24] *N. Trawny and S. Roumeliotis, "Indirect Kalman lter for 3d attitude estimation", Technical report., University of Minnesota, Department of Computing Science and Engineering, 2005.*

[25] *S. J. Julier and J. K. Uhlmann, "A New Extension of the Kalman Filter to Nonlinear Systems", in Proc. of the International Symposium Aerospace/Defense Sensing, Simulation and Controls, Orlando, FL, USA, pp. 182–193, April, 1997.*

[26] *J. L. Crassidis and F. L. Markley, "Unscented filtering for spacecraft attitude estimation", J. Guid. Control Dyn., vol.26, pp. 536–542, 2003.*

[27] *Kasper Vinther, Kasper F. Jensen, Jesper A. Larsen, and Rafael Wisniewski, "Inexpensive CubeSat Attitude Estimation Using Quaternions and Unscented Kalman Filtering", Automatic Control in Aerospace, 4(1), 2011.*

[28] *J. Li, M. A. Post and R. Lee, "A novel adaptive unscented Kalman filter attitude estimation and control systems for 3U nanosatellite", in Proc. of European Control Conference, Zurich, Switzerland, pp. 2128-2133, July, 2013.*

[29] *Vlad Grigore, "Unscented Kalman Filters for Attitude and Orbit Estimation of a Low Earth Orbit CubeSat", Thesis, Stockholm, Sweden, January, 2015.*

[30] *Opencv Library, www.opencv.org.*

[31] *John Polansky, HORYU-IV Project Team, and Mengu Cho, "Arc Event Generator and Investigation Satellite HORYU-IV", 28th Annual AIAA/USU Conference of Small Satellite, Logan, UT, USA, August, 2014.*

[32] *C. Dou, X. Zhang, H. Gou, C. Han, and M. Liu, "Improving the geolocation algorithm for sensors on-board the ISS: Effect of drift angle", Remote Sensing, vol. 6, pp. 4647-4659, 2014.*

[33] *E. Malis and M. Vargas, "Deeper understanding of the homography decomposition for vision-based control", PhD dissertation, INRIA, 2007.*

[34] *E. Rosten, R. Porter, and T. Drummond, "Faster and Better: A Machine Learning Approach to Corner Detection", IEEE Transactions on Pattern Analysis and Machine Intelligence, vol. 32, pp. 105-119, 2010.*

[35] *D. Lowe, "Distinctive image features from scale-invariant keypoints", Int. J. Comput. Vis., vol. 60, pp. 91–110, 2004.*

[36] *H. Bay, A. Ess, T. Tuytelaars, and L. V. Gool, "Speeded-up robust features (SURF)", Comput. Vis. Image Underst., vol. 110, pp. 346–359, 2008.*

[37] *C. Tomasi and T. Kanade, "Shape and Motion from Image Streams: A Factorization Method—Part 3: Detection and Tracking of Point Features", Technical Report CMU-CS-91-132, Carnegie Mellon University: Pittsburgh, PA, USA, 1991.*

[38] *Y. Abdel-Aziz and H. Karara, "Direct linear transformation from comparator coordinates into object space coordinates in close-range photogrammetry", in Proc. of Symposium on Close-Range Photogrammetry, Urbana, IL, USA, pp. 1-18, January, 1971.*

[39] *M. A. Fisher and R. C. Bolles, "Random sample consensus: A paradigm for model tting with applications to image analysis and automated cartography", Commun. ACM, vol. 24, pp. 381–395, 1981.*

[40] *www.computer-vision-talks.com/post/2011-07-13-comparison-of-the-opencv-feature-detection-algorithms/.*

[41] *Jean-Yves Bouguet, Camera Calibration from Points and Lines in Dual-Space Geometry.*

[42] *E. Wan and R. van der Merwe, The Unscented Kalman Filter. In Kalman Filtering and Neural Networks. Wiley: Weinheim, Germany, 2001.*

[43] *P. Muri, S. Runco, C. Fontanot, and C. Getteau, "The High Definition Earth Viewing (HDEV) payload", in Proc. of IEEE Aerospace Conference, Big Sky, MT, USA, pp. 1–7, March, 2017.*

[44] *A. Angeli, D. Filliat, S. Doncieux, and A. Meyer, "Fast and incremental method for loop-closure detection using bags of visual words", IEEE Trans. Robot., 24(5) (2008).*

[45] *T. Botterill, S. Mills, and R. Green, "Bag-of-words-driven single camera simultaneous localisation and mapping", Journal of Field Robotics, 2010.*

[46] *D. Galvez-Lopez, and J.D. Tardos, "Bags of binary words for fast place recognition in image sequences", IEEE Trans. Robot., 28(5), 2012.*

[47] *D. Nistér and H. Stewenius, "Scalable recognition with a vocabulary tree", In Proceedings of the 2006 IEEE Computer Society Conference on Computer Vision and Pattern Recognition, 2, pp 2161-2168, 2006.*

[48] *Y. Liu, and H. Zhang, "Indexing visual features: Real-time loop closure detection using a tree structure", 2012 IEEE International Conference on Robotics and Automation (ICRA), 2012.*

[49] *Y. Ma, S. Soatto, J. Kosecka, and S. S. Sastry, "An Invitation to 3-D Vision: From Images to Geometric Models", SpringerVerlag, ISBN 0387008934, 2003.*

[50] *CesiumJS - Geospatial 3D Mapping and Virtual Globe Platform", https://cesiumjs.org/.*

Publication List

- Vision-Based Attitude Determination System for Small Satellites Using Unscented Kalman Filter, Proc. 68th International Astronautical Congress, Amartuvshin Dagvasumberel, Kenichi Asami
- Visual-Inertial Attitude Propagation System for Small Satellites Using Unscented Kalman Filter, Proc. International Workshop on Lean Satellite, Amartuvshin Dagvasumberel, Kenichi Asami
- Visual-Inertial Attitude Propagation for Small Satellites Using Unscented Kalman Filter, Proc. 4th IAA Conference on Dynamics and Control of Space Systems, Amartuvshin Dagvasumberel, Kenichi Asami
- Design SVM Classifier for Automatic Modulation Recognition Systems, UNISEC Space Takumi Journal, Mohamed Elhady Keshk, Dagvasumberel Amartuvshin, Rafael Rodriguez, Kenichi Asami
- A Visual-Inertial Attitude Propagation for Resource-constrained Small Satellites, Journal of Aeronautics and Space Technologies, Amartuvshin Dagvasumberel, Kenichi Asami
- Attitude Determination System for Small Satellites Using Low-cost Vision Sensor, Proc. International Scientific and Practical Conference, Amartuvshin Dagvasumberel, Kenichi Asami

About Author

Amartuvshin Dagvasumberel was born in Darkhan-Uul city, Mongolia on June 5, 1991. He received his B.Sc. degree in Physics Electronics from School of Physics and Electronics, National University of Mongolia in 2013. And the M.Sc. degree in Environmental Remote Sensing and Geographic Information system, from National University of Mongolia in 2015. He has been a Ph.D. student in Department of Applied Science for Integrated System Engineering, Graduate School of Engineering, Kyushu Institute of Technology in Japan. His research interests are attitude determination and control systems for small satellites, computer vision, nonlinear filtering, and satellite proximity operations. In 2017, he worked as a camera system engineer on the "Birds project" (A trans-boundary interdisciplinary satellite project).